2015

Simulating the Impacts and Sensitivity of the Southeastern United States Climatology to Irrigation

Christopher Manuel Selman

FLORIDA STATE UNIVERSITY

COLLEGE OF ARTS AND SCIENCES

SIMULATING THE IMPACTS AND SENSITIVITY OF THE SOUTHEASTERN UNITED STATES CLIMATOLOGY TO IRRIGATION

By

CHRISTOPHER MANUEL SELMAN

A Dissertation submitted to the
Department of Earth, Ocean and Atmospheric Sciences
in partial fulfillment of the
requirements for the degree of
Doctor of Philosophy

2015

Christopher Selman defended this dissertation on July 9, 2015.
The members of the supervisory committee were:

Vasubandhu Misra
Professor Directing Dissertation

Sachin Shanbhag
University Representative

Mark A. Bourassa
Committee Member

Guosheng Liu
Committee Member

Zhaohua Wu
Committee Member

The Graduate School has verified and approved the above-named committee members, and certifies that the dissertation has been approved in accordance with university requirements.

ACKNOWLEDGMENTS

I would like to acknowledge the numerous friends, family members and loved ones who helped me through difficult times. In particular, I would like to thank my major professor, Dr. Vasubandhu Misra for his continued support and guidance through the preparation of this manuscript. Through his suggestions, and those of my esteemed committee, this manuscript was created with minimal difficulty.

TABLE OF CONTENTS

LIST OF TABLES

LIST OF FIGURES

ABSTRACT

The diurnal variations from a high-resolution regional climate model (Regional Spectral Model; RSM) are analyzed from 6 independent decade long integrations using lateral boundary forcing data separately from the National Centers for Environmental Prediction Reanalysis 2 (NCEPR2), and European Center for Medium-Range Weather Forecasts (ECMWF) 40-year Reanalysis (ERA40) and the 20th Century Reanalysis (20CR). With each of these lateral boundary forcing data, the RSM is integrated separately using two convection schemes: the Relaxed Arakawa-Schubert (RAS) and Kain-Fritsch (KF) schemes. The results show that RSM integrations forced with 20CR have the least fidelity in depicting the seasonal cycle and diurnal variability of precipitation and surface temperature over the Southeastern United States (SEUS). The remaining four model simulations show comparable skills. The differences in the diurnal amplitude of rainfall during the summer months of the 20CR forced integration from the corresponding NCEPR2 forced integration, for example, is found to be largely from the transient component of the moisture flux convergence. The root mean square error (RMSE) of the seasonal cycle of precipitation and surface temperature of the other four simulations (not forced by 20CR) were comparable to each other and highest in the summer months. But the RMSE of the diurnal amplitude of precipitation and the timing of its diurnal zenith were largest during winter months and least during summer and fall months in the four model simulations (not forced by 20CR). The diurnal amplitude of surface temperature in comparison showed far less fidelity in all models. The phase of the diurnal maximum of surface temperature however showed significantly better validation with corresponding observations in all of the 6 model simulations

The impacts of irrigation on SEUS diurnal climate are then investigated. An extreme case is assumed, wherein irrigation is set to 100% of field capacity over the growing season of May through October (IRR100). Irrigation is applied to the root zone layers of 10-40cm and 40-100cm soil layers only. It is found that in this regime there is a pronounced decrease in monthly averaged temperatures in irrigated regions across all months. In non-irrigated areas a slight warming is simulated. Diurnal maximum temperatures in irrigated areas warm, while diurnal minimum temperatures cool. The daytime warming is attributed to an increase in shortwave flux at the surface owing to diminished low cloud cover. Nighttime cooling results as a consequence

of higher net downward ground heat flux. Both diurnal and monthly average precipitations are reduced over irrigated areas at a magnitude and spatial pattern similar to one another. Due to the excess moisture availability, evaporation is seen to increase, but this is balanced by a corresponding reduction in sensible heat flux. Concomitant with additional moisture availability is an increase in both transient and stationary moisture flux convergences. However, despite the increase, there is a large-scale stabilization of the atmosphere stemming from a cold surface and a warmed vertical column.

Three additional regional climate model runs centered on the SEUS assume a crop growing season of May through October and are irrigated at 25%, 50%, 75% (IRR25, IRR50, IRR75, respectively) of the root zone field capacity to assess the sensitivity of the SEUS climate to irrigation. A fifth run, assuming no irrigation (CTL), is used as the basis for comparison. Across all IRR runs, it is found that there is a general reduction in monthly mean precipitation over the irrigated cells relative to CTL, with much of the change occurring in the sub-diurnal scales. This manifests as an increase dry days and reduction in > 1 mm/day rainfall events. IRR25 is seen to have the lowest change in both, while IRR100 is seen to have the greatest change. Area-averaged precipitation over the irrigated cells reveals a strong reduction in precipitation in IRR100 (on the order of 0.4 mm/hr) with a much weaker reduction in IRR25. Vertically integrated moisture convergence is seen to have the most pronounced sensitivity pattern across all runs. Monthly averaged temperatures are reduced over irrigated areas, with the intensity of the reduction increasing as irrigation vigor increases. This is attributed to a systematic change in ground heat flux that transports heat into the subsurface soil layers in the irrigated cells. The precipitation ahead of the transient cold fronts is reduced by irrigation as it passes over the irrigated cells. The intensity of the net precipitation reduction becomes more intense as irrigation vigor increases. Lastly, heat waves in the SEUS are reduced in intensity just over the irrigated cells, though likely increasing in frequency due to lowered temperature thresholds for heat wave definition.

CHAPTER 1

INTRODUCTION

1.1 Diurnal Climatology of the Southeast

In the Southeastern United States (SEUS), diurnal variation of precipitation accounts for nearly 40% of the total seasonal variation in the summer (Bastola & Misra 2013). In fact, the diurnal variation of rainfall is a considerably strong and persistent feature of SEUS climatology (Dai et al. 1999). Carbone and Tuttle (2008) claim that the diurnal variability is stronger over the SEUS than in any other region of the contiguous United States. By virtue of these facts, especially when the climatological features of diurnal variations of precipitation are relatively stationary (Dai et al. 1999), it comes as no surprise that the SEUS is climatologically the wettest region of the United States (Chan and Misra 2010).

There is growing evidence that anthropogenic climate change presents itself in diurnal signals of surface temperature, such as the observed warming in daily minimum temperatures (Zhou et al. 2008; Portmann et al. 2008; Lauritsen and Rogers 2012). Dai (1999) noted a reduction in the afternoon precipitation frequency by 5-10% per decade, and a rainfall amount reduction of about 2 to 4 mm/decade over the SEUS. Similarly, that larger-scale climatological phenomenon affected by climate change, such as the North Atlantic Subtropical High, can impart an influence on the diurnal variability of sea breeze circulations (Li et al. 2011, Misra et al. 2011; Selman et al. 2013). It is the purpose of this paper to assess the fidelity of diurnal variations in temperature and precipitation as produced by multiple simulations of a regional climate model forced by a variety of global reanalysis at the lateral boundaries and two different cumulus parameterization schemes given such relevance of diurnal variations to the current and future climate of the SEUS.

Diurnal precipitation in the SEUS is driven by a combination of processes with strong sub-regional dependence. For instance, in coastal regions of the SEUS, sea breezes are drivers of diurnal variability (Schwartz and Bozart 1979; Biggs and Graves 1962; LeMone 1973). The late afternoon convergence of sea breezes from the eastern and western coastlines of peninsular Florida results in frequent convective systems (Byers and Rodebush 1948; Gibson and Haar 1990). In non-peninsular areas, it is the convergence of sea breeze circulation and background

winds that produce the convective systems (Gentry and Moore 1954). The resultant convective systems do not form immediately at the coastline, and convergence is strongest where coastal curvature accentuates sea breeze convergence (Pielke 1974). In the non-coastal regions of the SEUS, orographic effects represent a sizeable portion of the diurnal variability (Parker and Ahijevych 2007). Mountain-crossing mesoscale complex systems from the Central United States, in combination with the ample moist air in the region develop and sustain these convective episodes (Parker and Ahijevych 2007). Additional large-scale drivers of diurnal precipitation include the North Atlantic Subtropical High (Li et al. 2011) which depending on its zonal position (eastward or westward) can suppress daily maximum convection by increasing local subsidence. Li et al. (2013) identified a primary driver of warm season precipitation variability to be large-scale moisture transport, primarily impacted by adjustments to the dynamic environment of the Southeast.

The diurnal variation of precipitation is coincident with corresponding variations in ground hydrology. For example, non-runoff precipitation enhances local soil moisture, which may lead to enhancing local soil-moisture/precipitation coupling (Wei and Dirmeyer, 2012). The phase difference between the diurnal variations of precipitation and temperature can impact the partitioning of surface energy of latent and sensible heat fluxes (Dai and Trenberth 2004). In the SEUS, Misra and Dirmeyer (2009) found that evaporation is energy limited both in the winter and summer seasons. Furthermore, evapotranspiration (ET) is a major contributor to the water budget in the SEUS (Sun et al. 2002). In the SEUS ET also has a diurnal cycle peaking roughly at 1600 UTC (Liu et al. 2005). This peak in ET is offset from the corresponding observed peak in precipitation (2200 UTC; Liu et al. 2005; Stefanova et al. 2012).

1.2 Simulating Diurnal Climatology of the Southeast

The errors in the prescribed lateral boundary conditions limit the fidelity of a regional climate model simulation (Risbey and Stone 1996; Misra et al. 2003; Misra 2007). Therefore it is important to account for the uncertainty and relative fidelity of the regional model simulation of an important feature as the diurnal variation over the SEUS. Furthermore, cumulus parameterization scheme has been identified as one of the key processes that strongly affect the

simulation of the diurnal variations in rainfall (Liang et al. 2004; Lee et al. 2007; Wang et al. 2007; Evans and Westra 2012; Harding et al. 2013; Dirmeyer et al. 2012).

Dirmeyer et al. (2012) noted that while implementation of better cumulus parameterizations can improve simulations of diurnal variations, the improvements exhibit strong regionality. In a related study, Stefanova et al (2012) using the National Centers for Environmental Prediction - Department of Energy Reanalysis 2 (NCEPR2; Kanamitsu et al. 2002) and the ECMWF 40-year Reanalysis (ERA40; Uppala et al. 2005) as lateral boundary conditions to an RCM suggested sensitivity to simulation of the diurnal phase and amplitude of precipitation over the SEUS. Similarly, DiNapoli and Misra (2012) showed that dynamic downscaling of the 20th century global reanalysis (20CR; Compo et al. 2011) yielded realistic simulations of the inland progression of the sea breeze in panhandle Florida. However, all of these studies lack a systematic analysis of the diurnal variations forced by the various global atmospheric reanalysis and the combined sensitivity to cumulus parameterization schemes.

In this paper, we examine the diurnal variations from 10-year integrations of regional climate model run independently with two different cumulus parameterization schemes and forced with three different global atmospheric reanalysis. In total, in this study we have examined results from 6 different experiments of the regional climate model. The motivation to conduct these experiments is to systematically analyze the sensitivity of the simulated diurnal variations to the choice of the cumulus parameterization schemes and lateral boundary forcing. As pointed out in Stefanova et al. (2012), the downscaled seasonal mean precipitation from NCEPR2 and ERA40 showed systematic differences, which were contrary to the corresponding rainfall differences in the two global reanalysis. We have therefore conducted this comprehensive study to understand the influence of the large-scale lateral boundary conditions and convection schemes on the dominant diurnal variations in the southeastern US.

The simulation of diurnal variations of both temperature and precipitation is however one of the outstanding shortcomings of the Atmospheric General Circulation Models (AGCMs; Dai et al. 1999; Dai and Trenberth 2004; Slingo et al. 2004; Braganza et al. 2004; Lewis and Karoly 2013). For example, Lewis and Karoly (2013) indicate that the linear trend of diurnal temperature range in the 1951-2005 period is underestimated in the CMIP5 models (which is similar to that exhibited by CMIP3) because they overestimate the changes in the maximum temperature. They further attribute these errors to deficiencies in cloud cover and land surface processes. Dai (2006)

indicated that AGCM from the CMIP3 project produce very strong diurnal signals over land, attributed to an early wet season onset, and frequent but weak rainfall. There is however a suggestion from many studies that finer resolution models with astute choice of cumulus parameterization scheme can lead to improvement in the diurnal variations of precipitation (Liang et al. 2004; Lee et al. 2007; Wang et al. 2007; Evans and Westra 2012; Harding et al. 2013). Some studies indicate that the erroneous phase shift of the diurnal cycle of precipitation displayed by the AGCMs can be rectified to some extent by the high resolution offered by regional climate models (Liang et al. 2004; Chow and Chan 2009). For example, Dirmeyer et al. (2012) noted that improved diurnal rainfall simulations follow from improved simulation of the mean rainfall rate when resolution is increased.

1.3 Impacts of Irrigation on Climatology

Irrigation has been identified as a significant contributor to regional climatology. For instance, irrigation's impact on precipitation manifests in several ways. Conversion from most non-tropical vegetation types to cropland generally produces increases in precipitation by modifying boundary layer structure and available moisture (Pielke et al. 2007). Transitional regions, between moist and dry areas, have strong soil moisture-precipitation coupling, which can lead to increased rainfall over these regions (Wei and Dirmeyer 2012). Over the Indian subcontinent, irrigation weakens the monsoon heat low, allowing for deeper inland penetration of monsoon circulation and evapotranspiration to produce local precipitation (Saeed et al. 2009). In areas of heavy irrigation, local precipitation is seen to increase, though the precipitation gain is generally less than the loss of water through ET, indicating that irrigation can have a net negative effect on local water budgets (Wei et al. 2013). This increase in ET has a second order effect on atmospheric circulation, strengthening tropical rain belts and modifying the Indian monsoon (Puma and Cook 2010). However, these secondary effects appear to be somewhat model dependent. Similarly, development of strong soil moisture gradients can produce thermally induced, sea breeze-like circulations on land (Ookouchi et al. 1984).

Likewise, land-use change has an observable impact on diurnal variations in temperature (Defries et al. 2002, Oke 1982) and other thermodynamic/hydrologic variables including humidity and evapotranspiration (Sorooshian et al. 2011). Thus, when conducting climatological simulations it is of the utmost importance that land-use is considered, especially in regions like

the Southeastern United States (SEUS) where diurnal variations are significant (Bastola and Misra, 2013). In a related study, Misra et al. (2012) showed that irrigation has an impact on the observed surface temperature trends in the SEUS. In recent years, development of next-generation global and regional climate models has allowed for some capturing of these features with the development of urban extent databases (e.g., Schneider et al. 2009) and regional irrigation maps (e.g., Siebert et al. 2005). However, global climate models continue to use resolutions that are not suited for resolving small-scale, dynamic phenomena (Selman et al. 2013). Hence there remains a need for high-resolution regional climate models. Such models have well-documented skill in resolving both features arising from land-use change and small-scale dynamic phenomena (Kanamaru and Kanamitsu 2008, Misra et al. 2012, Dinapoli and Misra 2012).

The effects of irrigation on diurnal variations of all atmospheric and sub-surface variables are well documented in regions outside of the SEUS. The most noted change is a reduction of globally averaged daytime maximum temperatures (on the order of 0.5-1K) owing to increased cloud cover (Sacks et al. 2009). It has been noted that this cooling of temperature can potentially mask warming associated with climate change (Lobell et al. 2008). In the Great Plains, application of irrigation in a regional climate model (RCM) caused a cooling in maximum temperatures owing to an increase in latent heat (LHF) and decrease in sensible heat (SHF) (Qian et al. 2013). In addition to this cooling, there exists also a slight warming of nighttime minimum temperatures arising from increased thermal conductivity of the darker, wetter soil (Kanamaru and Kanamitsu 2008). These and other results exhibit some regional and model configuration dependencies (Sorooshian et al. 2012; Lobell et al 2009). Cooling is generally felt less in regions that are climatologically wet or have an already high soil moisture level (Lobell et al. 2008; Lobell et al. 2009). Irrigation implementations that fix the soil moisture values at a specific percentage tend to overestimate evapotranspiration when compared with implementations that add water only when falling below a certain water depletion threshold (Sorooshian et al. 2012).

Changes to the surface energy budget are not observed at just the surface, however. Increases in LH at the surface from irrigation mirrored increases in the mixing ratio of water vapor in the lower atmosphere (Kueppers and Snyder 2012). By extension it is then plausible to assume that addition of irrigation can affect the vertical structure of the atmosphere and boundary layer. Kueppers and Snyder (2012) noted a lowering of the PBL height, which

manifested more prominently in a dry year over an irrigated area. Likewise, in the California Central Valley, humidity over irrigated areas was seen to increase by 9-20% and PBL heights were found to be low as well (Sorooshian et al. 2011). In both studies it was noted that the effects of irrigation did not extend far beyond the irrigated cells.

Ground hydrology is in large part dictated by soil and vegetative surface type. One of the most readily apparent ways human action can influence ground hydrology is via the application of irrigation (Pielke et al. 2007). Irrigation is modest in the SEUS; Florida withdrew on average 1,000 to 5,000 million gallons of water per day in 2005 (Hutson et al. 2000). This is in contrast to California, which withdrew 15,000 to 25,000, million gallons per day in 2005 (Hutson et al. 2000). This large difference is explained largely by the differing climates of each state. The California Central Valley, a semi-arid/steppe climate, is the most productive agricultural region in the country (McNally et al. 2004), with a gross value of $16 billion for the year 2004 owing to its irrigation withdrawals and year-round mild climate that extends the growing season substantially. The SEUS, a more humid subtropical climate with a similarly long growing season, has profits of $11 billion between Georgia, Florida, Alabama, Mississippi and South Carolina (USDA ERS). However, unlike California, agriculture in the SEUS is largely rain fed. As the agriculture industry of the SEUS grows so too will the demand for water. Thus, the future of agriculture in the SEUS rests on intelligent water management policies similar to those of California, including the adoption of broader irrigation practices.

CHAPTER 2

METHODS

2.1 The Regional Spectral Model

The Regional Spectral Model (RSM; Kanamitsu et al. 2010) was adopted as the regional climate model for this study. The spatial resolution of the RSM adopted for this study is 10 km grid resolution, with output from the integration stored at hourly intervals. The RSM has demonstrated proficiency at resolving diurnal variations in the SEUS (Misra et al. 2011; Stefanova et al. 2012; DiNapoli and Misra 2012; Selman et al. 2013). The RSM has a unique feature of scale selective bias correction (Kanamaru and Kanamitsu 2007) that allows us to avoid multiple nesting in going from the relatively very coarse resolution of the global reanalysis (typically 2° resolution) to the target 10 km grid resolution. It is essentially a spectral nudging technique conducted in the wave-number domain to restrict the RSM drift from the large-scale forcing at the largest spatial scales of the regional domain. The RSM uses the NOAH land-surface model (Ek et al. 2003). The vegetation map is based on the USGS vegetation map reduced to the 12 NOAH types (Loveland et al. 1995), which offers a realistic depiction of land-use over the SEUS.

2.2 Cumulus Parameterization and Lateral Boundary Condition

Of particular importance to this study was the choice of the cumulus parameterization scheme used in the model simulations. Changing convective schemes within a model can produce dramatically different model biases in rainfall (Meinke et al. 2007). The choice of the convection scheme also has an influence on the magnitude of diurnal variations (Liang et al 2004). In a study employing the RSM, Meinke et al. (2007) found that use of the Kain-Fritsch convection scheme (KF; Kain and Fritsch, 1993) produced a realistic simulation of diurnal precipitation over the SEUS. Numerous studies employing the RSM have also noted realistic simulations of diurnal precipitation using the Relaxed-Arakawa Schubert scheme (RAS; Moorthi and Suarez 1992; Stefanova et al. 2012, DiNapoli and Misra 2012). The KF implementation within the RSM includes detrainment, entrainment and imposes a minimum

entrainment rate over dry and weakly unstable environments. Based on cloud base temperature, non-convective precipitation may occur for any cloud that does not reach the minimum cloud depth for convective precipitation. Mass flux is specified as a fraction of udraft mass flux at cloud base (MyMeteo, 2015). RAS, on the other hand, assumes that mass flux is a linear function of height, and relaxes cloud ensemble toward equilibrium, rather than invoking a quasi-equilibrium of the cloud ensemble (Das et al. 2002). In order that we may fully understand how this important choice of parameterization impacts results from our model, we choose to compare data from these two convective schemes known for producing realistic simulations of diurnal precipitation. While additional convection schemes are available within the RSM, these two have been employed in prior studies and have been well tested for climate simulations.

Six model integrations were performed over the SEUS over the period spanning January 1st 1989 to December 31st 1999 (Table 1). In order to mitigate errors introduced by model spin-up, the entirety of 1989 is removed from our calculations. The RSM was forced with three different global atmospheric reanalysis packages: the NCEPR2, the ERA40 and the 20CR, which were downscaled to a horizontal resolution of 10 km using the two convective schemes (mentioned above) separately. A brief outline of the three global reanalysis is given in Table 2. Each global reanalysis package features a different choice of assimilated sea surface temperature data over the integration period. There are some similarities between the packages however, for instance both NCEPR2 and 20CR are run using the same horizontal spectral truncation and vertical discretization. Despite this similarity, there is a fundamental difference between the two packages through 20CR's assimilation of surface observations of mean sea level pressure only. Thus diminishing any overlap that may exist between the other reanalysis packages and 20CR. Soil moisture is initialized by interpolating data from the corresponding analysis to the RSM grid.

Fig. 1 depicts the domain and vegetation map of our integrations. Further, it also contains 5 sub-regions that we believe to be representative of different climatological drivers of diurnal variability. Sub-region 1, the Florida Peninsula, has diurnal variability driven primarily by sea-breeze convergence (Wallace 1975). Sub-region 2 is primarily driven by Southerly sea breezes (Wallace 1975), while sub-region 3's variability is primarily driven by the interaction of the sea breeze and the sea-breeze-like circulations arising from thermal differences in soil properties (Wootten et al. 2010). Sub-region 4 is in a unique position, as neither sea breeze nor orographic

effects directly drive its diurnal variability, given its situation of being far away from inland propagation of sea breezes and distance from the Appalachians. Finally, the fifth sub-region has diurnal variability driven primarily by a combination of orographic effects in the eastern portion, and propagating weather systems of the higher latitudes from the central United States (Parker and Ahijevych, 2007). We also consider a sixth region which represents the entire model domain shown in Fig. 1. These sub-regions will be used to assess model sensitivity to lateral boundary conditions. In order to prevent significant bias being introduced into our analysis, the boundary grid cells in which the RSM nudges the solution towards the global reanalysis following Lehmann (1993) are removed.

2.3 The Modified Noah Land Surface Model

Crucial to our study is the modification of the Noah LSM to account for irrigation. The irrigation technique we have chosen to apply to our model is that of a sub-irrigation technique, wherein additional moisture is applied directly to the root zone of the cropland. We choose to use a sub-irrigation technique, as the growing regions of the SEUS have a shallow water table, with table depths in Florida as shallow as 10cm (Sun et al. 2000). An important feature of sub-irrigation systems is the ability to drain excess water, which we are essentially doing when we constrain the adjusted soil moisture to be not below the wilting point but not above field capacity. Each vegetation type has a specified number of root zones within its parameterization. For the cultivation vegetation type, to which the irrigation is applied, the model has prescribed three root zones, which occupy the span of 0-10cm, 10-40cm and 40-100cm. Because we employ a sub-irrigation type scheme, we do not moisten the top layer, and instead apply irrigation to the 10-100cm (root zone) layers. The sub-irrigation process used in this study is summarized in Fig. 2.

The adjusted LSM allows the user to specify what fraction of field capacity they would like all irrigated cells to be set at and how long the growing season should be. For the purposes of this study, 100%, 75%, 50% and 25% (IRR100, IRR75, IRR50 and IRR25 respectively) of field capacity from the period spanning May to October are chosen. This method carries the weakness that all cells considered to be croplands are fixed to the same percentage of field capacity for the specified months. The real world implication of this is that all municipalities are

growing the exact same crop over the same period. Since soil moisture adjustments are being done every time step. This results in anywhere from 10-11 times more water being added to the system than in the real world. This method of irrigation is however similar to some of the previous such studies, which did not keep an account of the water added (Lobell et al. 2006; Kanamaru and Kanamitsu 2008). To understand the implication of this issue on water usage further, we have added a new tracking variable to the model that reports how much water is being added to or taken out of a cell at each time step.

2.4 Ensemble Empirical Mode Decomposition

In order to isolate the diurnal signal, Ensemble Empirical Mode Decomposition (EEMD; Huang and Wu 2008; Wu et al. 2011) was performed on each of the 10-year model integrations for both precipitation and temperature. EEMD is a data adaptive time series analysis tool that does not use any predetermined basis functions as is routinely done in wavelet transforms or Fourier transforms. EEMD seeks to determine the intrinsic modes of oscillations (also called Intrinsic Mode Function [IMF]) in the data on the basis of local scale separation. The IMFs are obtained through a sequential sifting process that involves identifying local extrema (which includes both maxima and minima). These local extrema are connected with a cubic spline to obtain the upper and lower envelopes. As a preliminary step a "component" is obtained from the difference of the data between the local mean of the upper and lower bound envelopes. This procedure is repeated till the two envelopes are symmetric about zero or within a certain pre-determined tolerance to obtain the "component" as the first IMF. The sifting process is said to be complete when the residue computed as the difference of the IMFs from the original data yields a monotonic function containing one internal extremum from which no more IMFs can be extracted. A particular advantage of this technique over other time series analysis tools is that it can isolate frequencies unambiguously, without any leakage from other frequencies. For further details of the methodology the readers are referred to Wu et al. (2011). EEMD was conducted on all RSM simulations and the observations to isolate the diurnal harmonic. It was found that for the model simulation data, a combination of IMF five and six represented the diurnal precipitation signal. IMF four represented the diurnal signal of temperature in the model

simulation. In the observed precipitation data, a combination of IMF five and four contained the diurnal signal in precipitation and temperature, respectively.

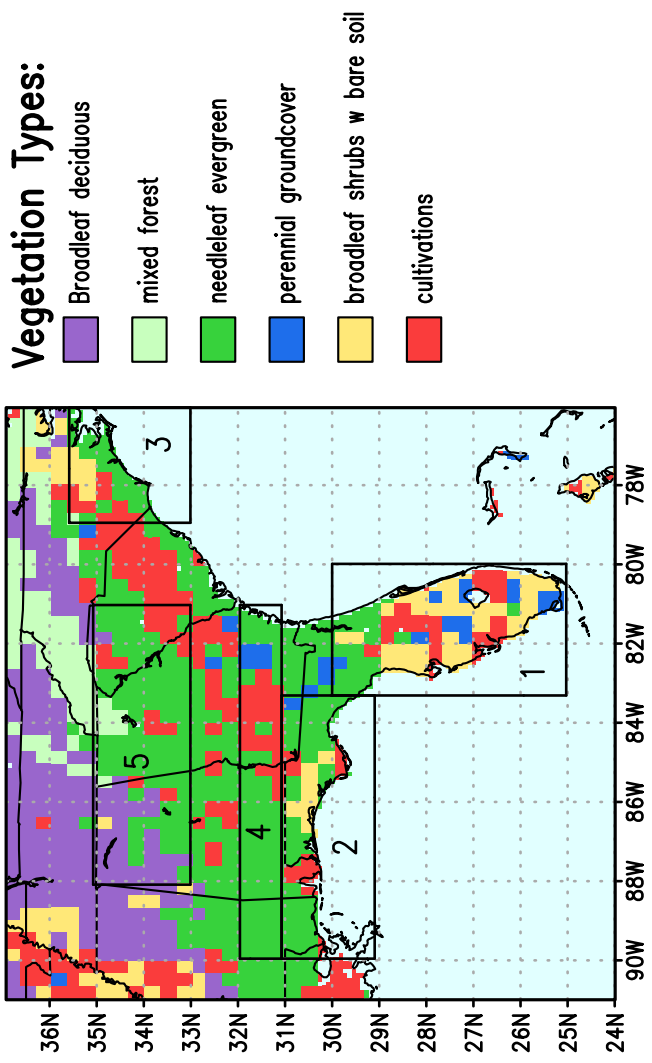

Fig. 1 - Domain and vegetation map used in model simulations. Also included are five sub-regions used for sensitivity analysis.

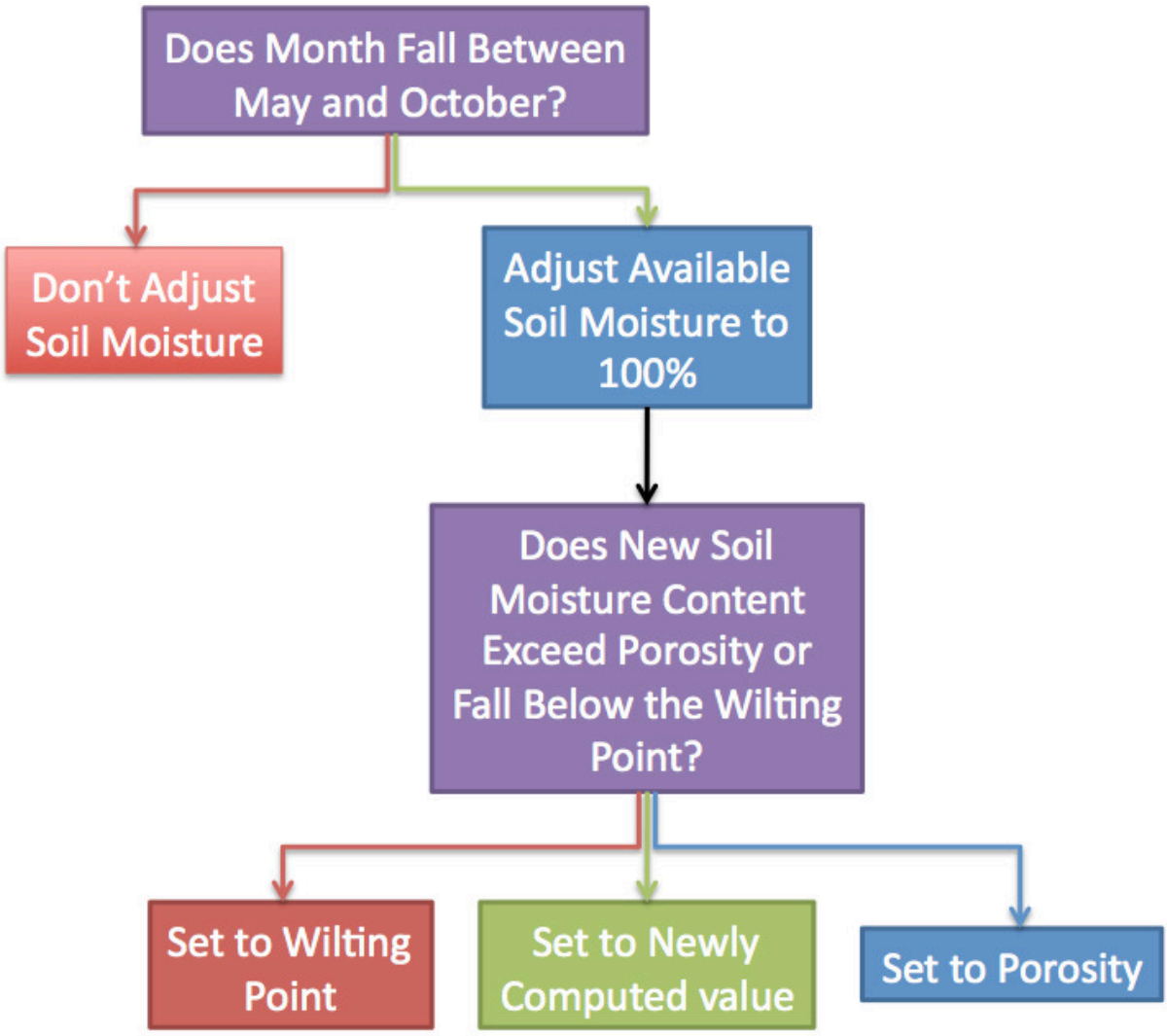

Fig. 2 - Flowchart depicting irrigation parameterization within the model.

CHAPTER 3

RESULTS AND DISCUSSION

3.1 Fidelity and Sensitivity of Simulations to Model Parameterization

The model simulation precipitation data is verified against hourly NCEP Stage IV (Lin and Mitchell 2005) multi-sensor data. On its native polar-stereographic grid, the resolution of Stage IV is 4 km, however when interpolated to a lat-lon grid the resolution becomes 0.1° x 0.1°. When EEMD is performed to isolate the diurnal signal from the raw data, the resolution is further reduced for the purposes of this study to 0.2° x 0.2° in order to reduce computational time. Numerous past studies have used Stage IV data for validation purposes (Tian et al. 2007; Davis et al. 2003; Sapiano and Arkin 2009) and as such we believe the data to be appropriate for use in this study. Because Stage IV was only made available beginning in 2002, our analysis must span the period 2003-2010. This chosen interval is not coincident with our model integration period. However, Dai et al. (1999) noted stationarity in the climatological features of the diurnal variability (which include amplitude, phase and spatial patterns) in regions that displayed strong diurnal variability in precipitation. Furthermore, we are comparing the diurnal climatology across two adjacent decades, and observed trends in diurnal precipitation for the Southeast are small, on the order of a 2 to 4 mm/decade reduction in the rainfall amount (Dai 1999). As such, between the model simulation and observations, we do not expect the changes in the mean monthly climatology to change significantly. Furthermore, on account of using EEMD to isolate diurnal variability, it is not contaminated by variations at other temporal scales. Consequently the objective of this paper is to verify the climatology of the diurnal variations from the six experiments of decade long simulations conducted with the RSM. The validation data for temperature at hourly interval for the period 1997-2007 comes from the North American Land Data Assimilation System (NLDAS)-1 forcing package (Cosgrove et al. 2003) which has a horizontal resolution of 0.25° by 0.25°. The NLDAS-1 forcing package are assimilated from gauge-based observations and fed into the Eta model-based Data Assimilation System (EDAS) (Rogers et al. 1995) with 3-hourly output, which are temporally disaggregated to one-hourly (Cosgrove et al. 2003).

3.1.1 Fidelity of Monthly Averaged Rainfall

Before we proceed to examine the diurnal variations in the various model simulations, we begin with analyzing the seasonal cycle of precipitation. Figure 3 depicts the climatological monthly fraction of total annual precipitation from STAGEIV observations. The coastal regions of the SEUS are characterized by a distinct wet summer season in June, July, and August (Fig 3f-h) and relatively dry winter months in November, December, and January (Figs. 3k, l, and a). This is generally the opposite for the northwestern portion of the interior, owing to the progression of frontal systems during the winter, spring and fall months. The root mean square error (RMSE) of the climatological monthly fraction from the various model integrations is shown in Fig. 4. It is seen that over all months, 20CR-KF simulations exhibit highest RMSE (Fig. 4). The RMSE in the monthly fraction of rainfall in 20CR-KF is rather severe in the winter and summer months. This large RMSE in 20CR-KF is followed by those exhibited in 20CR-RAS simulation in the majority of the months. The other 4 simulations are far more comparable in terms of this metric (Fig. 4). In summary these results suggest that the seasonal cycle of precipitation in the regional model simulations over the SEUS is relatively more sensitive to the prescribed large-scale conditions of 20CR than the two cumulus parameterization schemes and the other two remaining global reanalysis forcing used in this study.

To illustrate the spatial distribution of the monthly fraction of precipitation, Figure 5 shows results from the NCEPR2-KF simulation, which was one of the better configurations of the regional climate model (see Fig. 4). For synthesizing the results, we hereafter consider NCEPR2-KF as our baseline integration, which helps us in comparing the rest of the simulations with this integration. The NCEPR2-KF in Fig. 5 generally exhibits a wet bias (in comparison to Fig. 3) throughout the year for most of the regional domain with the exception in February, May, November and December (Fig. A1 in appendix) when the simulation seems to exhibit a dry bias outside Florida peninsula. Despite this model bias, the contrast of the wet (Figs. 5j-l) and dry (Figs. 5f-i) seasons is reasonably well represented in the model simulation. In comparison, the transition season of spring (Figs. 5c-e) shows a larger bias with respect to the corresponding observations (Figs. 3c-e). The biases we see in the winter and transition seasons most likely stem from their comparatively smaller observed contribution of diurnal amplitudes (as seen in Figs. A1a-c;j-l.) In these periods, especially January and March (Fig A3a,c), RSM produces a diurnal amplitude that is too strong (Figs. A2a-e). However in November (Fig. A3k) and Dec (Fig. A3l)

it is too weak relative to observations (Fig. A2k,l). In reality, seasonal means over the winter and transition periods are dictated by transient systems as opposed to the stationary component of the diurnal variations.

3.1.2 Fidelity of Monthly Averaged Diurnal Rainfall Amplitude

After extracting diurnal signals in precipitation and temperature (using the EEMD approach) from the downscaled simulations, monthly averaged diurnal amplitudes in precipitation and temperature were calculated. Because of disparate resolutions of the RSM simulations and the validation data, we used a bilinear interpolation technique in order to fit our model data onto our observed data's grids. We show the climatological mean errors in the diurnal amplitude of precipitation from the NCEPR2-KF simulation (Fig. 6). In this figure we have masked out the differences where they are larger than the standard error of the observed mean diurnal amplitude. The peak of the isolated diurnal harmonic averaged for the month determines the mean monthly amplitude in Fig. 6 for both observations and model simulations. In Fig. 6 we also overlay the timing of the maximum precipitation as a vector, with southerlies being 0000 UTC, southwesterlies being 0300 UTC and so on.

NCEPR2-KF simulates diurnal precipitation amplitude quite poorly in January (Fig 6a), similar to all other configurations (not shown). But the simulation improves significantly in the subsequent months of the year especially in late spring (May), summer and fall seasons when the observed diurnal variations become significant. This improvement is directly related to the strengthening of the diurnal pattern through the wet season, a feature the RSM has been noted to capture well (Stefanova et al. 2012). The phase of the diurnal peak is also poorly simulated in the winter months (Figs. 6a-c) with differences in the phase being of the order of 6 hours in some parts of the domain. Progressing into the warm season, the NCEPR2-KF configuration begins to simulate the diurnal phase of maximum precipitation reasonably well with domain wide biases on the order of one to two hours. The bias in the timing of the maximum precipitation in the transition seasons of spring (Figs. 6c-e) and fall (Figs. 6i-k) seasons is somewhere between 2-6 hours.

Fig. 7 shows the region wide aggregated RMSE of the diurnal amplitude for all the conducted model runs. It is obvious from Fig. 7 that RMSE is significantly higher in 20CR-RAS and 20CR-KF in nearly all months, while the rest of the model simulations seem to display far more comparable RMSE. It should be however noted that observed diurnal variations over the

SEUS in the winter and spring months are significantly lower than the rest of the year (Bastola and Misra 2013). The monotonic decrease in RMSE from the summer months to December likely stems from the model's ability to simulate well the strong diurnal pattern of precipitation in the wet season. An interesting aspect in Fig. 7 is the abrupt increase in RMSE from Dec. to Jan. across all six model integrations. This stems from two reasons - One, the observed seasonal cycle in Fig. A2 exhibits a similar discontinuity with significant weakness in diurnal variation across the domain in Jan relative to Dec. Second, the RSM simulations show similar discontinuity in the seasonal cycle of diurnal variations of precipitation but with December being significantly weaker than January.

3.1.3 Fidelity of Monthly Averaged Diurnal Temperature Amplitude

We also investigated how sensitive the simulations of diurnal amplitude and phase of surface temperature are in the various model simulations of this study. Similar to Fig. 6, Fig. 8 shows the climatological monthly mean error in the diurnal amplitude of the surface temperature from the NCEPR2-KF simulation overlaid with vectors representing the climatological time of observed and simulated maximum surface temperatures. A rather sobering result of this analysis in Fig. 8 is that the diurnal amplitude error in surface temperature in our baseline NCEPR2-KF integration is larger than the standard error of the observed diurnal amplitude in the winter and fall seasons outside of peninsular Florida. However, the climatological diurnal amplitude error in the NCEPR2-KF (Fig. 8) recovers in mid-spring and sustains it through the early fall season. It is however possible that the discrepancy in the model simulations of the diurnal amplitude of the surface temperature is also being seen as a result of the differences in the resolution of the observations and the simulations, which can easily reflect in the elevations of the topography used in the ~28 km grid resolution of the NLDAS-1 assimilation model. Furthermore, the diurnal range of precipitation produced by NLDAS-1 poorly validates with independent observation. As a result, there is scope to speculate of a potential bias in the diurnal energy budget present within the NLDAS-1. This suspicion gets further raised when we notice that despite these amplitude errors the model performs comparably far better at simulating the climatological time of diurnal maximum surface temperature throughout the year (Fig. 8). This result is in stark contrast to the results seen in diurnal precipitation, in which months with well-simulated times of maximum rainfall also had the smallest errors in simulated amplitudes. It is also possible that the chosen parameterizations have inherent shortcomings with respect to diurnal ranges of temperatures.

The largest biases are on the order of one hour in coastal areas and around the Appalachians. Figure 8 shows the aggregate RMSE of the diurnal amplitude of the surface temperature over the whole domain from all model integrations. We again note that 20CR configurations produce the highest RMSE throughout the year (likely owing to large-scale biases from the lateral boundary which is discussed in the conclusions.) We also see that 20CR-RAS performs comparably to other configurations in the summer, when diurnal variations in rainfall are most pronounced.

3.1.4 Sensitivity to Cumulus Parameterization and Lateral Boundary Condition

In summary our analysis so far indicates that the climatological diurnal variations of the precipitation and surface temperature in the model integrations forced by 20CR are significantly different (and inferior) to all other model integrations. Furthermore, when excluding 20CR simulations, distinguishing the relative fidelity of the diurnal variations of the surface temperature and precipitation from the other four model integrations produces results that are inconclusive.

In order to understand how changing the lateral boundary conditions and convection scheme impacted the diurnal variation of the regional climate model simulations, we objectively computed sensitivity (S; Figs. 10-12) with respect to the baseline model integration as:

$$S = \left| \frac{(V_b - V)}{(V_b - V_{obs})} \right| \text{----------(1)}$$

where, V could be any one of the three variables: diurnal amplitude of precipitation, diurnal amplitude of surface temperature, phase of diurnal maximum of precipitation from any of the five model runs besides the baseline integration, Vb and Vobs are the corresponding variable from the baseline integration and observations respectively. In other words, S is the fraction of the relative change of the variable in question between two model integrations with respect to the corresponding departure of the baseline experiment from the observations of the variable. For the purposes of this discussion, we are interested in seeing how model simulations change under differing configurations. Since S can have a wide range of values depending on the fidelity of the simulation, we decided to plot the logarithm of S to capture a larger range of its values. This required us to compute its absolute value as shown in equation 1. We computed S as an average for the sub-regions (outlined in Fig. 1), in order that we may assess if our model is more sensitive

to lateral boundary forcing and convection scheme under regimes with different drivers of diurnal variability. As noted in section two, we subdivided our region (see Fig. 1) into the Florida peninsula (Region 1), Gulf of Mexico coast (Region 2), Carolina coast (Region 3), non-mountainous interior (Region 4), and mountainous interior (Region 5).

Fig. 10 shows the sensitivity of the diurnal precipitation amplitude to lateral boundary forcing and convection scheme. A value of S close to 1 indicated less sensitivity, while large deviations from 1 would suggest high sensitivity. Deviations beyond 50 are not shown in the figure. A value very close to zero would suggest that the experiment integration is better than the baseline integration. Very large values of S would suggest higher fidelity of the baseline integration relative to the experiment integration. 20CR forced RSM experiments appear to have the highest sensitivity values for both KF and RAS as an average, though no one conclusive statement can be made about them as a whole. In the month of February, for instance, sub-regions 2, 4 and 5 exhibit strong sensitivity to 20CR configurations, but this feature does not persist in March. In June, sub-region 1 appears to be extremely sensitive to lateral boundary condition and cumulus parameterization choice, a feature seen only again in September. In most other months, however, it appears that all non-20CR configurations perform similarly over most regions, exhibiting very low sensitivity to configuration. We find that most sub-regions exhibit sensitivity patterns similar to the region as a whole in the winter and early spring months, when the diurnal amplitude is weaker than the rest of the year in the SEUS,. However in the summer and fall months, the heterogeneity of the various sub-regions in terms of its topography, vegetation distribution, proximity to coasts, and its geographic location (longitude and latitude) make the sensitivity patterns look more dissimilar to the corresponding pattern for the region as a whole.

Next we examine the sensitivity of the phase of the diurnal maximum in precipitation (Fig 11). In order to prevent artificial bias in the results when precipitation occurs at 2300 UTC in comparison to 0000 UTC, our analysis seeks the minimum difference in time using the 24-hour clock. As in Figure 9 above, we see the greatest average sensitivity in configurations using 20CR, though again this is not an annual or sub-region persistent phenomenon. In the summer months, we see that phase is strongly sensitive to convection scheme choice in sub-regions 1 and 2. In the spring months of March and April a majority of the sub-regions demonstrate sensitivity to both changing the convective parameterization and boundary condition. Into November and

December it appears that the RSM simulated phase of diurnal precipitation is relatively insensitive to convection scheme and boundary condition choice. As seen in the previous figure, the sensitivity patterns of diurnal phase for the various sub-regions are similar to that for the whole domain in the winter months. In examining the sensitivity of the amplitude of diurnal amplitude of temperature (Fig 12) we find that for all months, the model is generally insensitive to choice of both lateral boundary conditions and convection schemes, except in isolated cases using 20CR configurations (June, July and August for sub-regions 3, 4 and 5.) We further note that sub-region 3 and 4 also exhibit sensitivity to choice of convection scheme, as ERA40-KF sensitivities are low whilst ERA40-KF RAS sensitivities are high.

In order to understand these sensitivities further we computed the moisture budget for the various regions. We will focus our moisture budget discussion on areas and experiments that displayed some of the highest sensitivity. In August, ERA40-RAS produced high values of sensitivity in the diurnal amplitude of precipitation in sub-region 4 when compared to the baseline integration (Fig. 10). Again in August, NCEPR2-RAS produced a high value of sensitivity in the diurnal phase of precipitation over sub-region 1 (Fig. 11). Finally, in September, sensitivity was high when computed against 20CR-KF in sub-region 1 (Fig. 10). The diurnal variations of each term of the moisture budget for these regions and experiments are shown in Figure 12. The moisture budget equation analyzed for this figure takes the form of:

$$\frac{\partial Q}{\partial t} = -\nabla \bullet M + E - P \quad \text{-------} \quad (2)$$

where,

$$Q = \frac{1}{g}\int_{p_s}^{p_{top}} q\,dp \qquad (3)$$

and

$$\nabla \bullet M = \nabla \bullet m + \nabla \bullet m' \qquad (4)$$

$-\nabla \bullet m$ is defined as the stationary moisture flux convergence,

$$= -\frac{1}{g}\int_{p_s}^{p_{top}} \nabla \bullet \bar{\vec{V}}\bar{q}\,dp \qquad (5)$$

and $-\nabla \bullet m'$ is defined as the transient moisture flux convergence,

$$= -\frac{1}{g}\int_{p_s}^{p_{top}} \nabla \bullet \overline{\vec{V}'q'}dp \qquad (6)$$

with E and P defined as the surface evaporation and precipitation respectively. The transient moisture flux convergence is computed as a residual. It may be noted in Fig. 12 that positive (negative) values of $-\nabla \bullet M(= -\nabla \bullet m - \nabla \bullet m')$ represent moisture flux convergence (divergence).

In Fig. 13 we see that at the nadir of the diurnal cycle of precipitation, all terms of the moisture budget are small and comparable in all configurations. The largest differences from 0000 UTC to 1200 UTC between the model experiments are in the transient moisture flux convergence and surface evaporation terms. As we approach the diurnal zenith (around 2000 UTC) the moisture budget reveals that there is a moderate increase (decrease) in the vertically integrated stationary moisture flux convergence (local storage) and steep increase in local evaporation, precipitation, and the vertically integrated transient moisture flux divergence in all simulations. In August over sub-region 1, comparing these moisture budget terms between the NCEPR2-KF and NCEPR2-RAS we find that the largest differences stem in the transient moisture flux divergence term followed by those in precipitation and evaporation (Fig 13e). This assertion is also true for September in sub-region 1 between the NCEPR2-KF and 20CR-KF experiments (Fig 13f). In sub-region 4 however, noted for its sensitivity in diurnal precipitation amplitude, the difference in evaporation is small between NCEPR2-KF and ERA40-RAS (Fig 13d). The difference in the transient moisture flux divergence term remains large, however, owing to large difference in precipitation. The differences in the local storage of the moisture in the column and the stationary component of the vertically integrated moisture flux convergence are relatively small among all sub-regions, months and simulations shown in Fig. 13. In other words, this budget reveals that the large sensitivity in both the diurnal amplitude and phase of precipitation found between the baseline model integration, NCEPR2-KF, and all other experiments (Figs. 10, 11) could be traced to the differences in the transient moisture flux convergence. The changes in precipitation from the simulations also entail changes in local storage. It is not surprising to note that the stationary components of the moisture flux convergence in the model integrations are comparatively similar. This is because the prognostic

variables from the boundary conditions are more likely to be similar in their stationary components than their transient components. The source of these disparities in the transient scale likely stems from the noted propagation of biases from the 20CR reanalysis packages, which include a persistent cold bias along the northern portion of the domain, and warm bias along the gulf coast (Dinapoli and Misra 2012). Both these features can cause underproduction (overproduction) by stabilizing (destabilizing) the atmosphere in the respective regions and from its impact on the large-scale meridional temperature gradient.

3.2 Impact of an Extreme Case of Irrigation on Southeast US Climate

In this segment of the analysis, we analyze results from IRR100 model run. Within the domain, monthly averaged added water during the irrigated period was extreme, often exceeding an average of 200m of added moisture over the growing season (Fig 14). However this added water was a consequence of keeping the soil moisture in the root zone at field capacity, which is often the case when growing crops like Rice Paddy. Most water was added to the soil in the month of May (Fig 14a), which is to be expected, as May is a climatologically drier period than the summer months. As the wet summer season of SEUS was established and diurnal variability of rainfall became prominent, the amount of moisture added reduced over much of the region. Still, it remained incredibly high in magnitude. The amount of water added highlights a critical aspect not previously addressed in similar irrigation studies: Few, if any, studies have indicated the volume of water added to the soil column.

3.2.1 Irrigation Impact on Precipitation

For the monthly climatology, irrigation manifested in precipitation (IRR100-CTL) in a mostly local manner, both temporally and spatially (Fig. 15). The impacts of irrigation were most pronounced during the irrigated period (Figs. 15e-j). During this time, there was a pronounced decrease in precipitation above and adjacent to irrigated cells, on the order of 1 mm/day. The sole exception is in June, in which most of the region has an increase in precipitation. There was also an increase in precipitation (again on the order of 1 mm/day) in non-irrigated areas. It is postulated that these patterns are connected via some physical mechanism-- likely owing to enhanced atmospheric stability stemming from the altered thermal properties of the moistened surface. These will be discussed in greater detail in section 4. Irrigation impacts on the SEUS

climate also appeared to manifest during the non-irrigated season as well (Figs. 15a-d;k,l), though the changes do not seem to follow the same patterns as during the irrigated months. While this study makes no attempt to attribute a physical mechanism to the off-season changes, we hypothesize that the mechanisms could be analogous to other drivers of precipitation change, such as translation speed and intensity of passing cold fronts.

Changes in diurnal precipitation (IRR100-CTL) mirrored those of monthly averaged during the irrigated period (Figs. 16e-j). This was an expected response as diurnal precipitation became stable and pronounced during the irrigated period. Despite changing the amplitude of diurnal precipitation, irrigation did not appear to have an impact on the phase of the diurnal amplitude. This suggests that the changes in precipitation owing to irrigation are not led by one particular mechanism, and instead represent an integrated change (which will be further discussed in Section 4). From November to April, the changes in diurnal precipitation lack appreciable spatial coherence in both change in amplitude and phase (Figs. 16a-d;k,l). This is owing to relatively weak diurnal variations of precipitation during non-irrigated months in the SEUS.

To understand the nature of precipitation changes caused by irrigation, we binned precipitation events by magnitude (Fig. 17). Bins are separated into 1 mm/day intervals. We confined our binning to areas over irrigated cells only, as the impacts of irrigation are primarily seen locally in space. In the irrigated season, with the sole exception of June, there is a decrease in 0-10 mm/day and 20+ mm/day events. In each of the irrigated months, there are isolated bins where increases in events are seen, however these are overwhelmed by the net decrease in other rainfall events. Again it is noted that June generally sees an increase in most precipitation events. The response in non-irrigated months is less cohesive; in January, and November there is a net decrease in nearly all precipitation events, yet in February there is a net increase. Thus, these results suggest that there it is a decrease in frequency of small precipitation events (on the order of 1-10 mm/day) that drive the reduction in rainfall during the irrigated season, over irrigated cells.

In order to further understand the reduction in rainfall, we computed moisture budgets over all irrigated cells during the irrigated period (Fig. 18). Terms of the moisture budget are computed as in Selman and Misra (2015a). At the onset of the irrigated period, IRR100 precipitation remains close to CTL, however there is an increase in evaporation and a

corresponding decrease in runoff beginning around 1400 UTC. There is also a slight increase in stationary moisture flux convergence. In May, the changes in evaporation and runoff seem to balance each other, causing the IRR100 residual transient moisture flux convergence (TMFC) to remain close to CTL. From June to August (Figs. 18f-h) the reduction in runoff is greater than the increase in evaporation with an associate increase in TMFC 1600 UTC (smaller negative TMFC in IRR relative to CTL in Figs. 18f-h means there is less transient moisture flux divergence in the former). Therefore despite a net reduction in moisture flux divergence and an increase in surface evaporation in the irrigated cells in IRR100 relative to CTL, there is a net reduction of rainfall in the former relative to the latter, which at the outset is counterintuitive. However we will elaborate further on this reduction in the irrigated cells later in Section 5 after discussing the differences in surface temperature.

3.2.2 Irrigation Impact on Temperature

Because irrigation has altered precipitation, and thus by extension cloud cover and radiative and turbulent fluxes, we should expect to see a response in average temperatures. Monthly averaged maximum two-meter temperatures have a noticeable decrease over the irrigated period, with reductions on the order of 0.5 K (Fig. 19). In contrast with precipitation, the effects of irrigation are readily apparent in non-irrigated months, though the decreases in monthly average temperatures are small compared to the changes found in the irrigated months. Outside of the irrigated areas and across all months, it is difficult to make a coherent deduction on change between IRR100 and CTL (except near the western and northern boundaries of the regional domain; Fig. 19). In order to determine the cause of this change in the mean surface temperature between the IRR100 and CTL integrations, we begin by analyzing the diurnal maximum temperatures (Fig. 20) and the diurnal minimum temperatures (Fig. 21).

During the onset of the irrigated period (May), diurnal maximum temperatures change (IRR100-CTL) slightly except in Florida, where temperatures rise substantially in IRR100 relative to CTL (Fig. 20e). In fact, across the entire year, surface temperatures over Florida increase, likely owing to the corresponding reductions in precipitation seen in Fig. 16. By reducing precipitation we have also reduced cloud cover (Fig. 21) and increased insolation. As we will discuss in Section 4, into June, many of the irrigated cells in the northeastern portion of the domain cool in IRR100 compared to CTL, despite the corresponding reduction in precipitation (Fig. 20f). However, as the irrigated season progresses, localized warming in

diurnal maximum temperature is seen over the irrigated cells, again owing to a reduction in precipitation and cloud cover in IRR100 relative to CTL. In conjunction with the increase in cloud cover in other non-irrigated areas (Fig. 21), there is an overall reduction in diurnal maximum temperatures over most non-irrigated areas during the irrigated months with the exception in September (Fig. 20i). During non-irrigated months there is moderate reduction in diurnal maximum temperature in the IRR100 run (Figs. 20b, c, j, k, and l), owing primarily to overlapping increases in low cloud coverage (Figs. 20b, c, j, k, and l). Throughout the year, the phase of the diurnal maximum temperature does not change significantly between IRR100 and CTL. These patterns of change in diurnal maximum temperatures between the two model integrations are reversed over Florida in analyzing the changes in diurnal minimum temperatures (Fig. 22). Over irrigated cells, the differences in the diurnal minimum temperature between IRR100 and CTL is not as systematic, with months of July (Fig. 22g) and August (Fig. 22h) showing some cooling while in May (Fig. 22e) and June (Fig. 22f) showing some warming in IRR100 integration. Areas of warming and cooling are both present in areas of cloud cover reduction, thus it becomes necessary to break the energy budget down further to understand the mechanisms of change. Interestingly, these analyzed changes do not reconcile the changes in seasonal average surface temperatures seen in Fig. 19, which exhibit uniform cooling across all irrigated cells. It is likely, then, that the cooling seen in the monthly averages is driven by changes across other timescales. In fact, analysis of all timescales reveals that no one time scale directly contributes to the cooling seen in the monthly averages, implying that irrigation impacts temperatures across all time scales.

In order that we may understand the mechanisms of temperature change we computed the heat budget (Fig. 23) over all irrigated cells and compared it with the CTL simulation. Throughout the entirety of the irrigated period, the largest changes can be seen in the portioning of SHF and LHF. As expected from our above results, LHF increases substantially in IRR (on the order of 100 W/m^2). There is also a moderate increase net shortwave flux during the summer months in the IRR run (Figs. 23f-h), which is to be expected accompanying a reduction in the low cloud cover (Fig. 21). In order to balance these increases, there is a corresponding decrease in the SHF in the IRR integration. However there is a consistent increase in the negative values of the Ground Heat Flux (GHF) in the IRR100 run. The reduction in ground heat flux can be attributed to the increased sub-surface soil moisture. The addition of water to the subsurface soil

(root zone) layers impacts the ground heat flux by introducing a new heat sink at every time step to the surface temperature. Throughout the day, there is a net flux of heat into the sub-surface soil layers (from the top soil to the root zone). During the daytime, this additional downward transport is exceeded by the increase in insolation, driving the daytime warming over the irrigated cells. But at night, with no solar insolation to compensate, the downward heat transport of the GHF drives the surface temperature cooling. However, as noted above, some irrigated cells also undergo a nighttime warming, implying that the altered thermal properties of the darker soil may still play a significant role in driving nighttime warming, as in Kanamaru and Kanamitsu (2008).

3.2.3 Stabilization of the Atmosphere

In order to identify the causes behind the simulated reduction in precipitation and associated adjustments to the surface energy budgets, we analyzed atmospheric stability. For this study we chose to analyze the lifted index (LI). LI is computed by lifting a surface parcel dry-adiabatically from the boundary layer to its lifting condensation level, then moist-adiabatically to 500mb (Bluestein 1993). Negative (Positive) values of LI tend toward atmospheric instability (stability); thus, in the simulated stable atmosphere we should expect higher values of LI in the irrigated run (Fig. 24). Indeed we found that during the irrigated period LI was higher over our irrigated regions (Figs. 24e-h). Notably, in June, there is a substantial decrease in LI over Southern Florida, which in part explains the increase seen in precipitation (Fig. 15f). The increase in LI persists annually, signifying a long-term impact of irrigation in atmospheric stability. However, in months where precipitation variability is primarily driven by transient frontal systems the local stabilization of the atmosphere is overridden by the less-stationary nature of rainfall. In non-irrigated areas there is generally a reduction in the LI, coincident with the simulated increase in precipitation (Figs. 24a-c, f, i-l). A notable exception to this is the month of July, in which there is a near region-wide increase in LI (Fig. 24g). This result appears to be consistent with an overall reduction in low cloud cover (Fig. 21g), though the exact mechanism is not known.

3.3 The Sensitivity of Southeastern US Climate to Varying Irrigation Vigor

In keeping the soil moisture fixed to 100%, an unrealistic depth of water was used (Fig. 25a). This is in stark contrast to the lower percentages, which use a depth measured in the tens of millimeters. The high withdrawal values primarily a result of irrigation being applied at all hours throughout the season, rather than short concentrated bursts throughout the day. However, the values still highlight an important aspect of irrigation being applied to the SEUS: despite a primarily rain-fed agricultural system, considerable amounts of water must be applied to maintain soil moisture at any specific field capacity. As such, establishing catchments or other supplementary sources of water will become necessary supplements should future crop growth require extensive irrigation.

3.3.1 Sensitivity of Seasonal Rainfall

Throughout the irrigated season, irrigation appears to have a reducing effect on monthly averaged rainfall over the irrigated cells (Figs. 26 and 27). This effect manifests at even low levels of irrigation vigor (Figs. 26a-f) and appears to be most pronounced in either the months of July or August. The reduction in precipitation appears to manifest primarily over irrigated areas, and steadily increases in both areal coverage and magnitude as irrigation vigor is increased. Importantly, we find that the spatial impact of irrigation is primarily local, with reductions in rainfall collocated with grid cells in which irrigation is applied. Outside of the summer months (i.e., June-August), when the dominant mechanism of seasonal rainfall transitions from local diurnal scales to transient synoptic events, there is a noticeable, albeit weaker, reduction in precipitation over and near irrigated areas. This implies that there is some modification to the properties of transient frontal systems (which will be discussed in further detail in Section 3.3.3.) The reduction in rainfall over irrigated areas persists outside of the irrigated period (not shown,) but is much more spatially incoherent and difficult to attribute solely to the influence of irrigation. Outside the irrigated areas of the regional domain there is an increase in precipitation, though it is difficult to ascribe this solely to irrigation in regions upwind of irrigated cells.

Because summer precipitation in the SEUS is primarily driven by late-afternoon convective activity (Selman and Misra 2015a) we expect that the changes in precipitation stem mostly from adjustments to the diurnal precipitation. Using the ensemble empirical mode decomposition method of Wu and Huang (2011), we were able to decompose total precipitation into its various

temporal components. Following this, we then computed irrigation-area averaged percent changes in precipitation relative to CTL (Fig 28) and found that most of the change in rainfall resides in intrinsic mode function (IMF) 3, which represents the sub-diurnal timescale. This pattern persists across all four IRR runs, implying little sensitivity in the percent magnitude of change to varied irrigation vigor. Further, that the change is seen primarily in IMF 3 strongly implies that irrigation influences precipitation negatively in a two to three time per day fashion, one component of which may be collocated with the diurnal maximum. We also find a small contribution from changes in IMF 4, the diurnal component, implying that irrigation indeed also modifies the nature of afternoon convection, as discussed in Selman and Misra (2015a).

Irrigation reduces precipitation in two primary ways: by increasing the number of dry days, and reducing the number of >1 mm/day events (Fig. 29). The decrease in magnitude follows irrigation vigor quite nicely, with IRR100 seeing the largest increase in 0 mm/day rainfall events (or dry days), and the change steadily decreasing until IRR50. In IRR25 there is an increase in dry days, which is roughly 50% that of IRR100. This pattern persists into the 1-4 mm/day range, with IRR100 seeing the largest reduction, and a substantial separation between IRR50 and IRR25. This noticeable jump could likely be related to the drainage of water in the IRR25 runs, a feature not seen in any of the other three simulations.

We have also analyzed the differences in the moisture budget (Fig. 30) (averaged over all irrigated cells) to determine if any particular term exhibits sensitivity to varied irrigation vigor. Throughout the day, precipitation is again seen to reduce relative to CTL (Fig. 30a). However, as irrigation vigor increases, precipitation magnitude further decreases, with a considerable decrease from IRR25 to IRR50. Evaporation (EVAP; Fig. 30b) is less clear-cut; though there appears to be a general increase as irrigation vigor increases, IRR100 drops below IRR75. This could be related to differences in incoming solar radiation (discussed below in Section 3b.) Vertically integrated moisture convergence (VCO; Fig. 30c) represents a small portion of the moisture budget's difference between the IRR and CTL experiments, but nonetheless exhibits sensitivity to irrigation vigor. The afternoon and evening peaks in VCO change increase in magnitude as irrigation vigor is increased (Fig. 30c). For the remaining terms, the patterns are less pronounced, though in the case of runoff (RUO; Fig. 30f) there is a considerable gap between the 21Z values in IRR25 and IRR100.

3.3.2 Sensitivity of Seasonal Temperature

Irrigation is also seen to have an impact on seasonally averaged surface temperatures (Figs. 31, 32). There is a pronounced reduction in seasonally averaged surface temperature across all months in all IRR simulations, especially over 25%. These reductions are seen to be primarily local to the irrigated areas. The intensity of the reduction follows irrigation vigor; for instance, in May IRR25 (Fig. 31a) there is no significant decrease in temperature stemming from irrigation, but as vigor increases so too does the magnitude of the reduction (Figs. 31g, 32a, 32g). In fact, this pattern follows across all months, indicating a seemingly linear relationship between reduction in temperature and irrigation vigor.

Because low cloud cover and surface temperatures are tightly related (owing to the availability of energy to heat the surface; Selman and Misra 2015a) we should expect that, much like precipitation, the bulk of the changes to temperature are found in the semi-diurnal timescale. Indeed, this is seen to be the case (Fig. 33). This follows a conclusion from Selman and Misra (2015a) discussing the relationship between increased columnar stability and thus reduced precipitation and cloud cover. Typically this would lead to runaway warming of the surface, however, we can break down the heat budget to determine where excess energy is being transferred (Fig. 34). In contrast to the moisture budget, all terms of the heat budget seem to exhibit consistent sensitivity to irrigation vigor. For instance, net longwave radiative flux (LWF; Fig. 34a) appears to change by about 1 W/m2 with respect to CTL between each of IRR25 through IRR100 experiments. The net positive adjustment to longwave flux indicates that more energy escapes from the surface as irrigation vigor increases. Similarly shortwave flux (SWF; Fig. 34b) increases across all irrigated runs, though the differences between runs seem to be less apparent than for LWF. IRR100's peak difference is however offset from all other runs for reasons unbeknownst to us. Sensible heat flux (SHF; Fig. 34c) decreases as irrigation vigor increases, but this relationship is non-linear. That is, the reduction in SHF is disproportionate to the increase in irrigation vigor. Furthermore, there is a non-linear increase in latent heat flux with irrigation vigor (LHF; Fig 34d). This is to be expected from our analysis of the moisture budget, in which EVAP was seen to increase in the irrigated runs (Fig. 32b).

Finally, we arrive at the major source of cooling in the irrigated runs: the decrease in Ground Heat Flux (GHF; Fig. 34e). The reduction indicates that in irrigated runs, more energy is being transferred to the sub-surface layers, causing a warming in soil temperatures and a net

cooling at the surface. This is a critical mechanism by which irrigation effects surface temperatures. Further, the reductions to GHF follow a similar consistent relationship as surface temperatures; that is to say, as irrigation vigor steadily increases, so too does the reduction to ground heat flux. In other words, the persistent surface cooling from irrigation leads to an increased low-level atmospheric stability increase in convective inhibition (Selman and Misra 2015b) that ultimately results in reduction of precipitation.

3.3.3 Impacts on Transient Frontal Passage

In the SEUS, transient frontal passages can occur in early May and late October (Fig. 35) when the atmosphere is sufficiently baroclinic. Because of irrigation's impact on precipitation and the local thermal environment, we should expect that irrigation would exert an influence on frontal passage events. In order to assess this, a late October frontal passage was isolated within CTL (Fig. 35). One day prior to the passage (Fig. 35a), there was moderate precipitation in the region, with a large cell associated with the front in the extreme western portion of the domain. Conditions in the SEUS appeared to be dominated by an offshore high pressure system off the coast. On the day of frontal passage over the irrigated cells in AL, GA and the Carolinas, (Fig. 35b) conditions worsened, bringing heavy rains on the order of 21+ mm over the day and establishing a dominant low pressure system over the central portion of the SEUS. Following the frontal passage across these irrigated cells (Fig. 35c) temperatures cooled substantially as the front moved over the Florida Peninsula.

We compared these conditions against those from the same timeframe in IRR100 (Fig. 36). In terms of frontal location and translation speed, characteristics varied very slightly compared to CTL. This implies that irrigation has very little effect on the spatial and temporal characteristics of frontal passages. However, there was a marked change in the precipitation characteristics of the frontal passage over the irrigated cells. On the day of the passage, when the front encountered cultivated cells, there was a net reduction in precipitation relative to CTL (Fig. 36b). As the front traveled further east of the irrigated cells, lifting mechanisms became more efficient and created rainfall. Because diabatic heating occurs in a different location than in CTL, a downstream gravity wave-like pattern in precipitation is shown in the differences. On the following day, a similar pattern is found, with reductions in precipitation downwind of the irrigated cells, which is also accompanied by an increase in precipitation relative CTL farther downstream.

In order to assure that these results are not specific to the event discussed above, the precipitation change over an irrigated cell was computed any time a temperature change of -7.5° C was recorded at said cell (Fig. 37). It was found that the average change for all cases of frontal passage in our simulation was a net reduction, on the order of 5-10%. IRR25 reported the lowest decrease in precipitation, which is consistent with results in Section 3a. IRR50, IRR75 and IRR100 were all within 2% of each other, with IRR75 reporting the largest reduction in rainfall. This does, however, appear to be consistent with results seen in previous sections in which IRR75 tended to outpace IRR100 in changes to local climate.

3.3.4 Impacts on Drought and Heat Waves

Because irrigation has such a pronounced impact on climatological precipitation and temperature, we should expect that it manifest in meteorological events, including drought and heat waves, as well. In order to define drought, we consider days in which accumulated daily precipitation exceeds (falls below) 1 mm/day wet days (dry days) (Bastola and Misra 2012). Using this definition, we can then compute the percent difference in number of dry days (not shown) and wet days (Fig. 38). Dry days are not shown because the percent change was insignificant. Again we see a steady decrease in the influence of irrigation on the number of wet days as we reduce irrigation vigor; in IRR25, there is an unsubstantial reduction in the number of wet days with little spatial homogeneity. However, as irrigation vigor is increased, there is additional spatial coverage in reductions, and reduction magnitude becomes more pronounced. As such, we see that irrigation can be attributed for a worsening of drought in an area, a somewhat ironic conclusion considering irrigations function in crop growth. This could potentially create difficulties in water storage for irrigation purposes, as the primary source of irrigation water would considerably reduce.

We then check to see if irrigation, which reduces local temperatures, has an impact on heat waves in an area. In order to do this, we define heat waves as three or more consecutive days in which the daily maximum temperature exceeds the 97.5 percentile of the seasonal temperatures in summer (Russo et al. 2014). Once we have done this, we then compute the difference in threshold temperature for each irrigation simulation (Fig. 39). Irrigation indeed reduces the threshold temperature for what constitutes a heat wave substantially, indicating that more heat wave days are possible under an irrigated regime. Again, as with wet days, there is a steady increase in spatial coverage of the reduction, however the magnitude does not seem to

change significantly much past IRR50. While an increase in heat wave days seems harrowing, it is important to note that the most significant aspect of a heat wave is its human impact. As the intensity of these new heat waves would be quite modest, akin to typical warm summer day temperatures, the human impact would be small. In fact, if we were to fix our CTL criteria as the metric for which a heat wave is defined, we would see a substantial reduction in the number of heat wave days over and near irrigated areas (Fig. 40). This reduction is helpful, as it reduces overall crop stress and can aid in the growth of numerous different types of crops in the region.

Table 1: Name of the conducted model experiments showing the choice of convection schemes and global atmospheric reanalysis used in each experiment

Convection Scheme	Global Reanalysis	2OCR	NCEPR2	ERA40
Kain-Fritsch (KF)		20CR-KF	NCEPR2-KF	ERA40-KF
Relaxed Arakawa Schubert Scheme (RAS)		20CR-RAS	NCEPR2-RAS	ERA40-RAS

Table 2: List of global atmospheric reanalysis packages used as lateral boundary conditions for the regional climate model simulations

Global Reanalysis	Reference Literature	Spectral Truncation	Vertical Levels	Assimilated sea surface temperature
NCEP-DOE R2	Kanamitsu et al (2002)	T62	28	Merged HadlSST1.1 (Rayner et al. 2003) and NOAA Oiv.2 SST (Reynolds et al. 2002) (AMIP II SST; Hurrel et al. 2008)
ERA40	Uppala et al. (2005)	T159	60	HadlSST1.1 (1958-1981) (Rayner et al. 2003) & NOAA Oiv.2 SST (1981-2001) (Reynolds et al. 2002)
20th Century Reanalysis	Compo et al. (2011)	T62	28	HadlSST1.1 (Rayner et al. 2003)

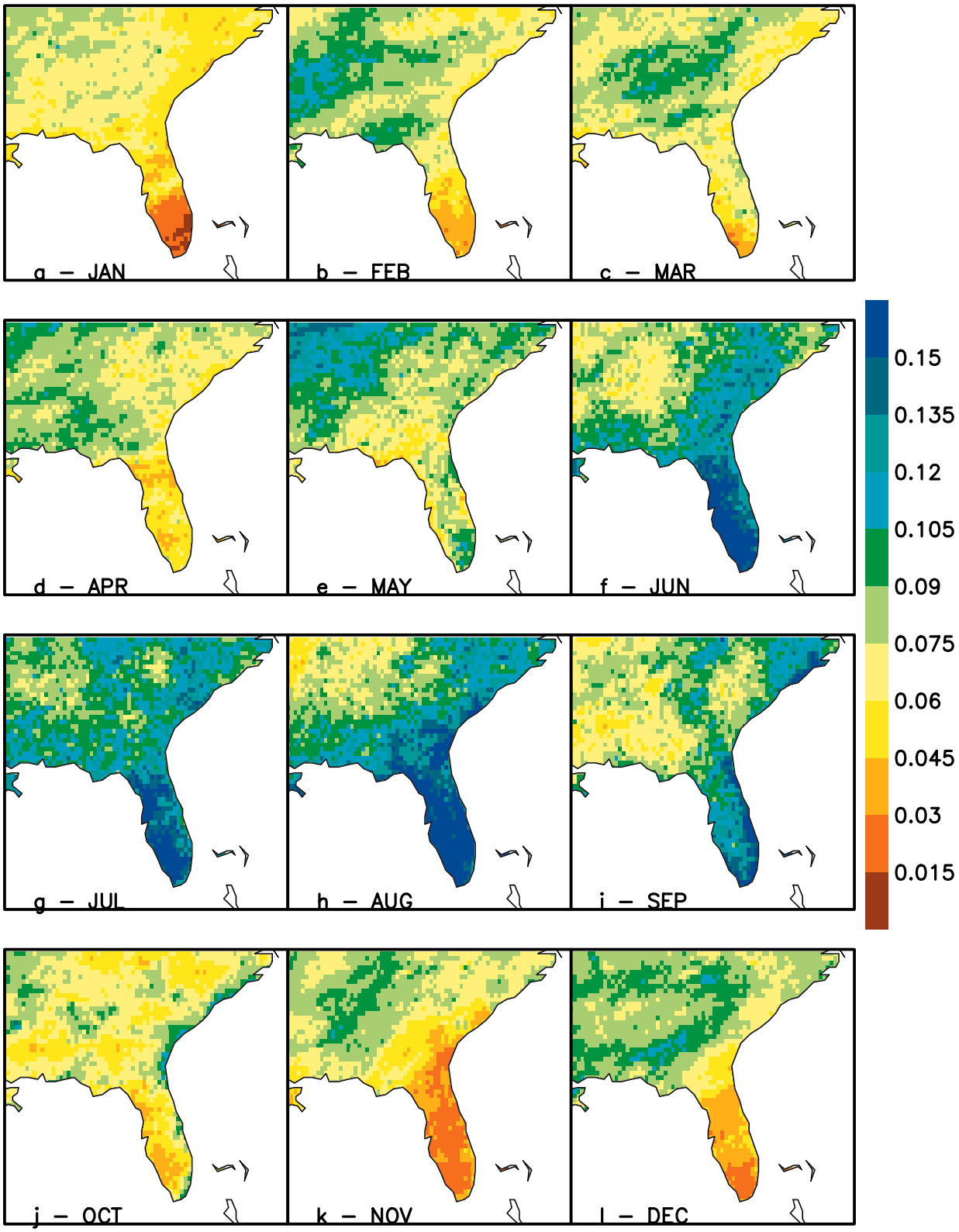

Fig. 3 - The fraction of the annual total precipitation for all months from STAGEIV observations. Unitless

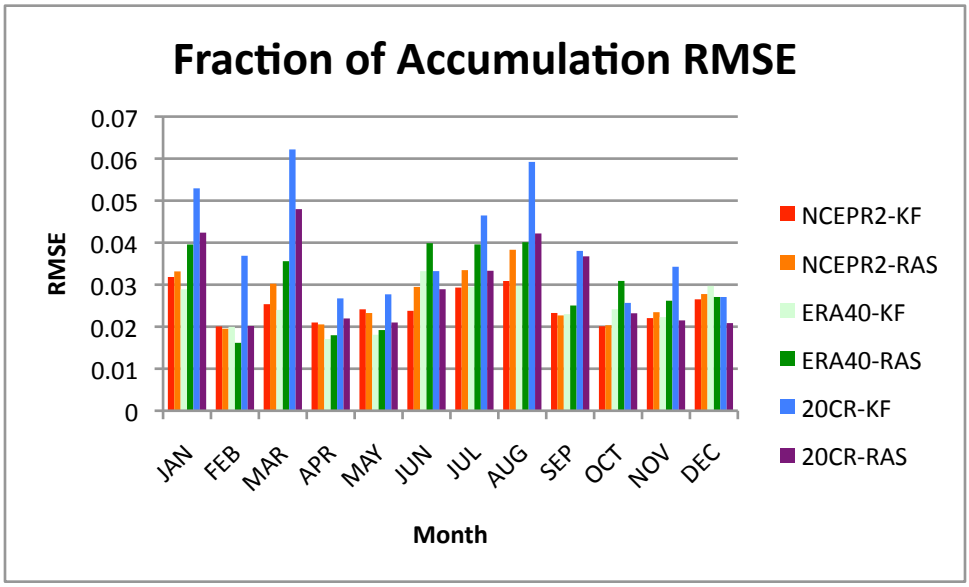

Fig. 4 - The domain wide RMSE of the climatological fraction of monthly rainfall from the six regional model integrations. Unitless.

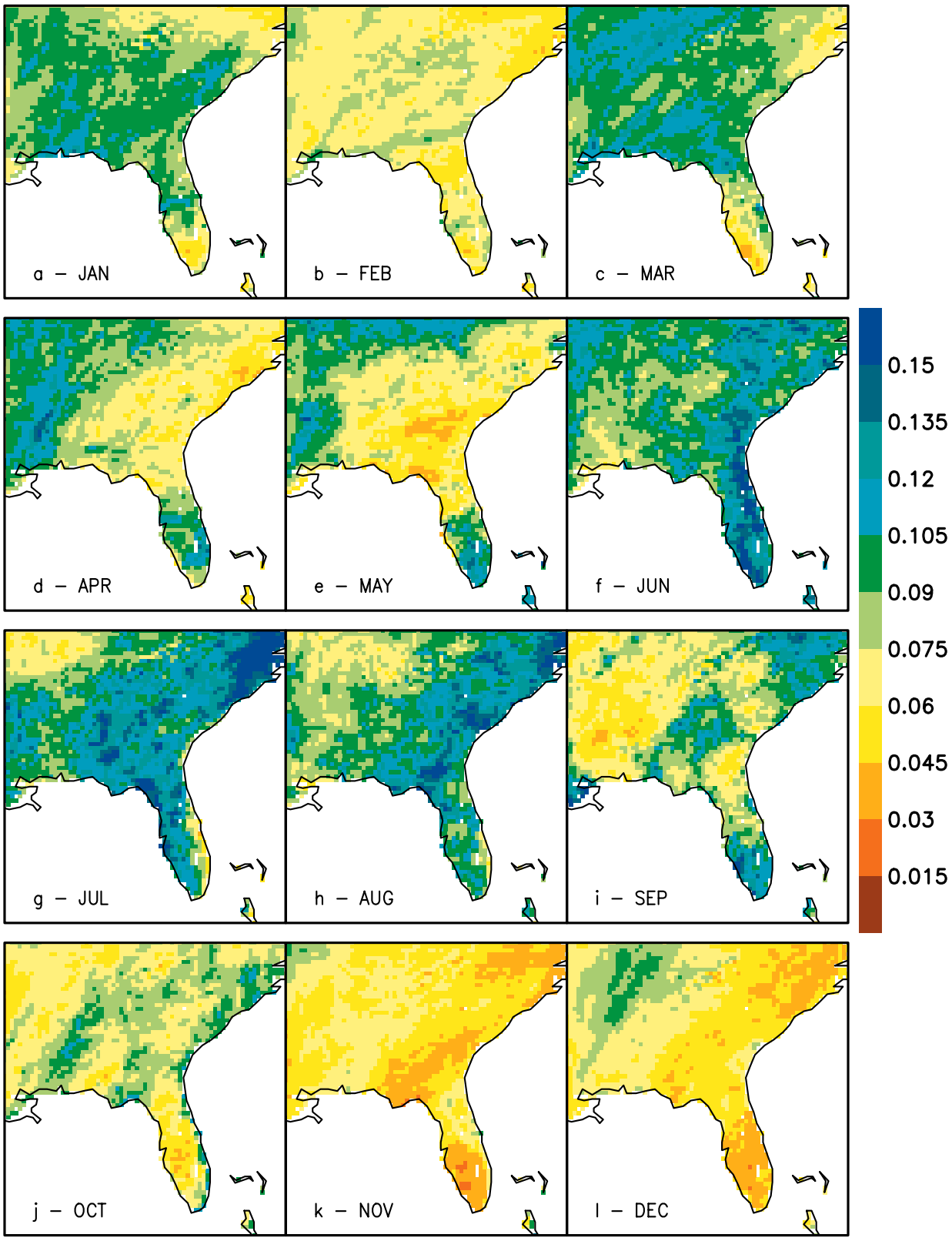

Fig. 5 - As in Fig. 3, but for NCEPR2-KF. Unitless.

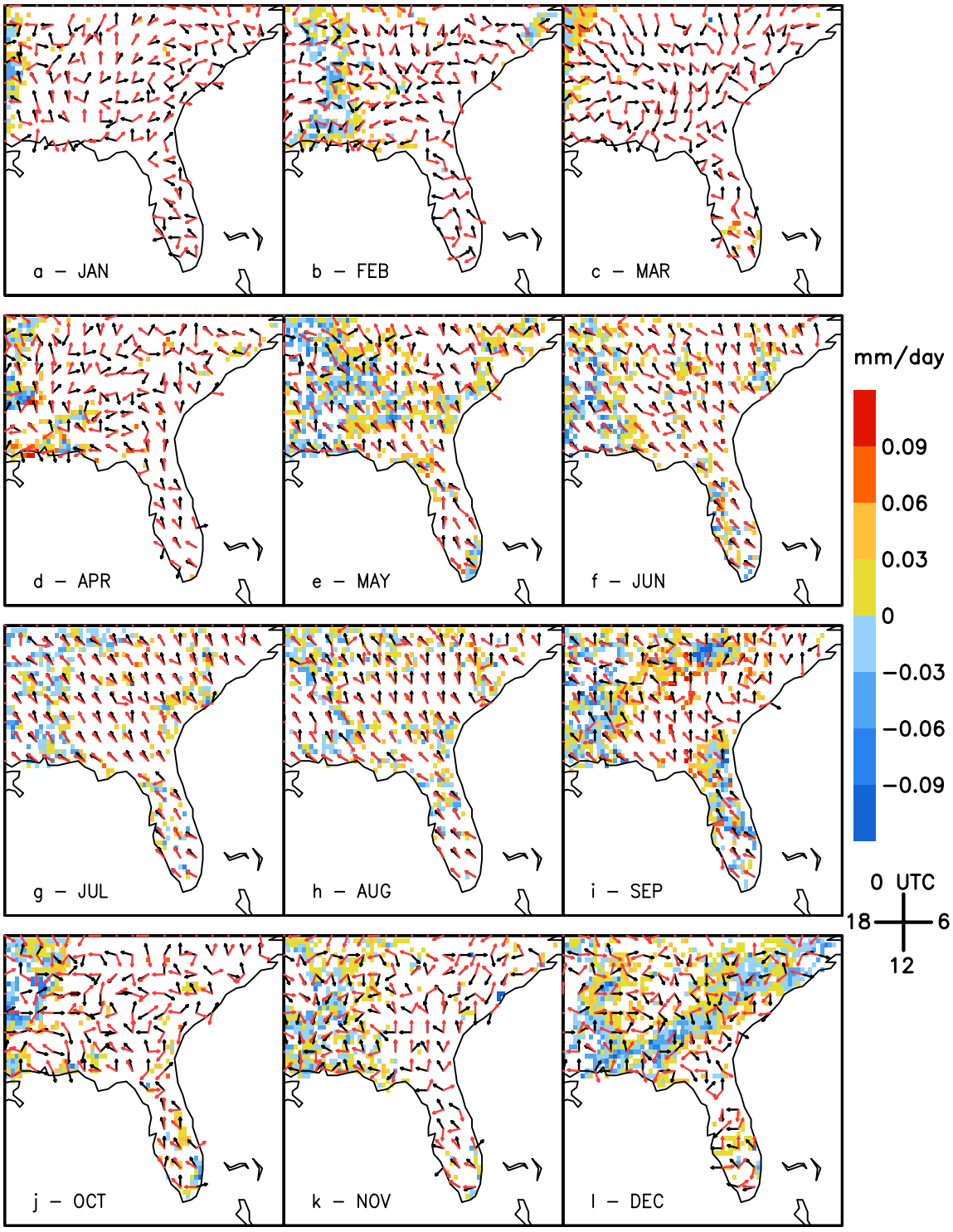

Fig. 6 - The climatological diurnal amplitude error in mm day^{-1} of NCEPR2-KF. The values of these errors are masked out when they exceed the standard error of the observational mean diurnal amplitude. The overlaid vectors denote the simulated (red) and observed (black) time of maximum precipitation. Southerly vectors denote 0000 UTC, westerly 0600 UTC and so on. When only one of the vectors is seen then simulation and observation timing are coincident.

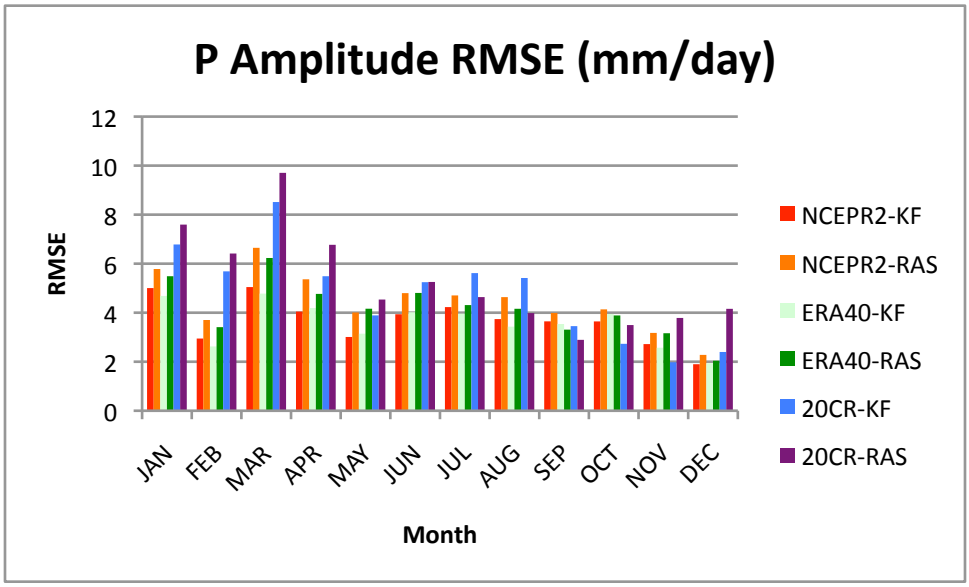

Fig. 7 - The domain wide RMSE of the simulated diurnal precipitation amplitude from all six model integrations.

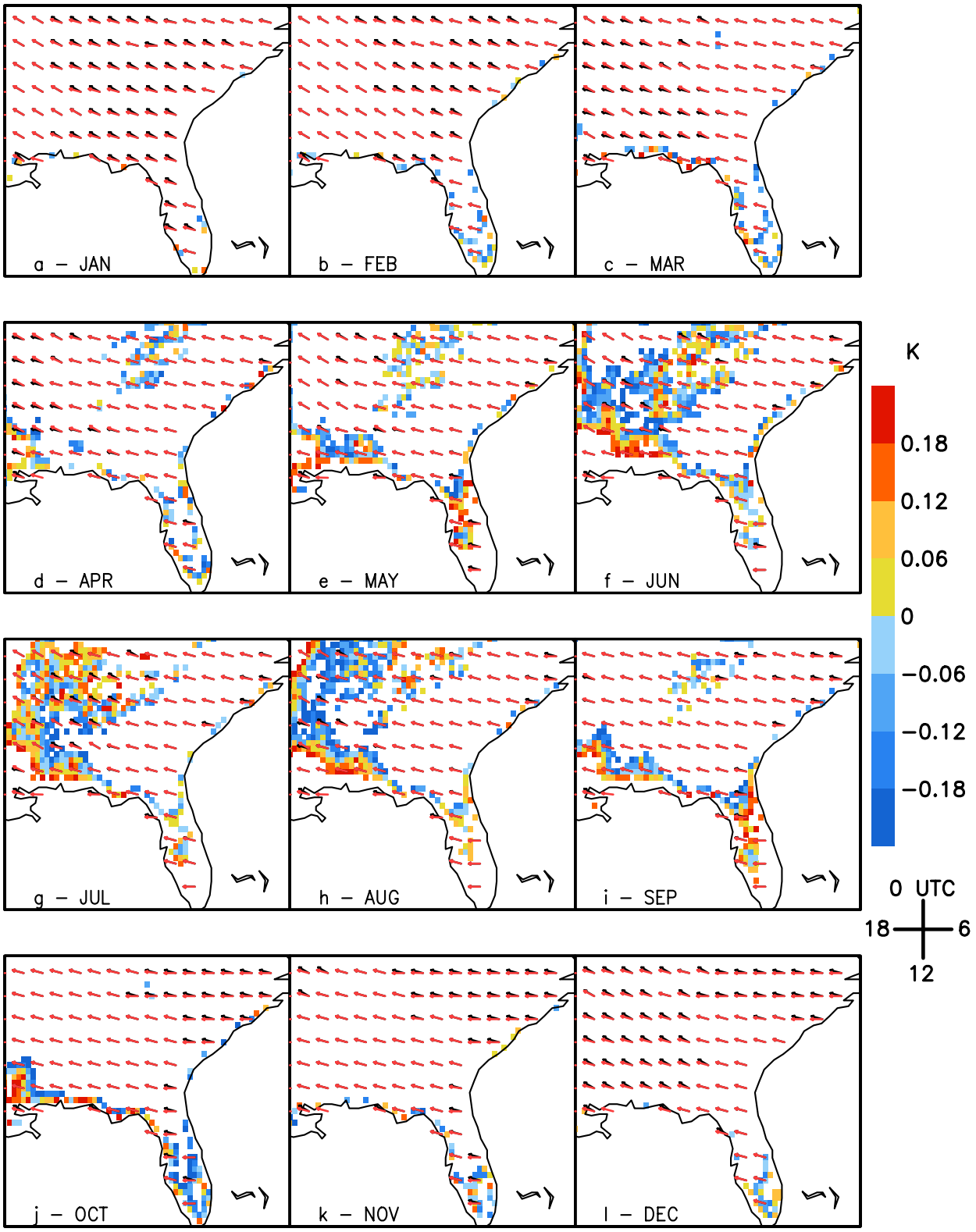

Fig. 8 - As in Fig. 5, but for the diurnal temperature amplitude error (Kelvins.)

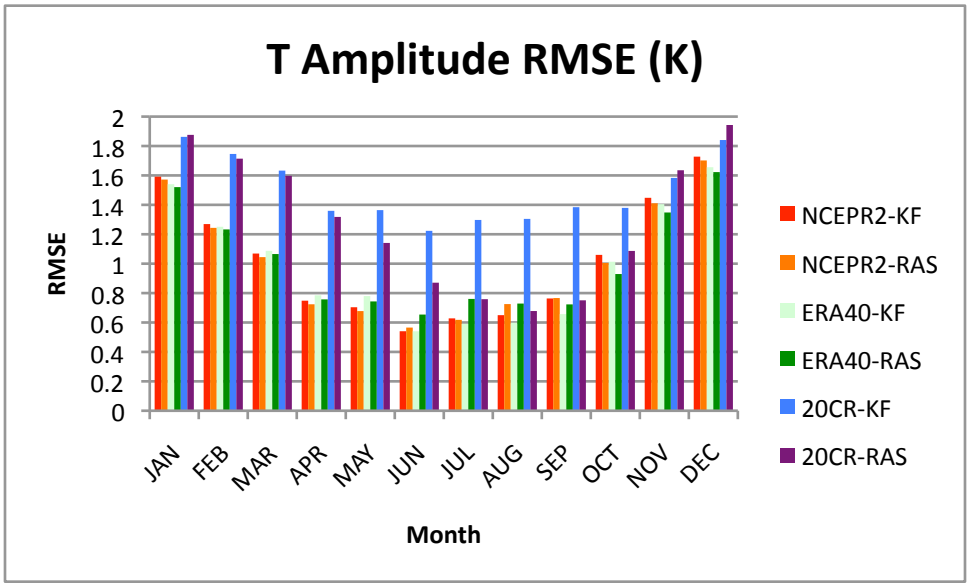

Fig. 9 - As in Fig. 7, but for diurnal temperature amplitude

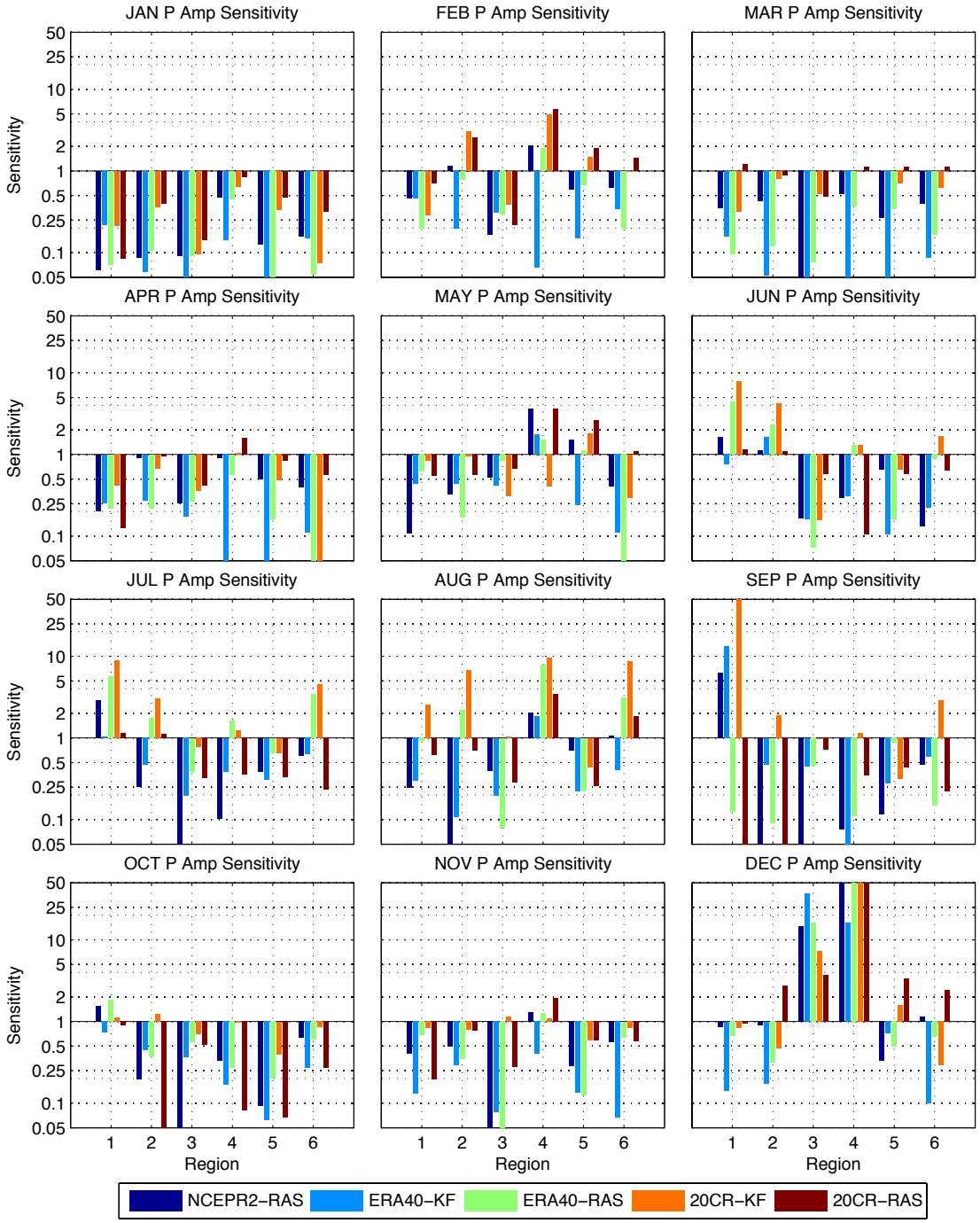

Fig. 10 - The climatological sensitivity (see text) of the diurnal precipitaiton amplitude using NCEPR2-KF as the baseline integration for various sub-regions indicated in Fig. 1.

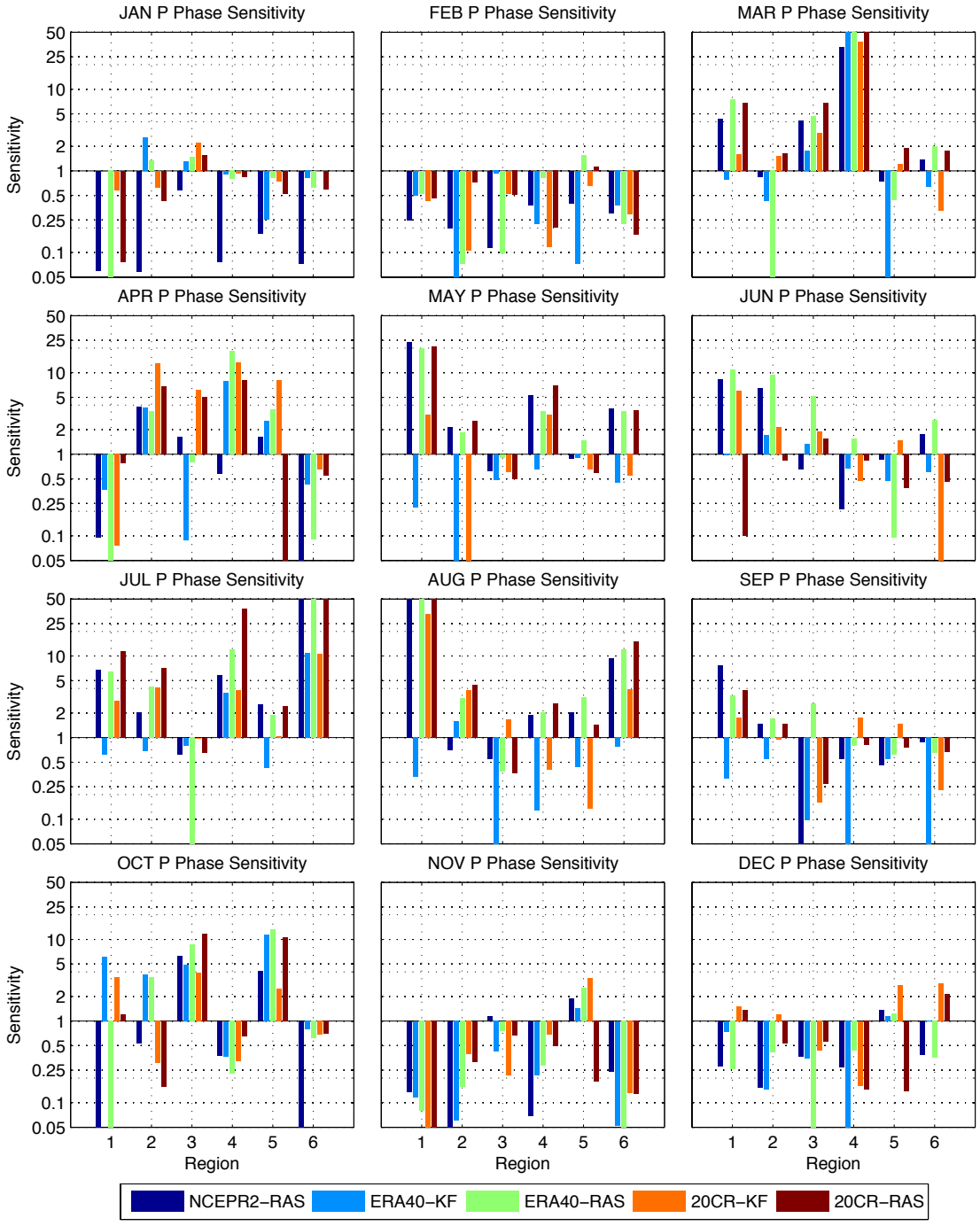

Fig. 11 - As in Fig. 10 but for timing of climatological maximum in diurnal precipitation.

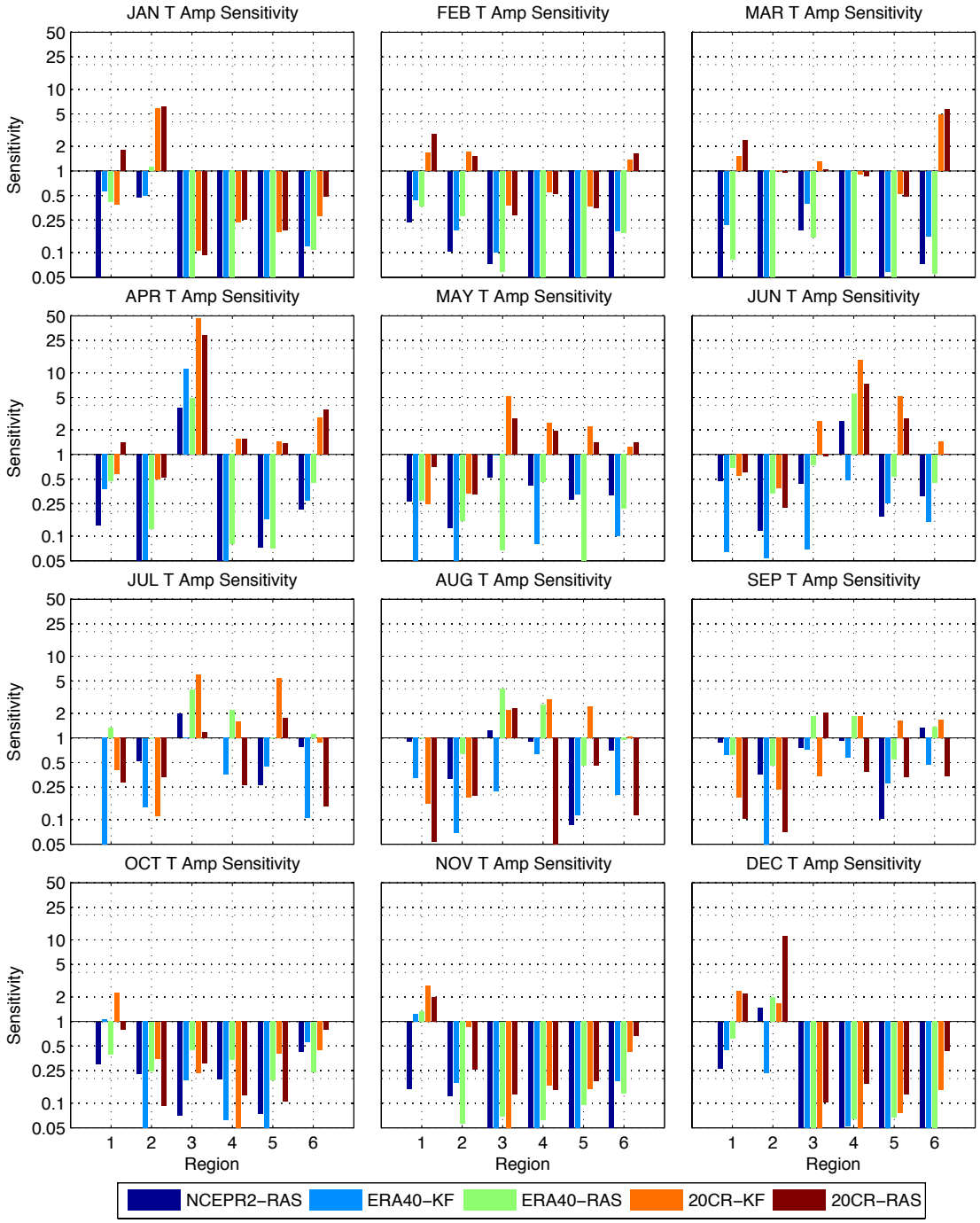

Fig. 12 - As in Fig. 10, but for diurnal temperature amplitude.

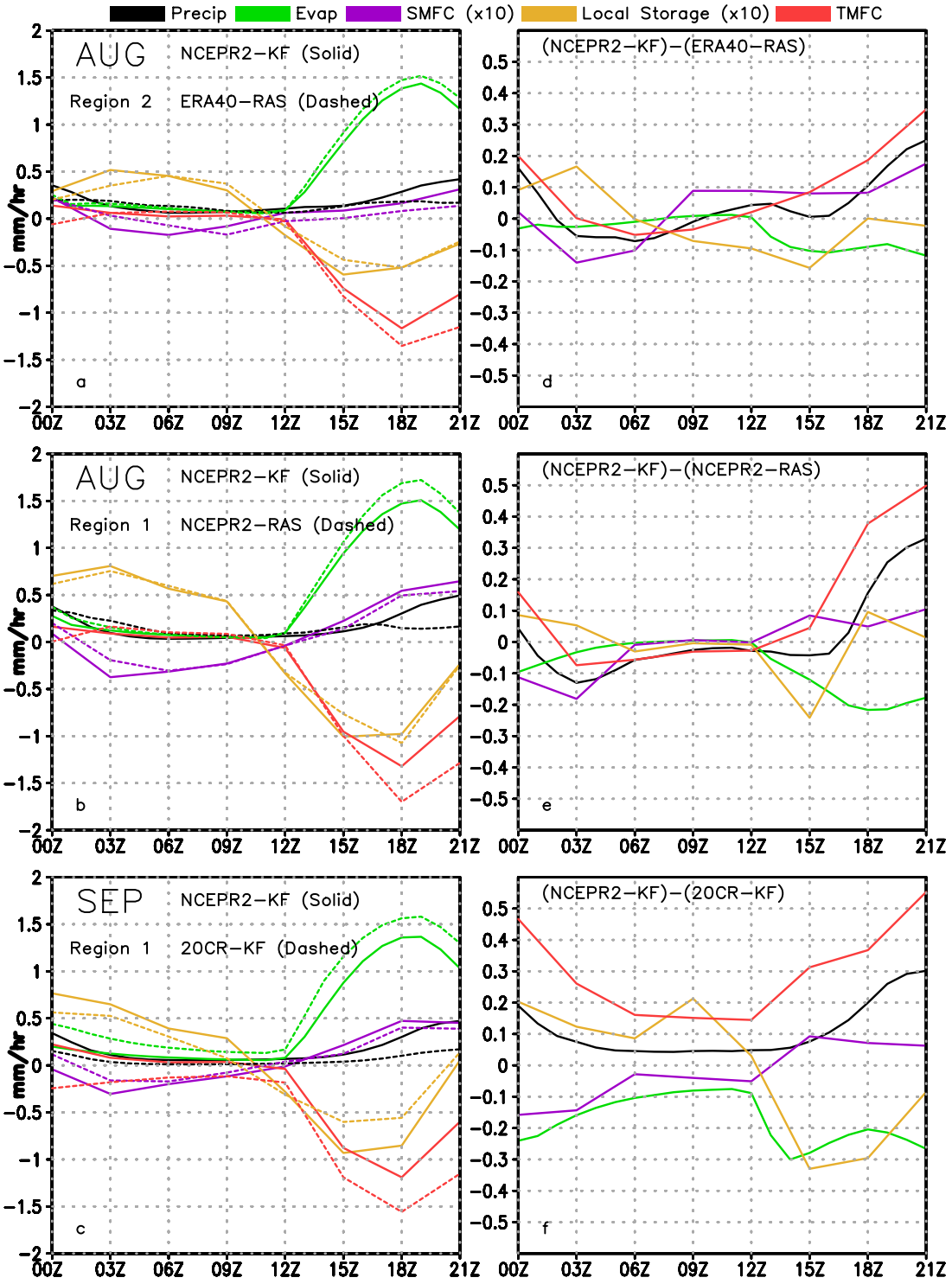

Fig. 13 - All terms of the moisture budget for a) August in Region 4, b) August in Region 1, and c) September in Region 1. Vertically integrated and time dependent terms are plotted at three-hourly intervals. For convenience of comparing the terms in the budget the stationary vertically integrated moisture convergence (SMFC) and the storage terms are scaled by 10. The transient flux term (TMFC) is computed as a residual of all terms of the moisture budget.

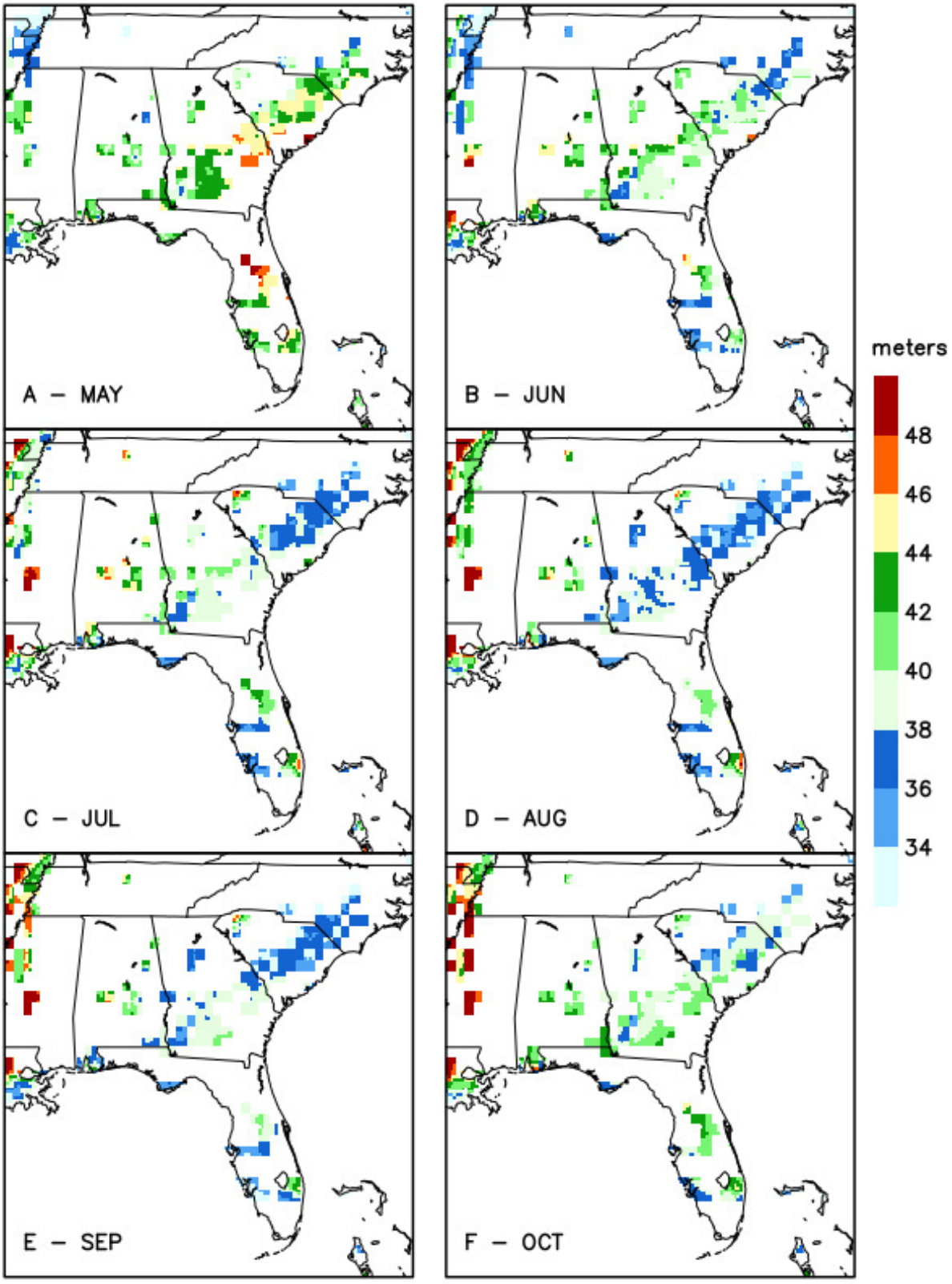

Fig. 14 - Monthly average total water added to the soil column.

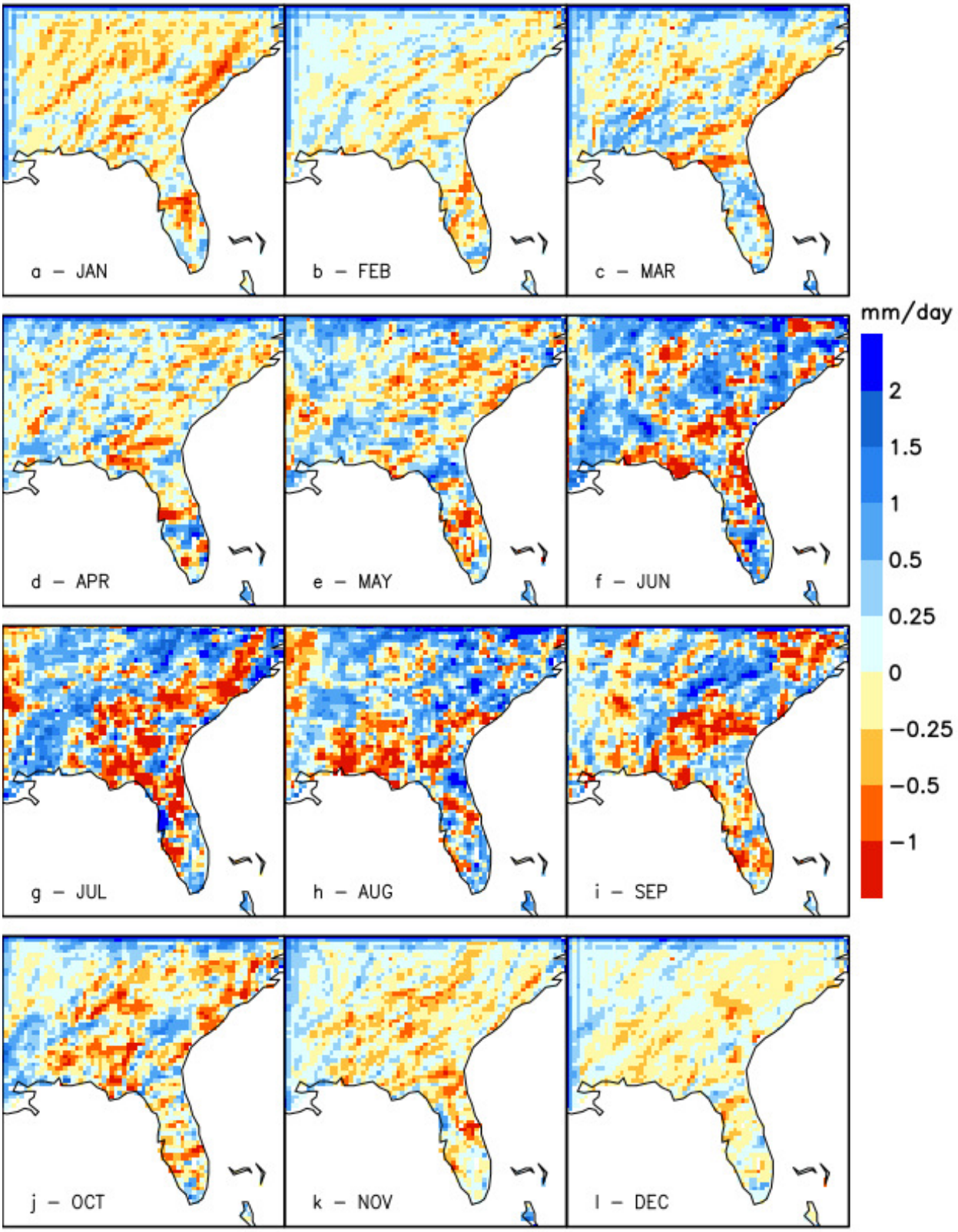

Fig. 15 - Monthly average precipitation differences (IRR100-CTL)

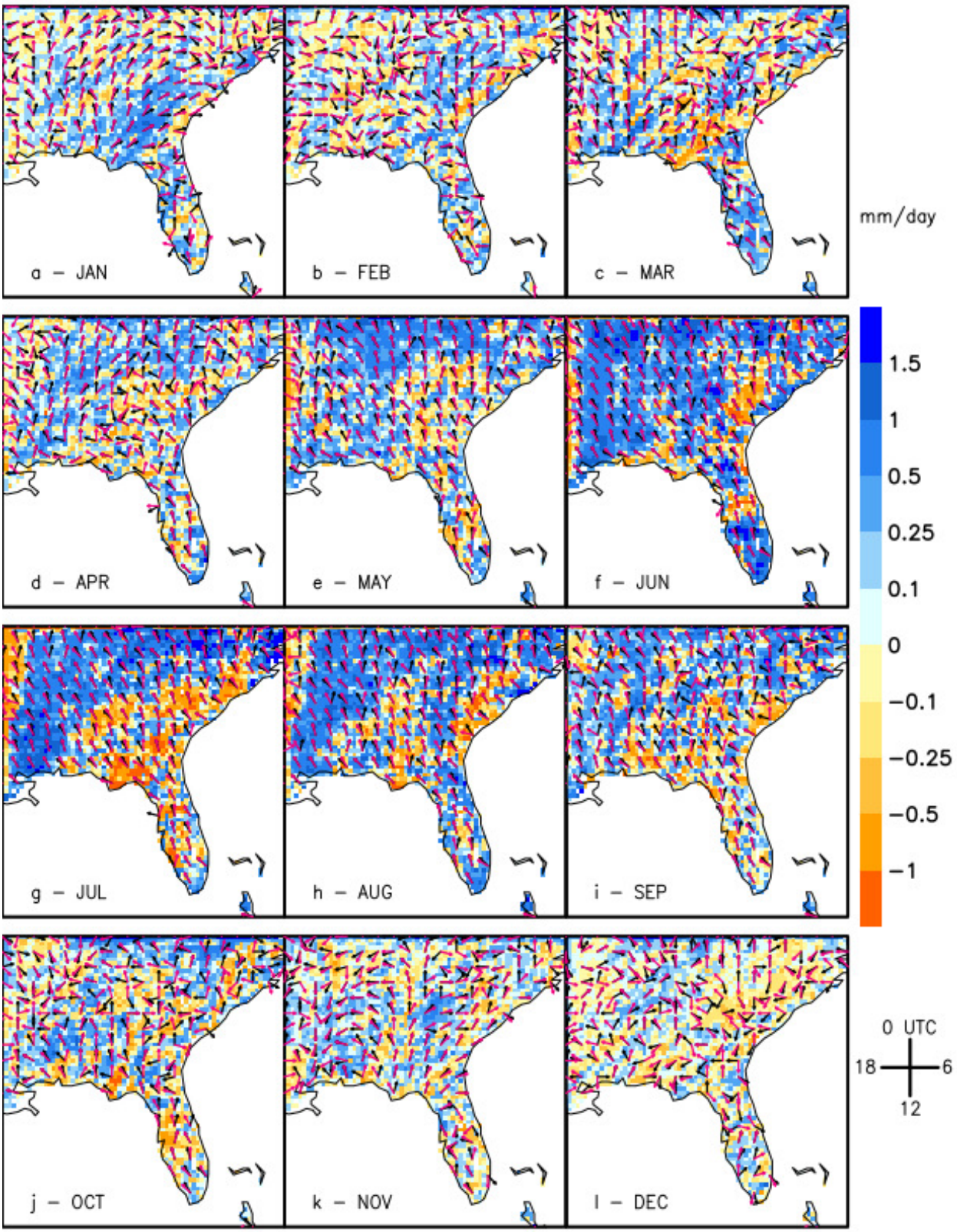

Fig. 16 - Diurnal precipitation amplitude differences (IRR100-CTL) Overlaid vectors indicate the time of maximum rainfall in the IRR100 simulation (red) and CTL simulation (black). When only one vector is visible, IRR100 and CTL timing are coincident.

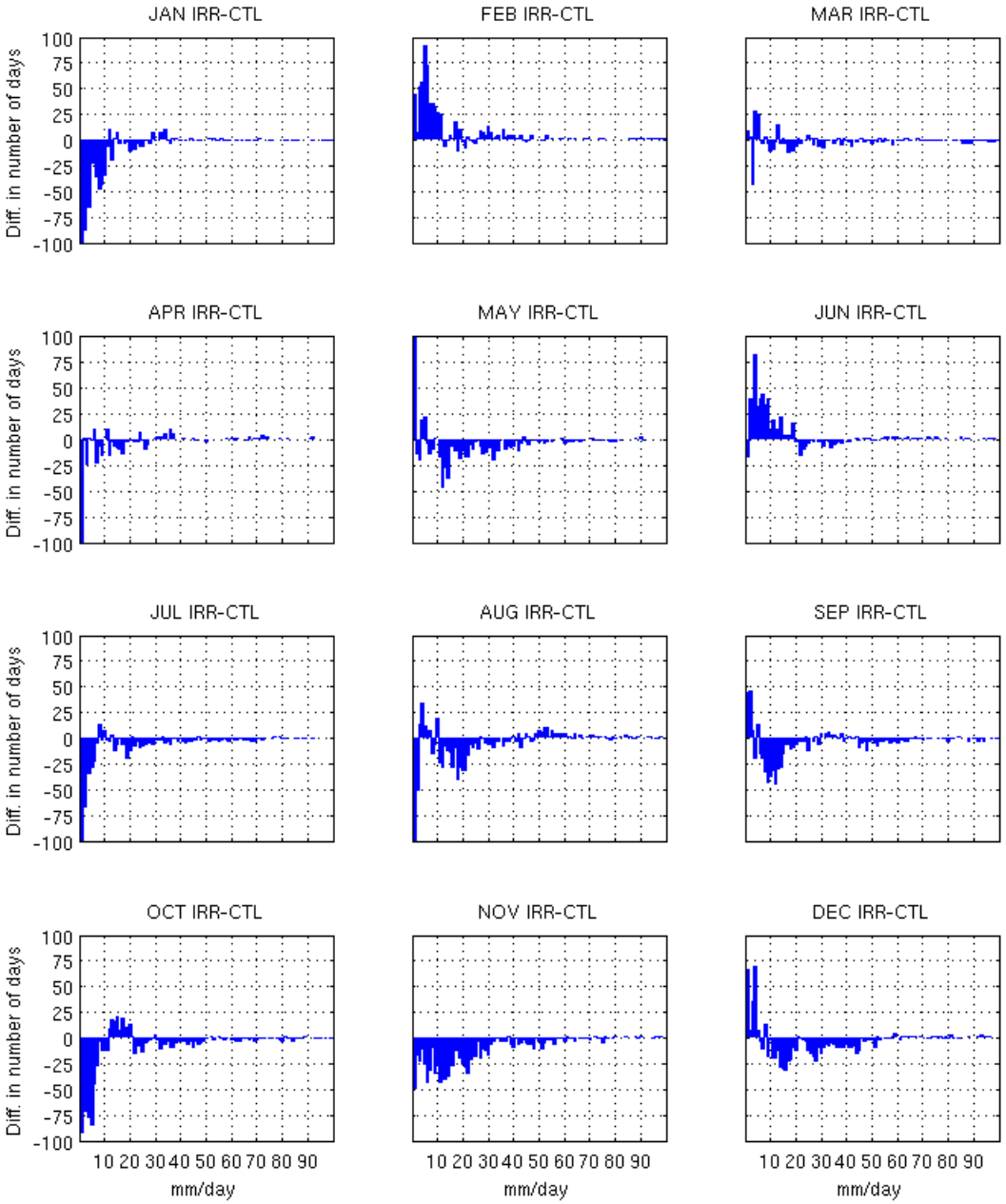

Fig. 17 - Binned difference (IRR100-CTL) in daily precipitation events. Bins are separated in 1 mm/day intervals.

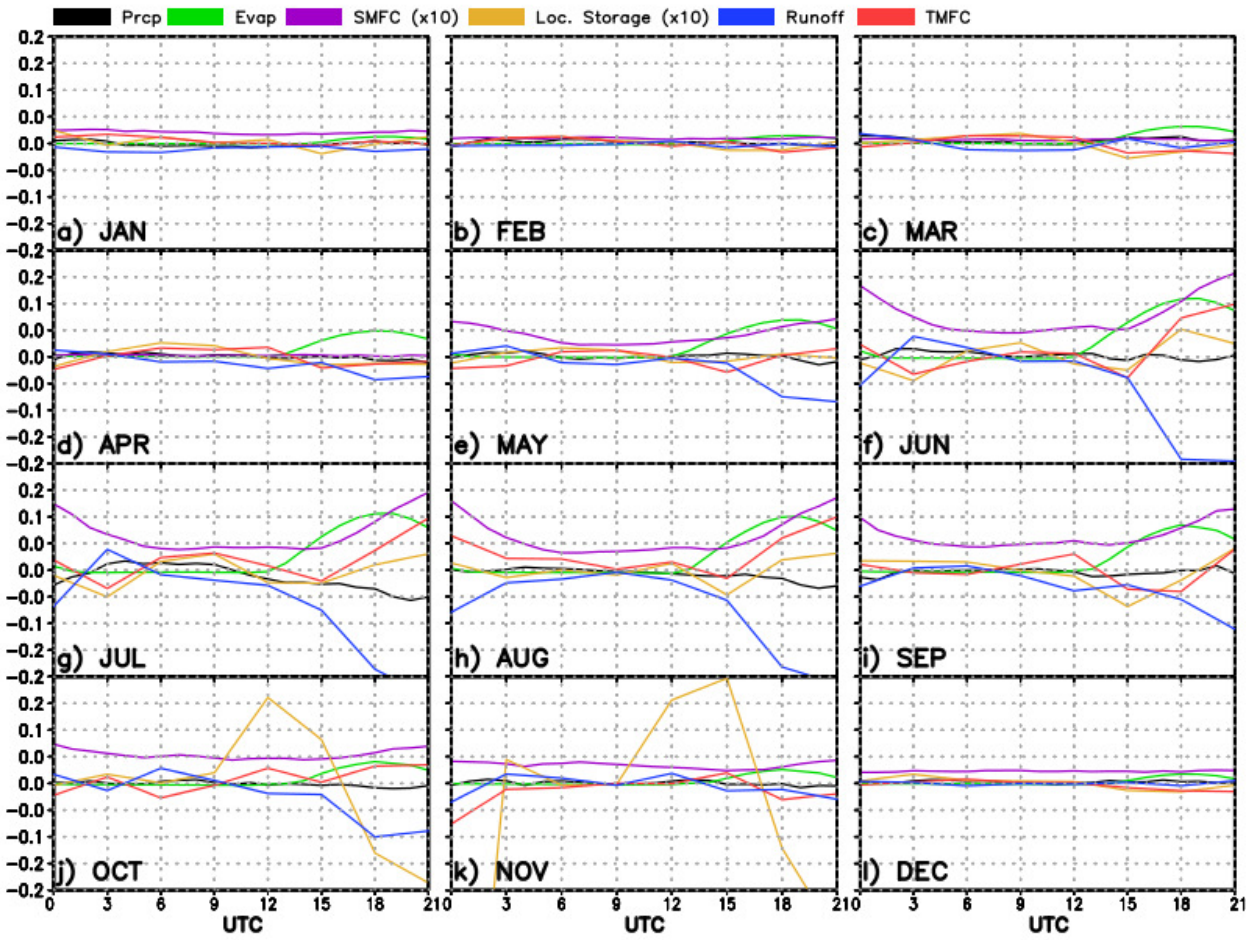

Fig. 18 - All terms of the moisture budget for IRR100-CTL. For convenience of comparison, both the stationary moisture convergence (SMFC) and local storage are scaled by 10. The transient moisture flux convergence (TMFC) is computed as a residual of all terms.

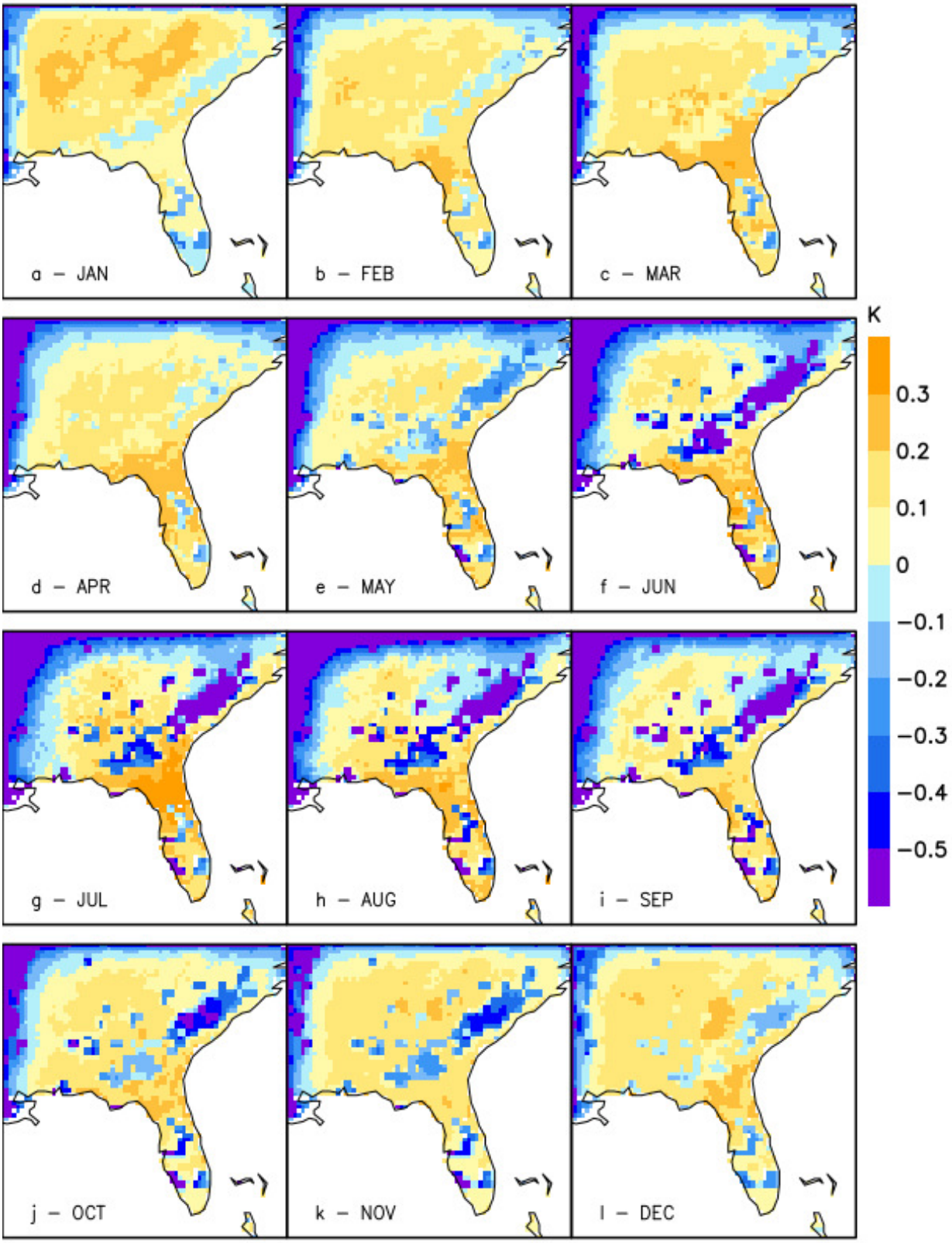

Fig. 19 - As in Fig. 15, but for temperature

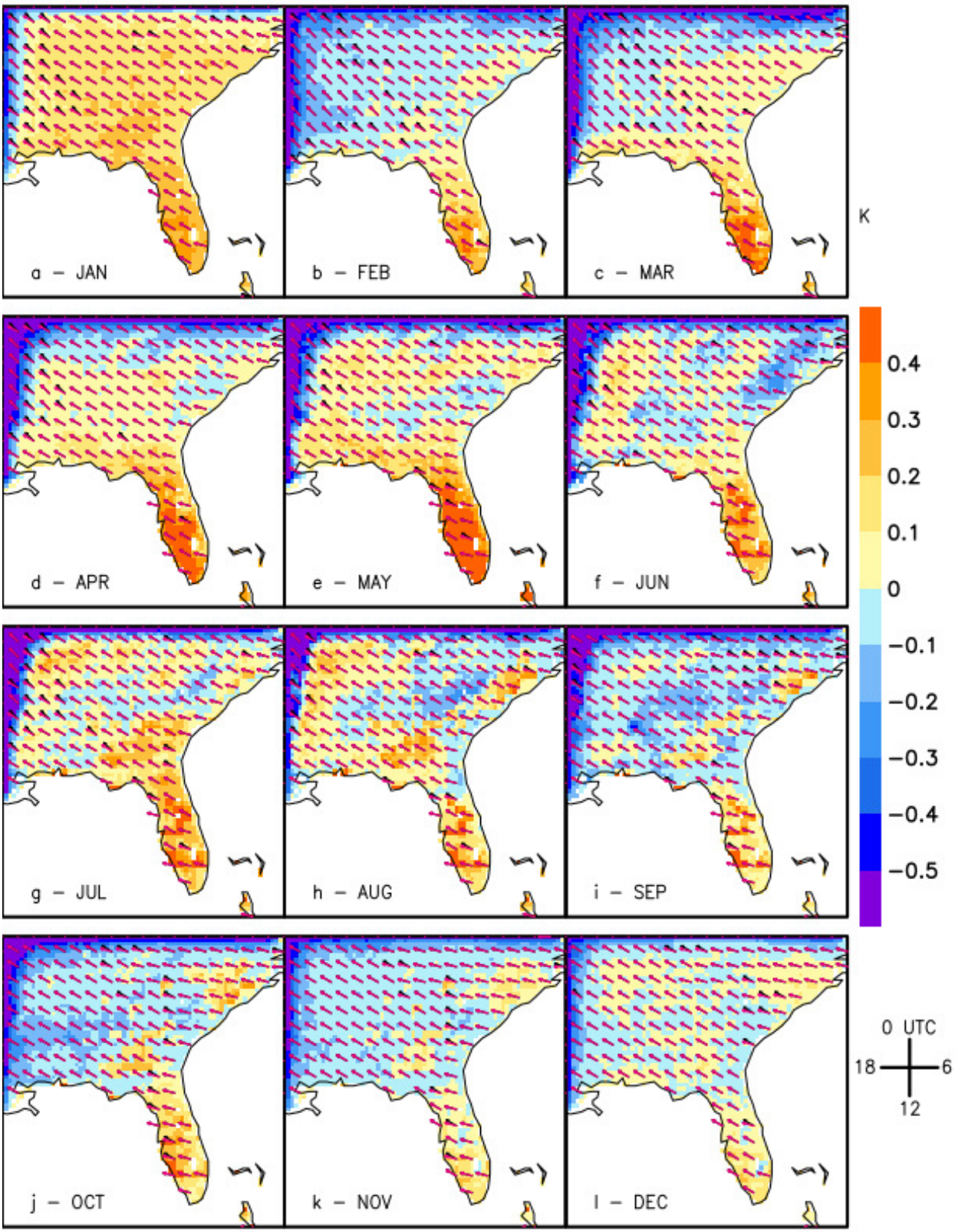

Fig. 20 - As in Fig. 16, but for diurnal maximum temperatures.

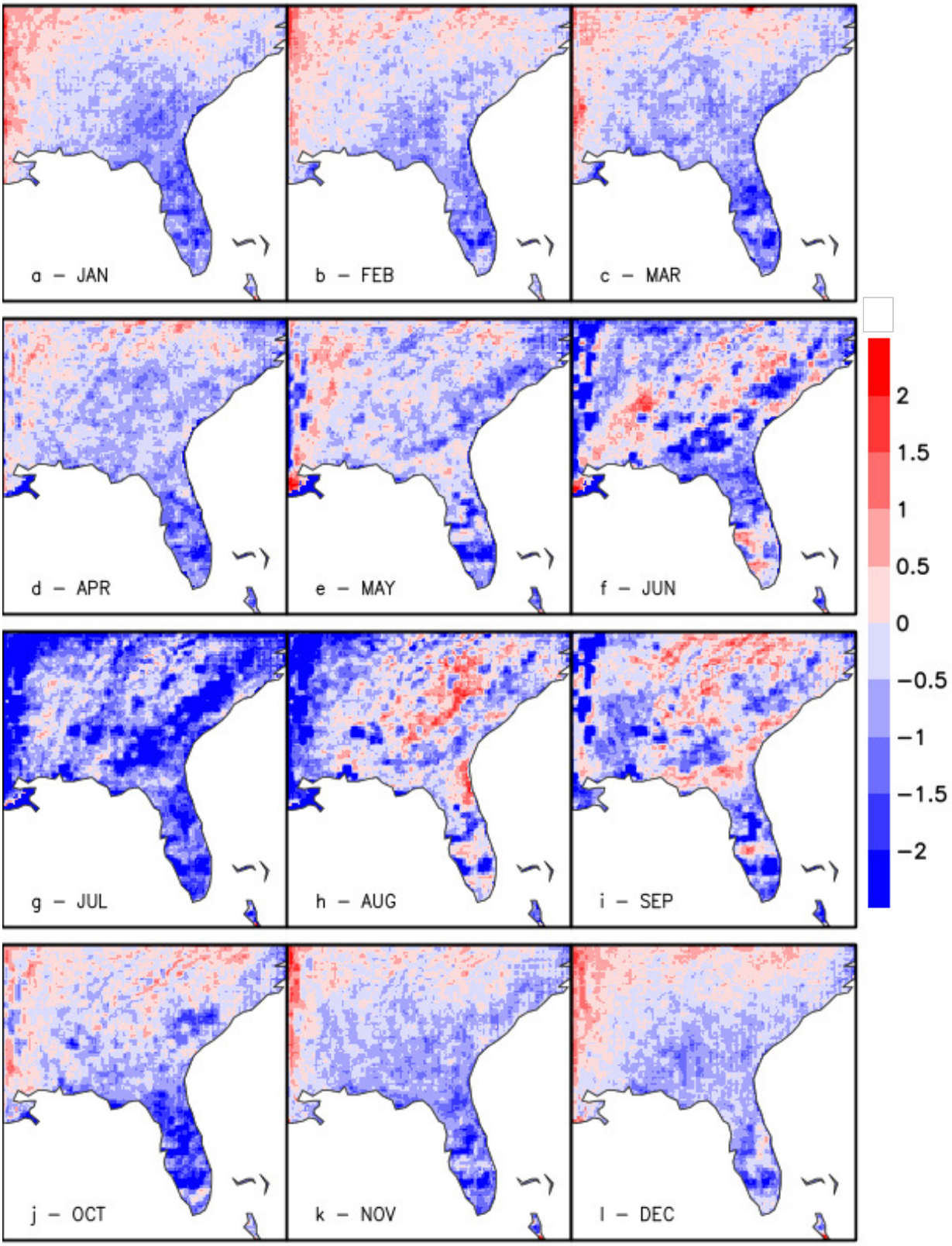

Fig. 21 - Difference (IRR100-CTL) in low cloud coverage, expressed as a percent of total sky coverage.

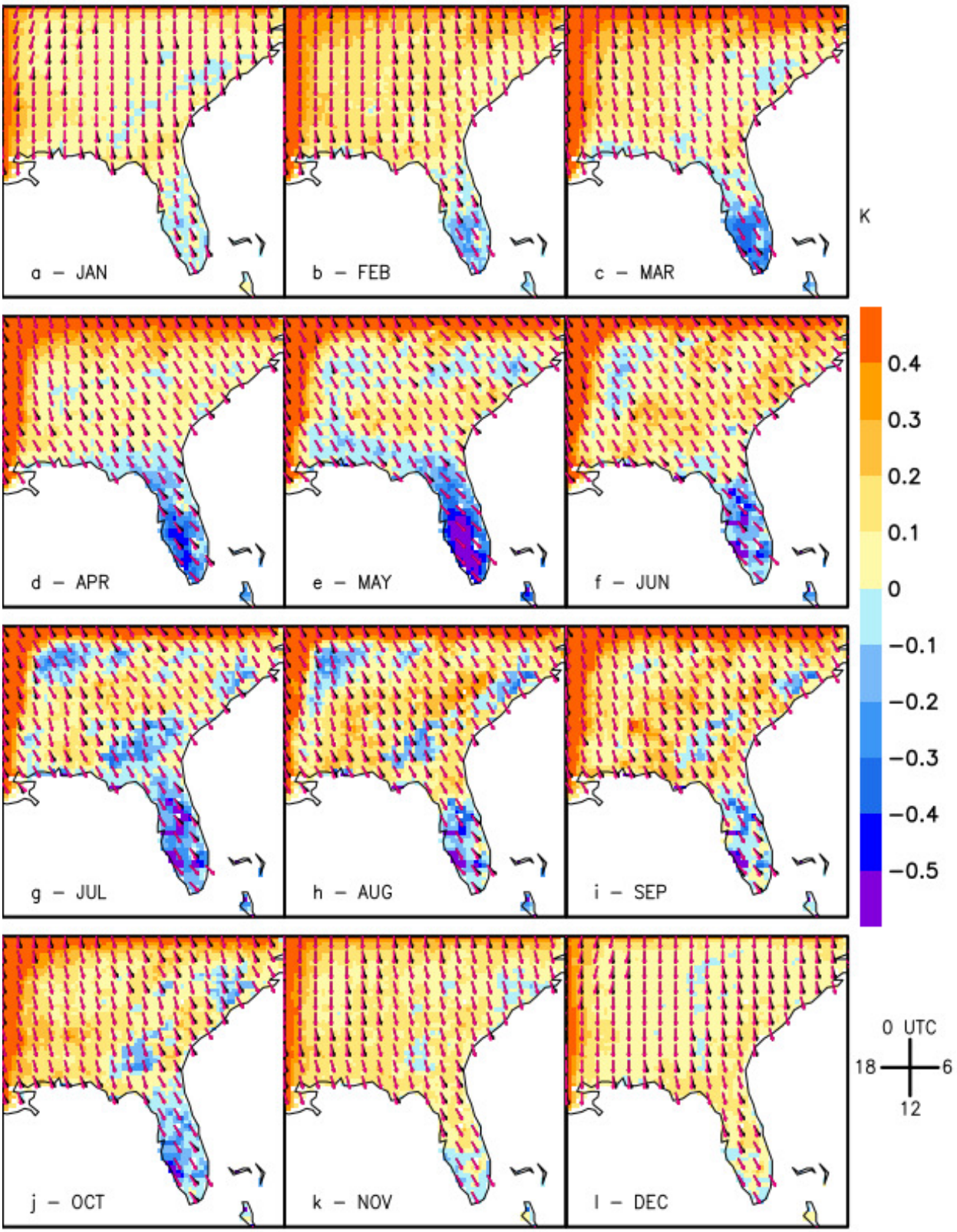

Fig. 22 - As in Fig. 20, but for diurnal minimum temperatures.

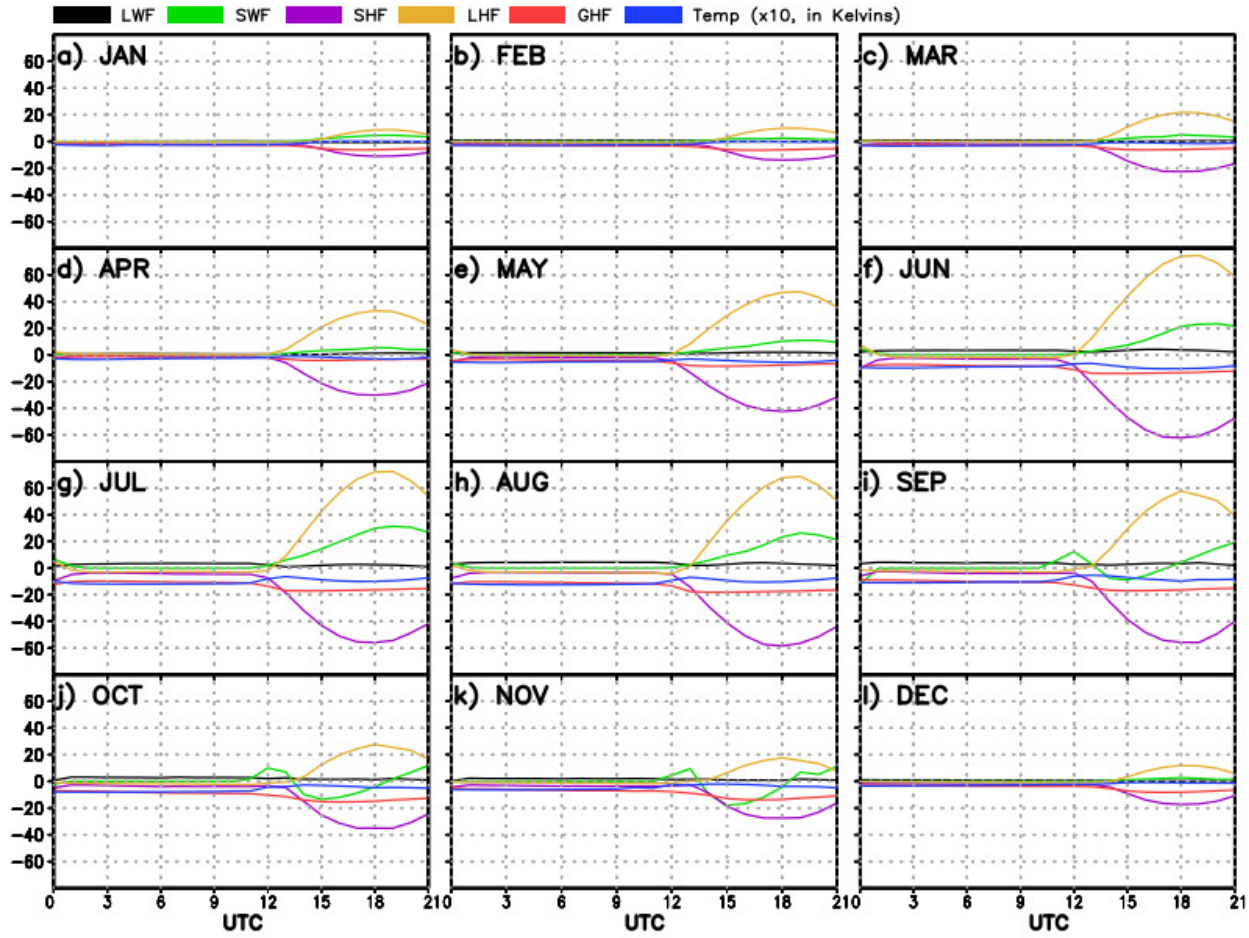

Fig. 23 - All terms of the heat budget for IRR100-CTL in W/m^2. Signs of each term follow meteorological convention. Temperature difference is included, but is scaled by ten for visibility.

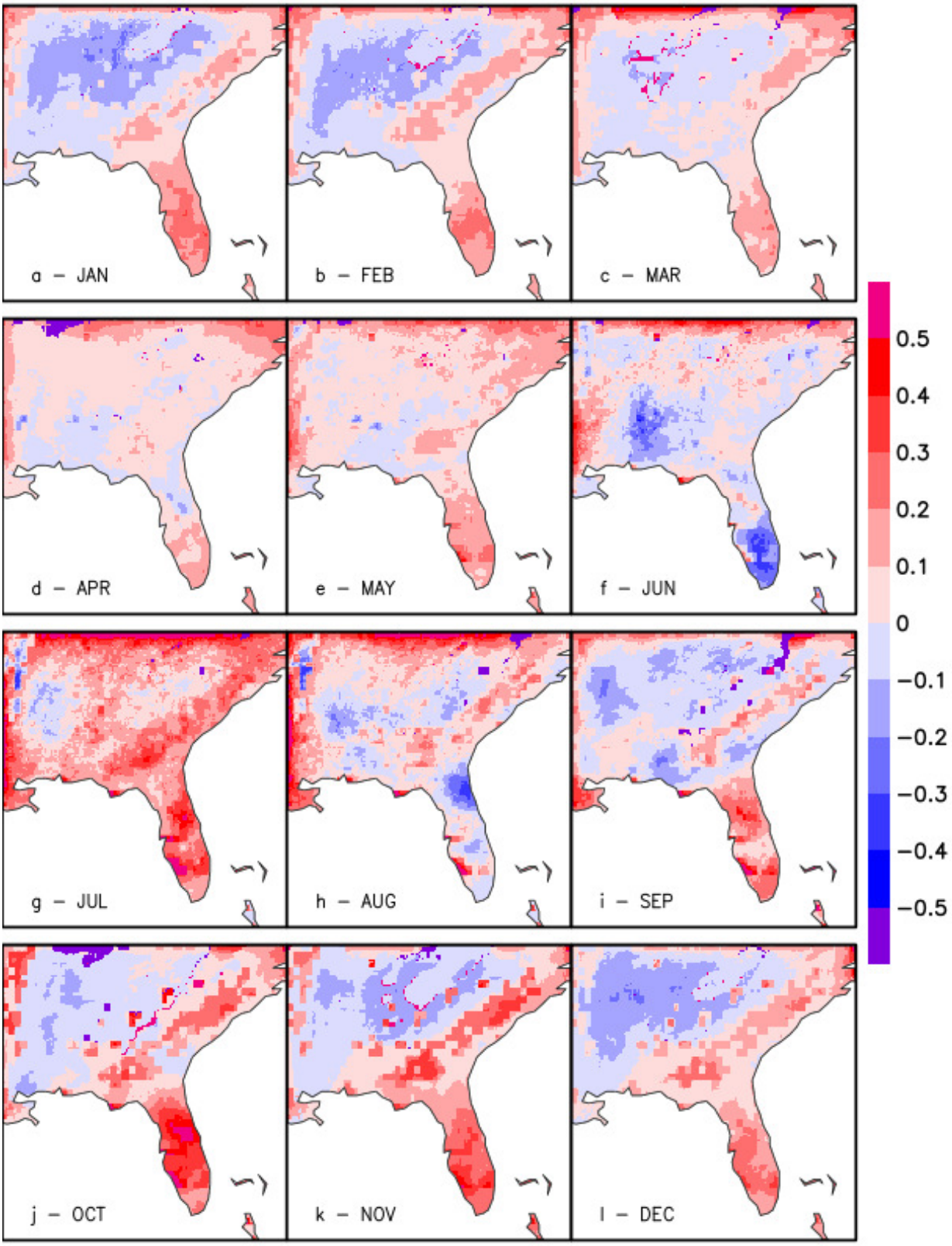

Fig. 24 - As in Fig. 19, but for the lifted index. Positive values indicate an atmosphere tending more toward stability.

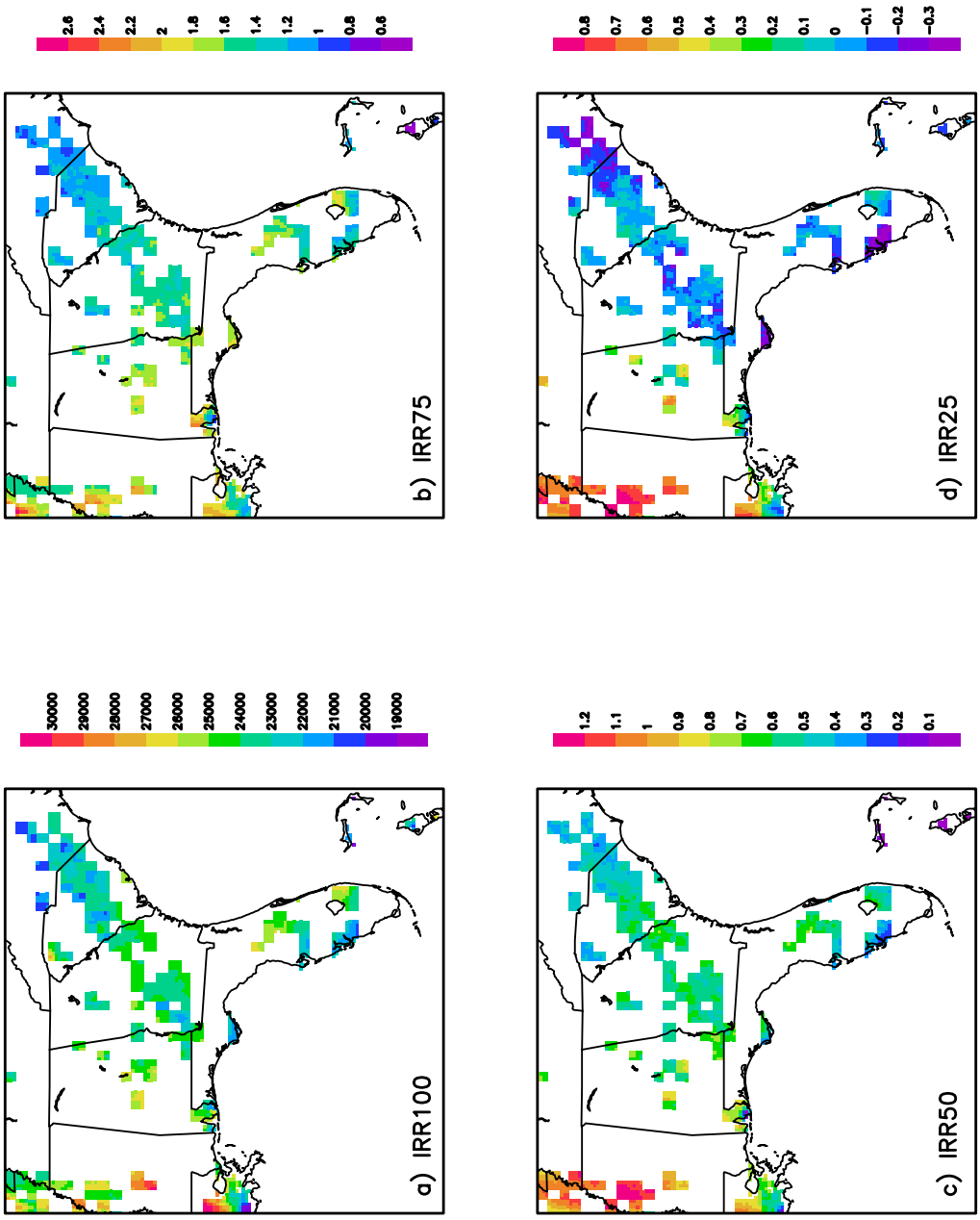

Fig. 25 - Depth of water added to each cell in order to reach a) 100% of field capacity, b) 75% of field capacity, c) 50% of field capacity, and d) 25% of field capacity. Units are expressed in cm.

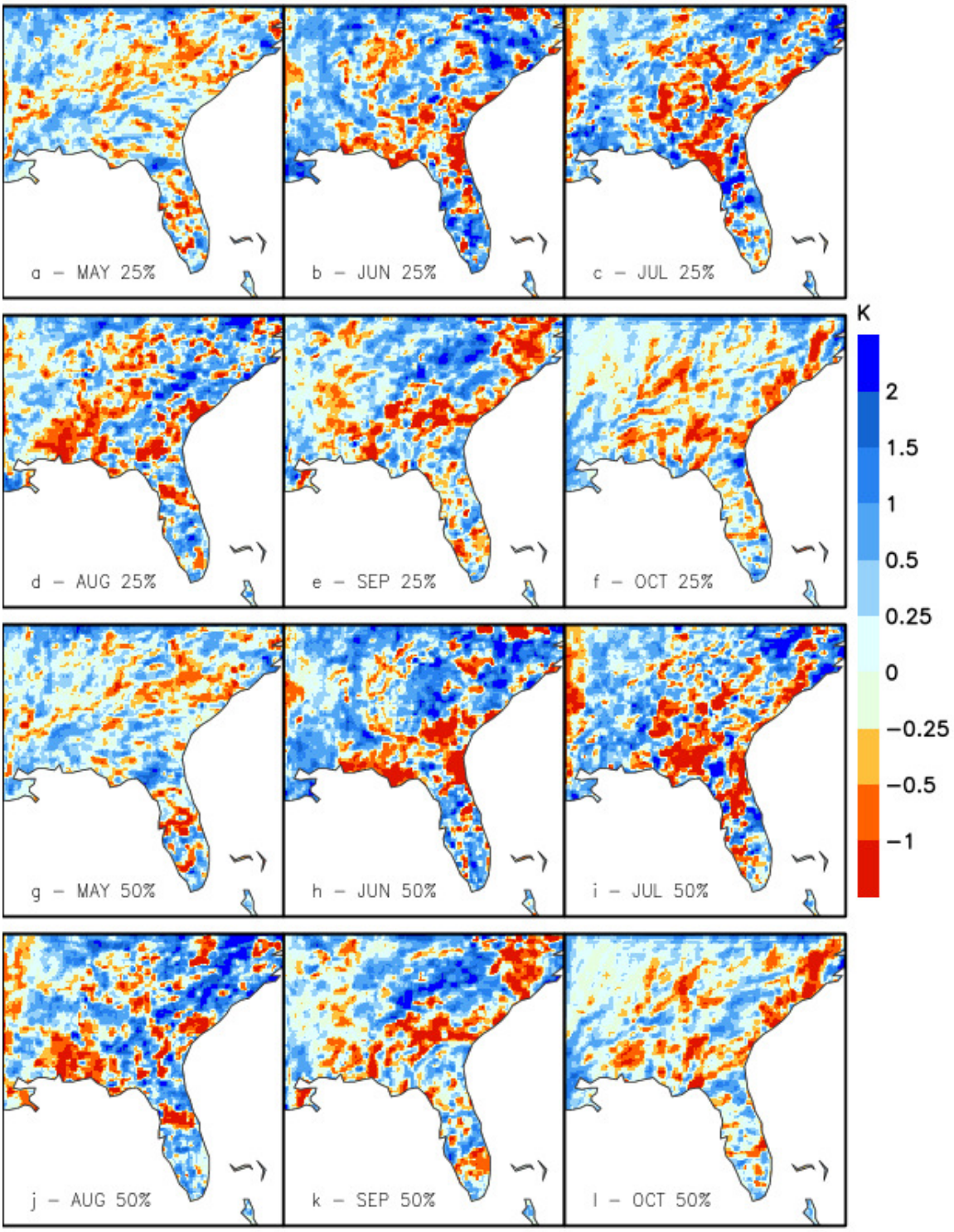

Fig. 26 - Change in monthly average precipitation, from irrigation (IRR) maintaining field root zone soil moisture at (a-f) 25% of field capacity (g-l) 50% of field capacity. Differences are computed as IRR - Control.

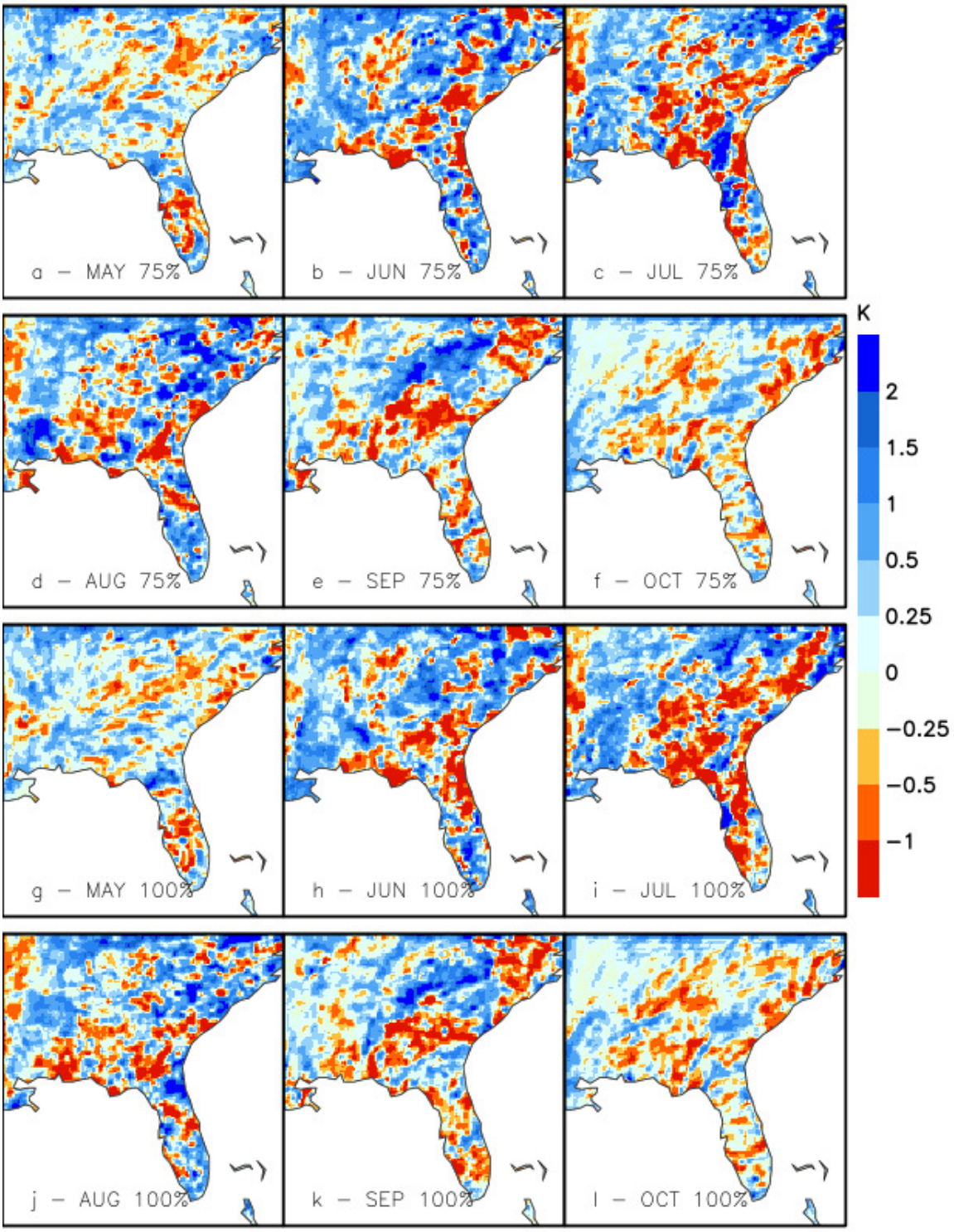

Fig. 27 - Same as Fig.26 but for IRR at (a-f) 75% and (g-l) 100%.

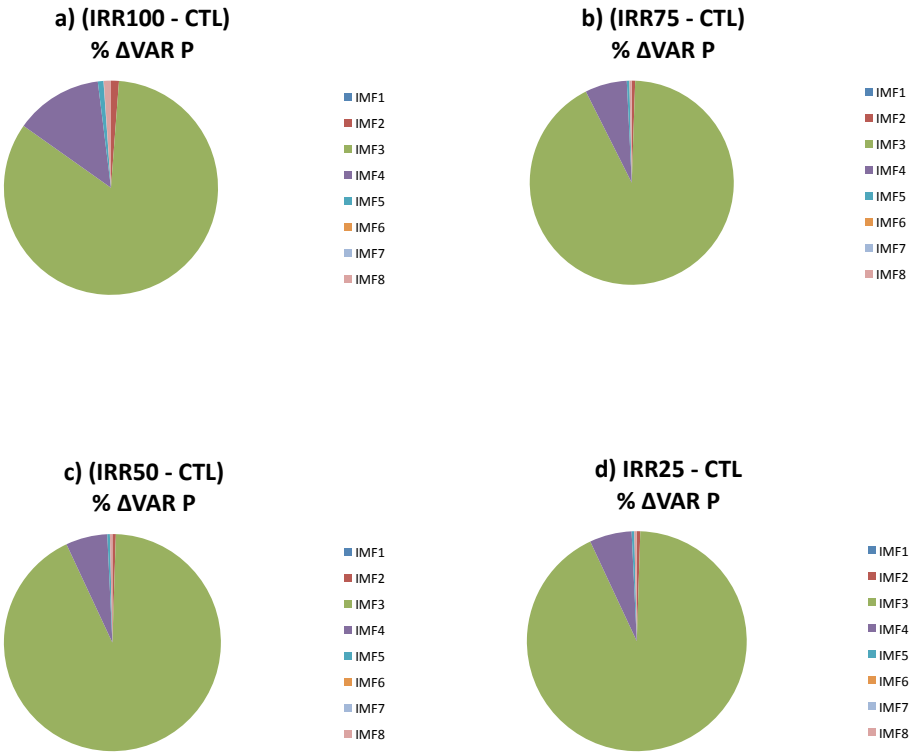

Fig. 28- Percent change in variance (IRR-CTL) of irrigation area-averaged precipitation.

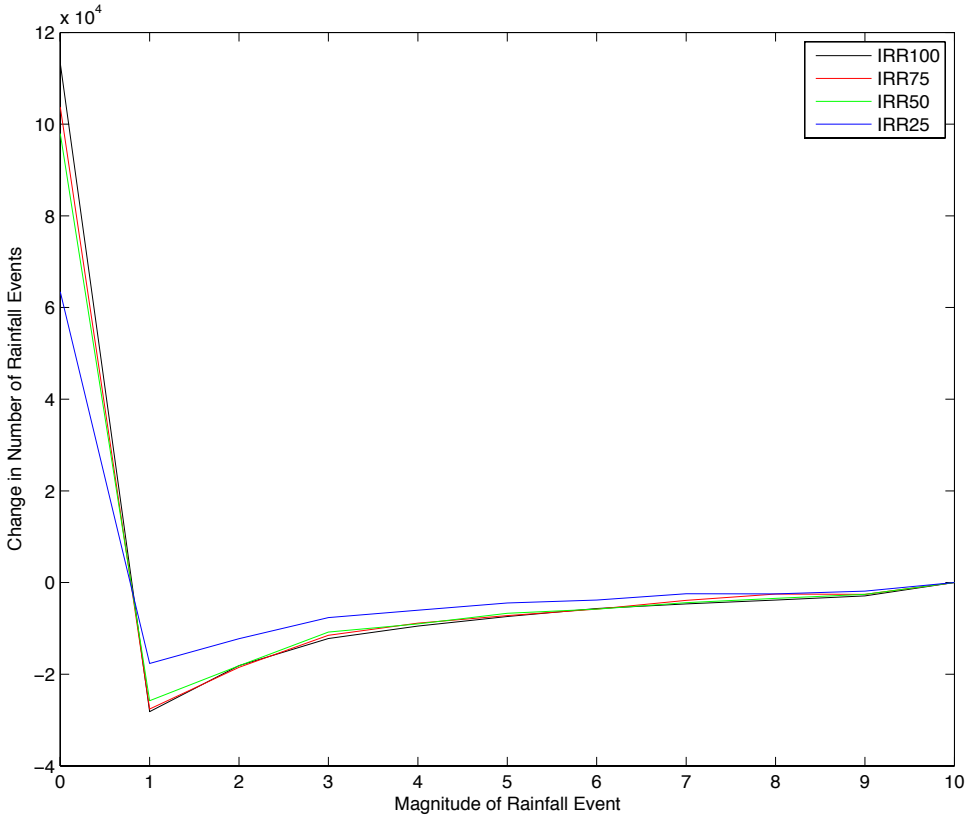

Fig. 29 - Difference (IRR-CTL) in total number of rainfall events binned in 1 mm/day intervals. Units of the ordinate axis are in days.

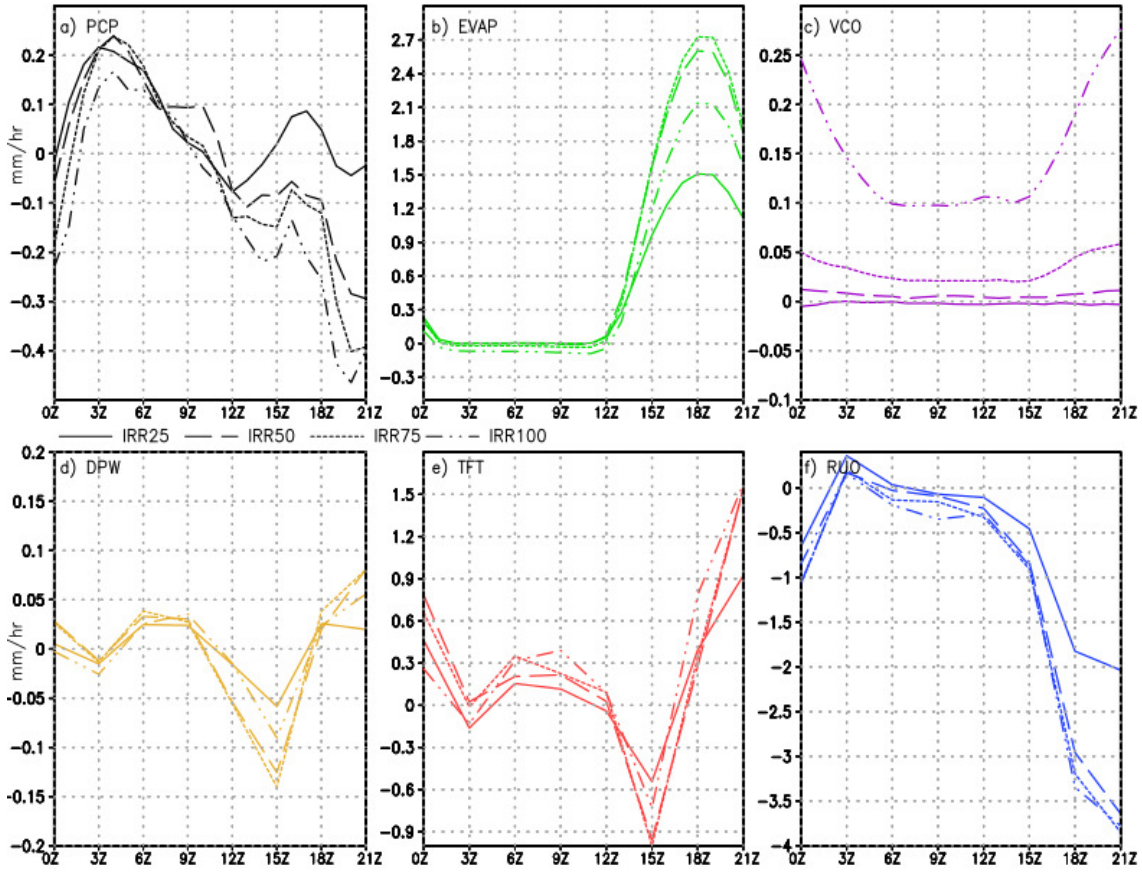

Fig. 30 - Difference of irrigation area-averaged terms of the moisture budget from CTL. Units are in mm/day. Panels represent a) precipitation (PCP), b) evaporation (EVAP), c) vertically integrated stationary moisture flux convergence (VCO), d) change in column precipitable water (DPW), e) transient moisture flux convergence (TFT), and f) runoff (RUO). Transient moisture flux convergence is computed as a residual. Units are in mm/hr.

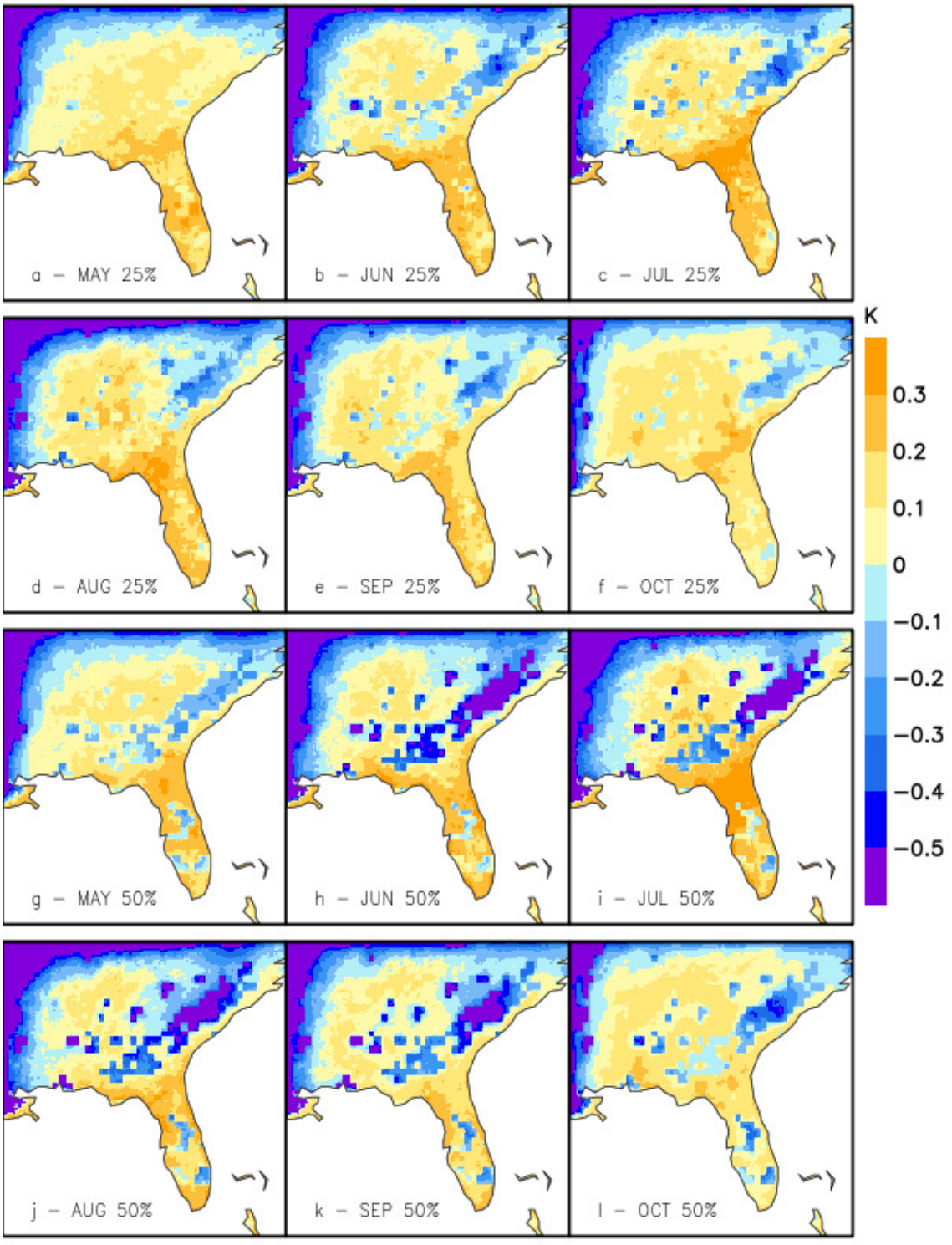

Fig. 31 - Change in monthly average surface temperature, from irrigation (IRR) maintaining field root zone soil moisture at (a-f) 25% of field capacity (g-l) 50% of field capacity. Differences are computed as IRR - Control

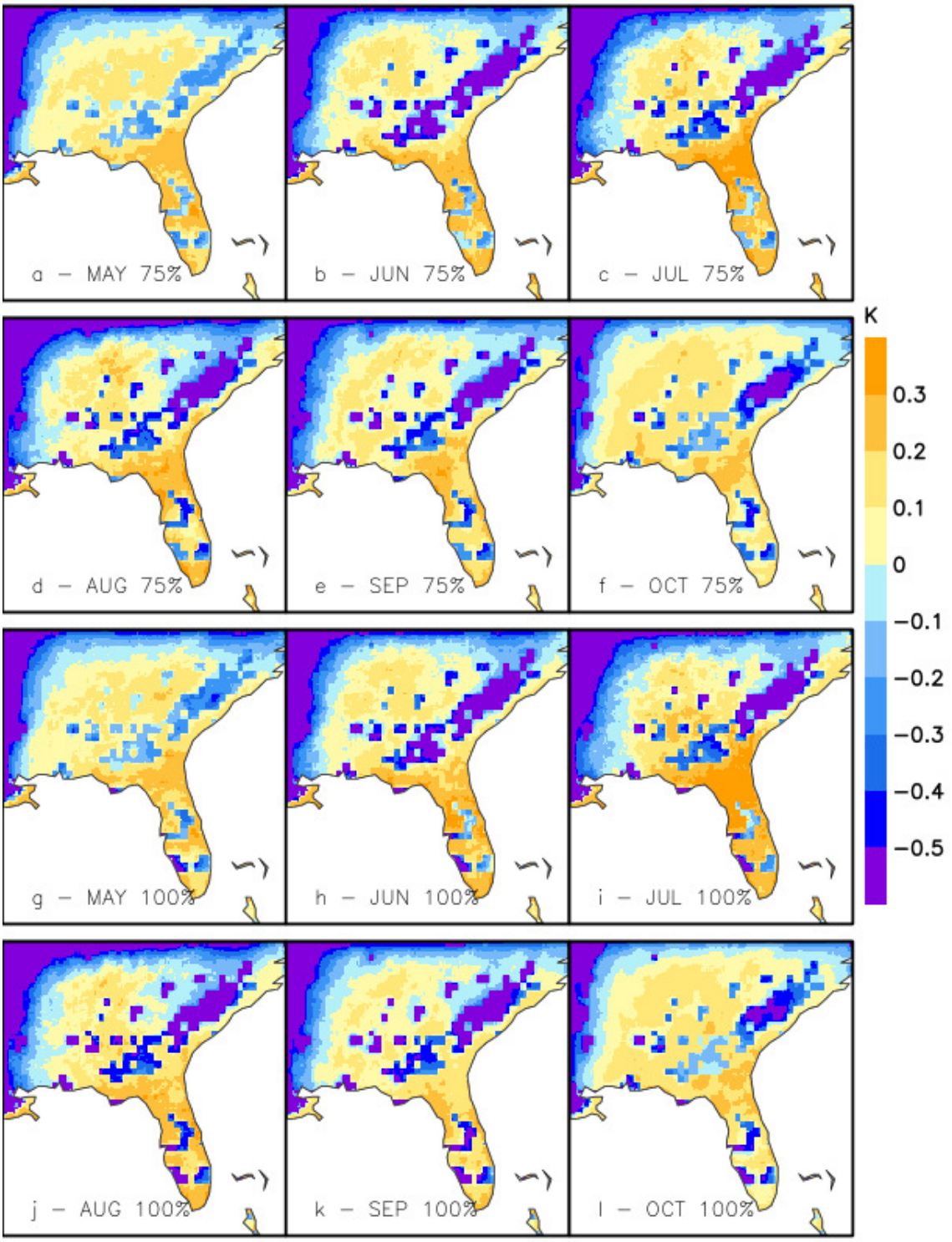

Fig. 32 - Same as Fig.31 but for IRR at (a-f) 75% and (g-l) 100%.

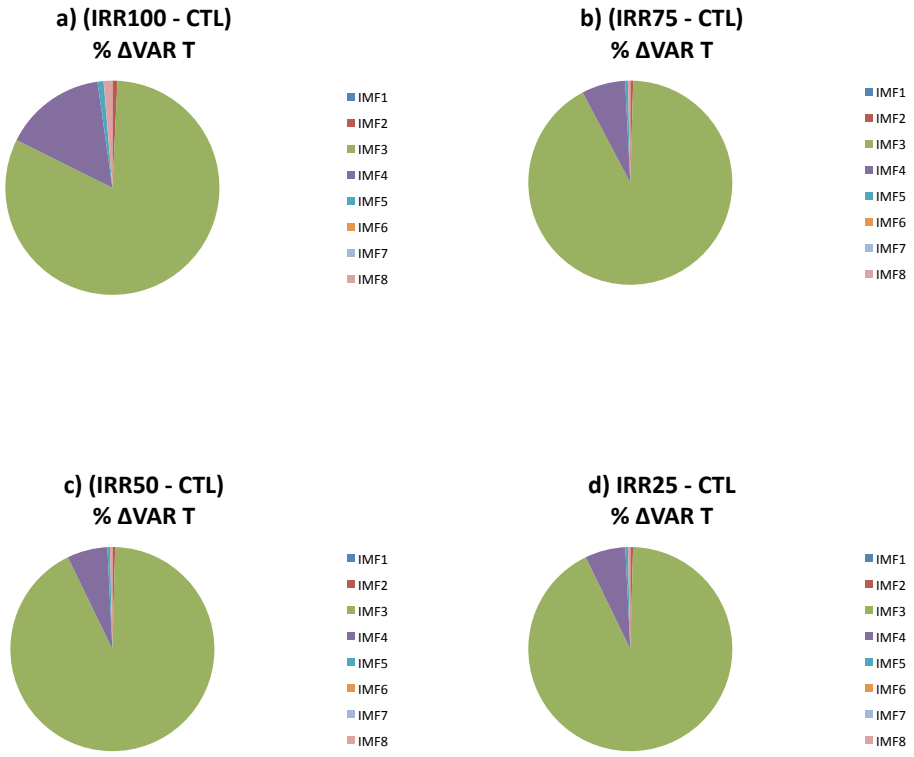

Fig. 33 - Percent change in variance (IRR-CTL) of irrigation area-averaged surface temperature.

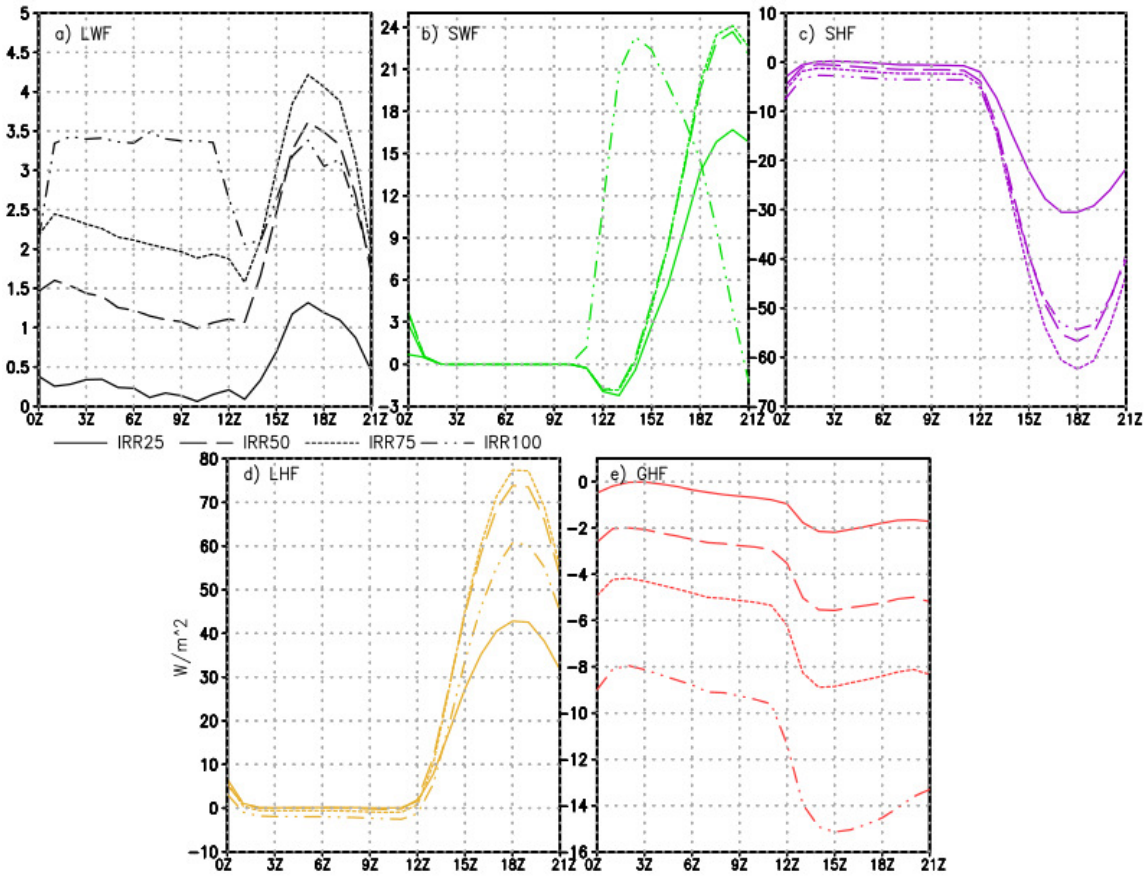

Fig. 34 - Difference of irrigation area-averaged terms of the heat budget from CTL. Units are in mm/day. Terms are represented as a) net longwave flux (LWF), b) net shortwave flux (SWF), c) sensible heat flux (SHF), d) latent heat flux (LHF) and e) ground heat flux (GHF). The sign of each flux follows meteorological conventions. Units are in W/m^2.

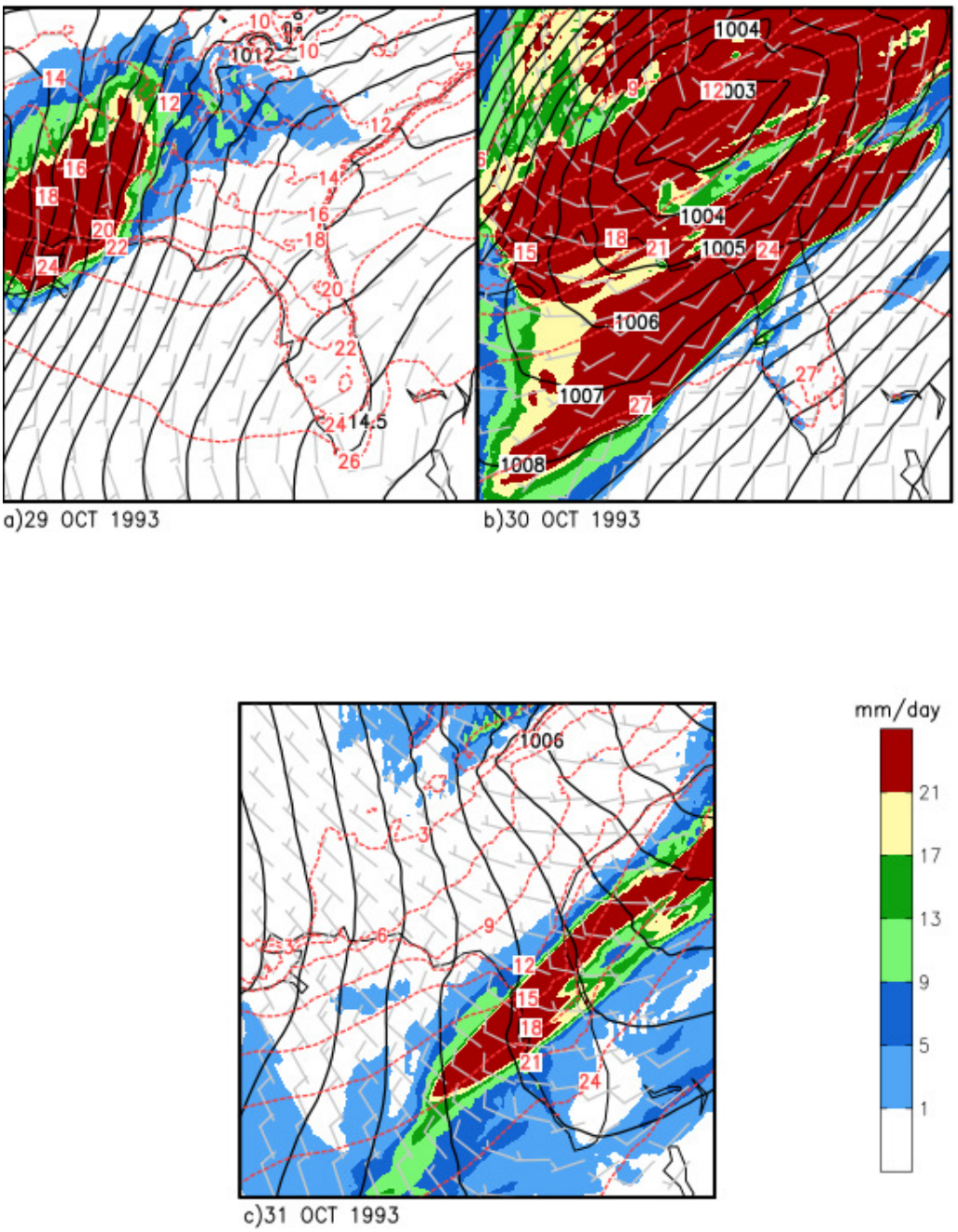

Fig. 35 - Conditions a) prior to, b) during and c) after a typical late October frontal passage over the SEUS. Underlaid wind barbs are in KTs, dashed and red contours indicate isotherms, solid lines indicate mean sea level pressure, and shading indicates precipitation intensity.

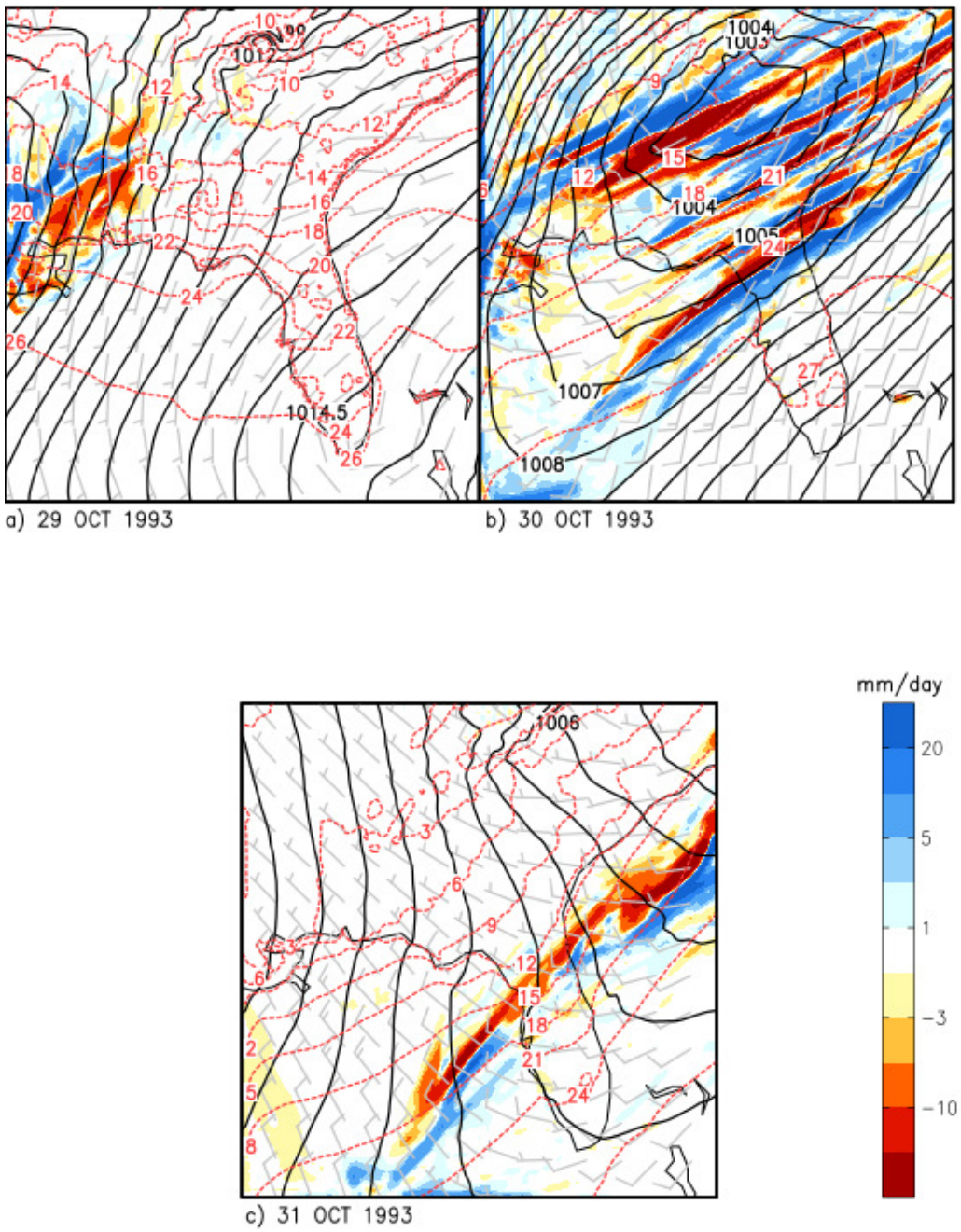

Fig. 36 - As in Fig. 35, but precipitation is plotted as a difference in IRR100 rainfall relative to CTL.

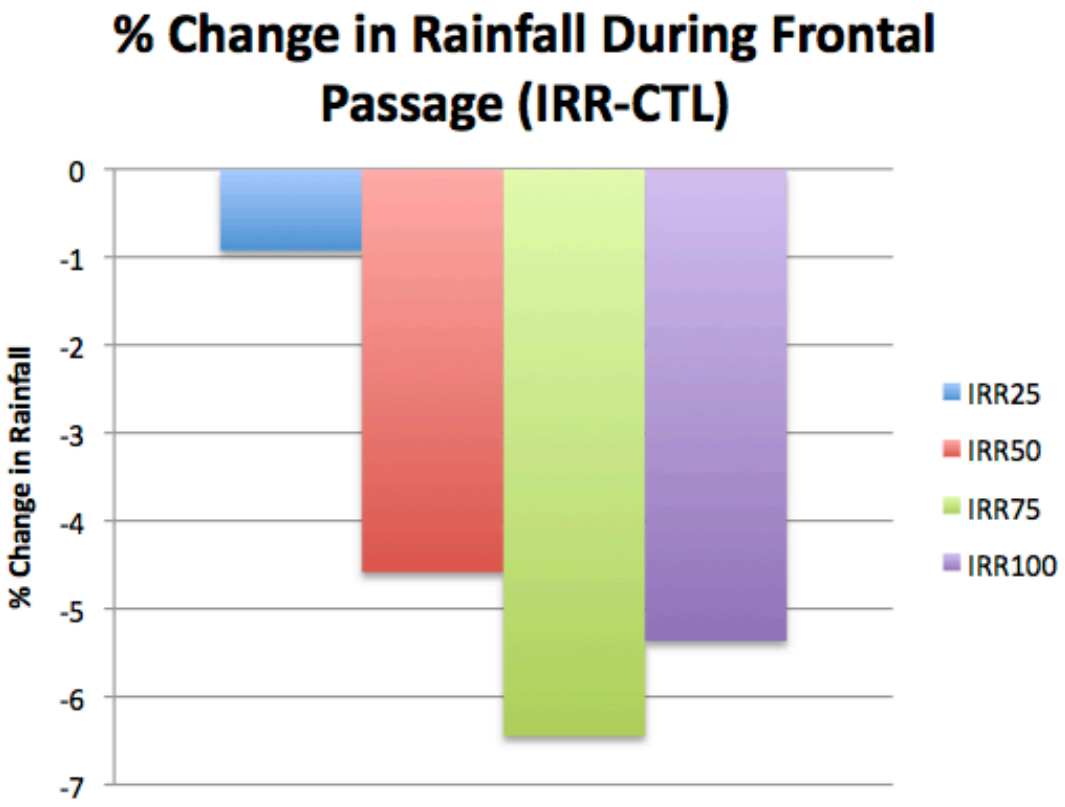

Fig. 37 - The percent change in rainfall accumulation averaged over all cultivated cells averaged across all frontal passage events.

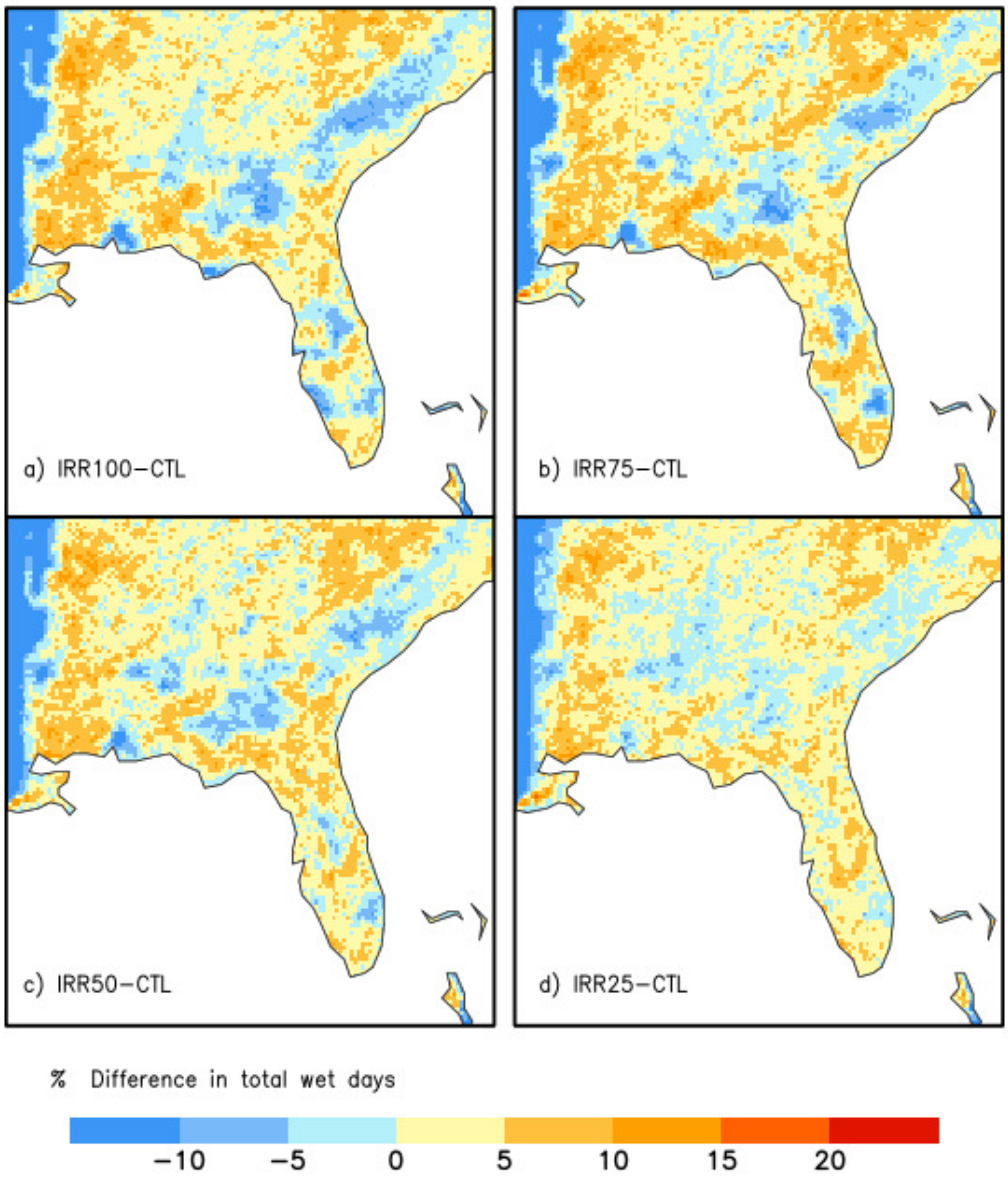

Fig. 38 - Percent reduction (IRR-CTL) in total number of wet days. Wet days are defined as days whose accumulated rainfall over a day total exceeds 1 mm.

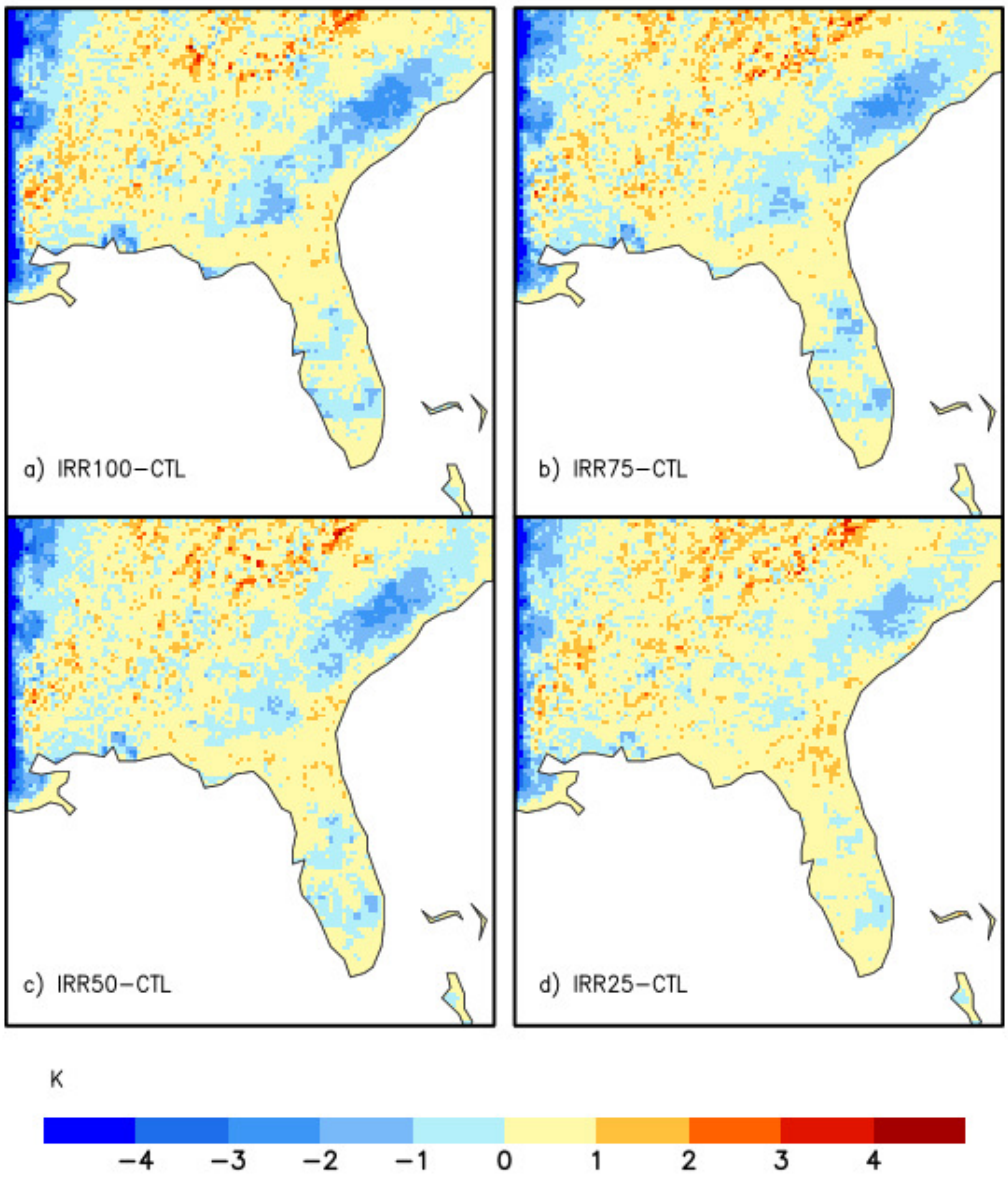

Fig. 39 - Difference (IRR-CTL) in threshold temperatures used in determining heat wave days. Thresholds are computed as the top 97.5th percentiles of all seasonal temperatures.

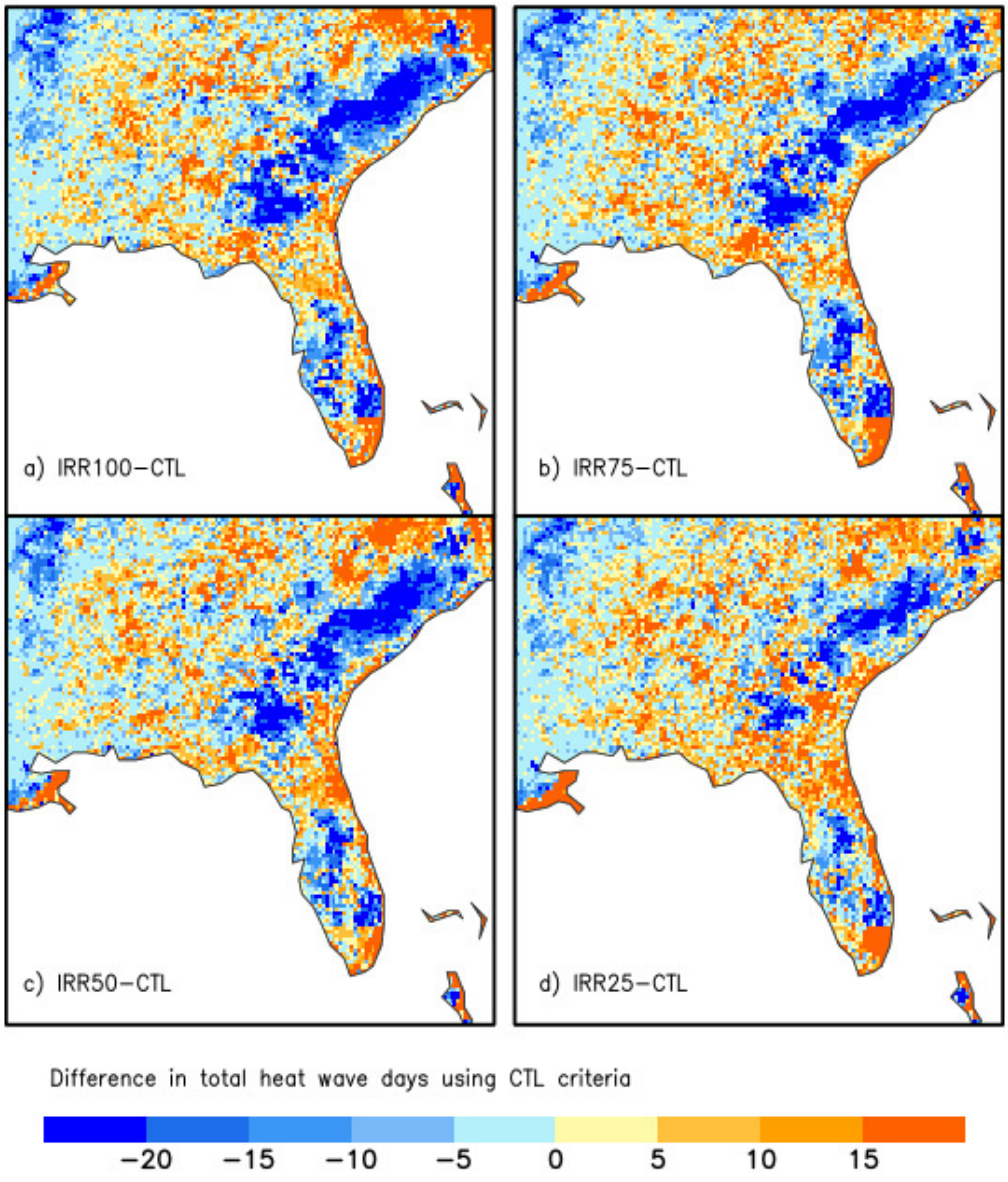

Fig. 40 - Difference (IRR-CTL) in total number of heat wave days using CTL threshold criteria.

CHAPTER 4

SUMMARY AND CONCLUSIONS

The fidelity and sensitivity of regional climate model simulations of diurnal variability of precipitation and surface temperature to changing lateral boundary forcing prescribed from different global reanalysis and convection schemes was examined in this study. In total we conducted 6 independent integrations forced with NCEPR2, ERA40, and 20CR global reanalysis and with two different convection schemes viz., Kain-Fritsch (Kain and Fritsch 1993) and Relaxed Arakawa Schubert scheme (Moorthi and Suarez 1992). We regarded NCEPR2-KF as our baseline integration for convenience.

The fidelity of the diurnal and seasonal climate variations in precipitation in these regional climate model simulations reveal that configuration forced with 20CR global reanalysis (20CR-KF and 20CR-RAS) show the largest RMSE. The RMSE of the annual cycle of precipitation and surface temperature of the other four simulations (not forced by 20CR) were however, comparable to each other and was highest in the summer months. But the RMSE of the diurnal amplitude of precipitation and the timing of its diurnal zenith were largest during winter months and least during summer and fall months in the four model simulations (not forced by 20CR). The diurnal amplitude of surface temperature in comparison showed far less fidelity in all model simulations especially outside of the Florida Panhandle within the SEUS domain. This low fidelity can possibly be attributed to relatively coarse resolution and hence topography of NLDAS-1, biases in diurnal precipitation in the NLDAS-1 suite, and our model's lack of consideration for land use change in the SEUS. In addition the bias related to cloud cover in the RSM cannot be ignored. Li and Misra (2014) find that RSM has a tendency to overestimate the low cloud fraction The phase of the diurnal maximum of surface temperature shows significantly much higher fidelity in all of the 6 model simulations.

We objectively defined sensitivity as a fraction of the difference between the baseline regional climate model integration (NCEPR2-KF) and each of the other five experiments divided by the difference between the baseline value and observed value of the variable. We found that 20CR-KF was most different from the baseline integration in the simulation of the diurnal amplitude of precipitation, especially in the summer and fall months. In contrast the sensitivity of

the phase of the diurnal maximum in precipitation is weak, especially in the winter months, to changes in the lateral boundary conditions and convection schemes. However, convection schemes seem to modulate the phase of the diurnal maximum in precipitation in the other three seasons more than the boundary conditions. On the other hand the sensitivity of diurnal amplitude of surface temperature to changes in convection scheme and lateral boundary conditions is comparatively far less. In further examining the cause of the significantly large differences in the diurnal amplitude of the precipitation in the summer months between NCEPR2-KF and 20CR-KF, we find from moisture budget analysis that transient moisture fluxes and surface evaporation exhibited the largest differences between the two simulations. In regions and months with low sensitivity, however, model simulations are in agreement with one-another with insignificant difference in transient moisture flux and surface evaporation (not shown).

In conclusion, our study finds that the regional climate model simulation of the diurnal variations of surface meteorology in the SEUS domain seems to be comparable in its fidelity when forced with NCEPR2 or ERA40 global reanalysis using either Kain-Fritsch or Relaxed Arakawa Schubert scheme. In other words, discerning the differences between the impact of NCEPR2 and ERA40 from changes in convection scheme is inconclusive. The use of 20CR as a lateral boundary condition does however show a significant difference. Further, it does not verify as well as the rest of the model simulations of this study. These results are significant, as projections of climate change can benefit substantially from incorporating considerations for finer-scale features such as the diurnal variation. While capturing variance of extreme events is significant, so too is understanding the changes to stationary patterns like the diurnal variability, which is a significant part of the seasonal variability in the SEUS (Bastola and Misra 2013). This study is suggesting that by understanding the fidelity of diurnal scale features in the current era from a forced downscaled integration, we may be able to assess the relative reliability of the GCM forcing for future projections of diurnal features in the downscaled integration. At minimum we will have an enhanced understanding of the individual regional climate model's sensitivity to choice of driving AGCM. This understanding will allow for an improved characterization of our confidence in the projections produced by each regional climate model.

Further, simulated results of an extreme irrigation case (where irrigation is set to 100% of field capacity from May through October) were compared against a non-irrigated control run

over the SEUS. Studies on this subject in other regions indicated a warming of nighttime temperatures due to increased thermal capacity of moist soil, and cooling of daytime temperatures owing to increased cloud cover. However, over the SEUS our study indicated opposite results- nighttime temperatures cooled and daytime temperatures warmed. These two changes do not explain the staunch cooling tendency seen in the monthly averaged temperatures. It was determined that the pronounced cooling manifests across all timescales. In order to understand the mechanisms behind these phenomena, surface heat and moisture budgets at hourly interval were computed. It was found that SHF and LHF compensated their respective decreases and increases, and SWF increased at the surface. During the day, the increase in SWF (as a result of less cloud cover) led to an increase in daytime temperatures, and at night an enhanced downward transport in GHF led to nighttime cooling over some irrigated regions. In other regions, the darker soil and reduction in daytime cloud cover caused warming similar to that of Kanamaru and Kanamitsu (2008). The overall decrease in temperature led to a large-scale stabilization of the atmospheric column that persisted through the year, resulting in an overall reduction in cloud cover and by extension precipitation over irrigated areas seen in both the diurnal and monthly averaged values. These changes progress into a positive feedback loop wherein increasing column stability leads to further reduction in rainfall. Because rainfall has reduced, there is a concomitant reduction in cloud cover and increase in downwelling shortwave flux. The increase in shortwave flux then leads to a warming of daytime temperatures. At night, owing to the reduced cloud cover, there is an increased loss of LWF. Alongside this, there is also an increased downward transport of GHF. The two processes combined bring a reduction in nighttime temperatures. The reduction of the cloud fraction in the IRR run is on account of a couple of reasons: a) the reduction of detrained condensed water from convection and b) increased stability of the atmosphere in the lower troposphere, which results in the reduction of the diagnosed cloud cover as it fails to meet the threshold stability criterion despite the relative humidity criterion being met. The feedback emerges here, as cooled nighttime temperatures enhance local atmospheric stability. This feedback process is summarized in Fig. 14. In addition to these results, we showed that maintenance of 100% field capacity irrigation requires an unrealistic amount of water to be maintained through the growing season; on the order of about a 200m depth of water is added. Previous studies have neglected to consider this, and it is indeed possible over drier regions like the California Central Valley that even more water is being

applied than in the SEUS. These results highlight the impact on SEUS climate from an extreme case of sub-surface irrigation.

Despite that, we have found that the mechanisms and features of climatology change owing to irrigation are regionally unique. It is possible, too, that sub-regional dependencies exist. For instance, irrigation near topographical features may produce different changes in precipitation than irrigation in a coastal region because of the different drivers of rainfall. If we are to correctly capture anthropogenic influence on climate we must make sure that localized land/atmosphere feedbacks from agriculture are considered. This becomes difficult in GCMs, as different crop specifications must be made over different areas, however it is not outside the realm of possibility that an average crop specification would be usable. Within regional models more rigorous treatment for agriculture should be considered, as temperature or precipitation changes caused by irrigation could mask out or exaggerate broader climate change features.

A noted result of this study was the marked changes in the water budget, which under most conditions would produce additional precipitation (e.g., increases in evaporation, moisture convergence, etc.). However, because of a change to the stability of the profile stemming from cooled surface temperatures, there was a reduction in precipitation. We have found that irrigation in the SEUS serves primarily to reduce precipitation and surface temperatures. The primary mechanism for reducing temperatures is an increase in ground heat flux, which serves to transport heat downward into the moistened soil. As a result of this, the surface cools, which in turn leads to raised stability in the atmospheric column, which stabilizes the atmosphere. The increase in ground heat flux seems to change linearly as irrigation vigor increases, yet the change in precipitation does not follow suit. However, there does seem to be some relationship between irrigation vigor and precipitation event changes; that is, as irrigation vigor increases there is a noticeable increase in 0-1 mm/day rainfall events and decrease in >1 mm/day rainfall events. Irrigation also seems to have an impact on frontal passage in late May and early October. Local changes in atmospheric stability tend to suppress precipitation over the irrigated cells. Instead, fronts travel downwind of irrigated cells before their lifting mechanisms become more efficient. The net result of this change is a reduction in precipitation over irrigated areas during frontal passage. Changes in temperature and precipitation both induced by irrigation are primarily found in the sub-diurnal and diurnal scales equally across all irrigated runs. In addition, increasing irrigation vigor promotes a decrease in number of wet days (days with accumulated rainfall

greater than 1 mm), and a reduction in the threshold (and thus intensity) of heat wave events. Furthermore we found that irrigation mitigates the intensity of heat waves. While few people live in areas where irrigation would occur, this is still significant, as heat waves tend to add to crop stress.

From our results we can conclude that first and foremost irrigation schemes must be assessed for their total water usage. Methods similar to the ones used in this study have been employed in others, yet no such study monitored exactly how much water was used. A more realistic scheme, which only irrigates during the day time, or perhaps keeps track of where the water is withdrawn will further improve upon this study's results. In addition, as computing power grows, additional runs could further enhance our understanding of the climate's sensitivity to irrigation vigor and possibly help in optimal design of irrigation systems. Additional future work in this field could analyze the overall trend of deep-soil temperatures by running a 1-dimensional offline simulation which applied irrigation water to one specific point over a very long period of time (say, 100 years). In addition, further dissection of the land-surface model to understand the consequences of adding water to model computations would be of great benefit to future research. Regardless of model considerations, future work in this field should expand upon the concepts presented here and drive the results of those studies toward applications. Runs such as our irrigation runs can be employed for optimal irrigation planning-- for instance, policymakers and stakeholders alike can determine optimal irrigation schedules for minimizing the impact of irrigation on local rainfall to ensure that the mean state does not experience noticeable change. Likewise, common wisdom currently suggests irrigating at nighttime to avoid loss of water to evapotranspiration. However, results from this study indicate that nighttime ground heat flux will increase, bringing cooler temperatures and ultimately a stabilization of the atmosphere. Furthermore, regional climate model experiments like those presented in this paper can be used by land-use planners to determine the optimal spatial distribution for agruculture. The current areas of agriculture occupy a band-shaped area across the Southeast. Perhaps a different distribution of cultivated areas will produce different spatial results, and have a less dramatic impact on the mean state of the SEUS. Lastly, future experiments must also consider the contribution of urbanized areas to the local climate of the SEUS, as urbanization has been implicated in a number of land-use studies.

APPENDIX A

SUPPLEMENTARY MATERIAL TO 3.1

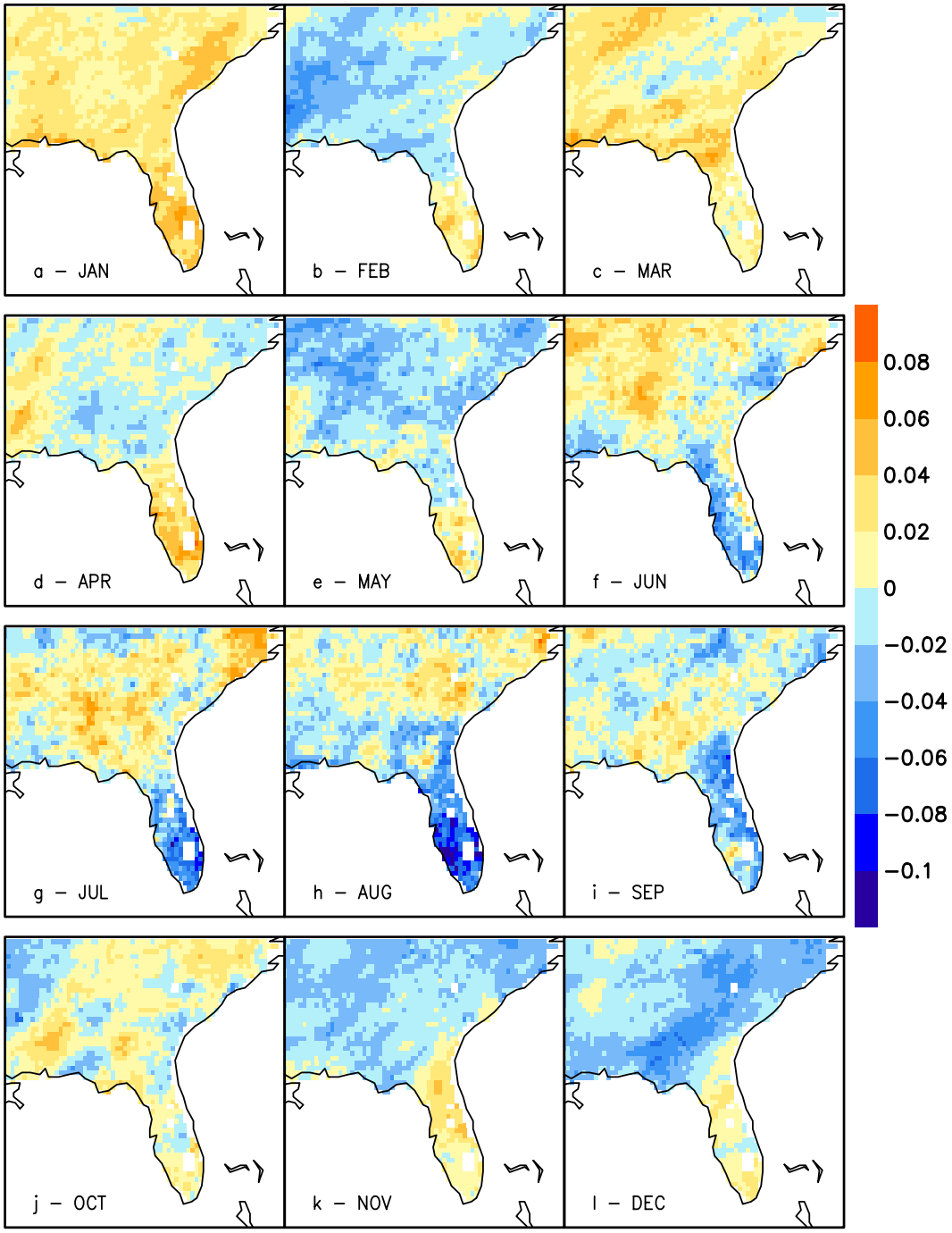

Fig. A1 - Difference plot of (Fig. 5 - Fig. 4) Unitless

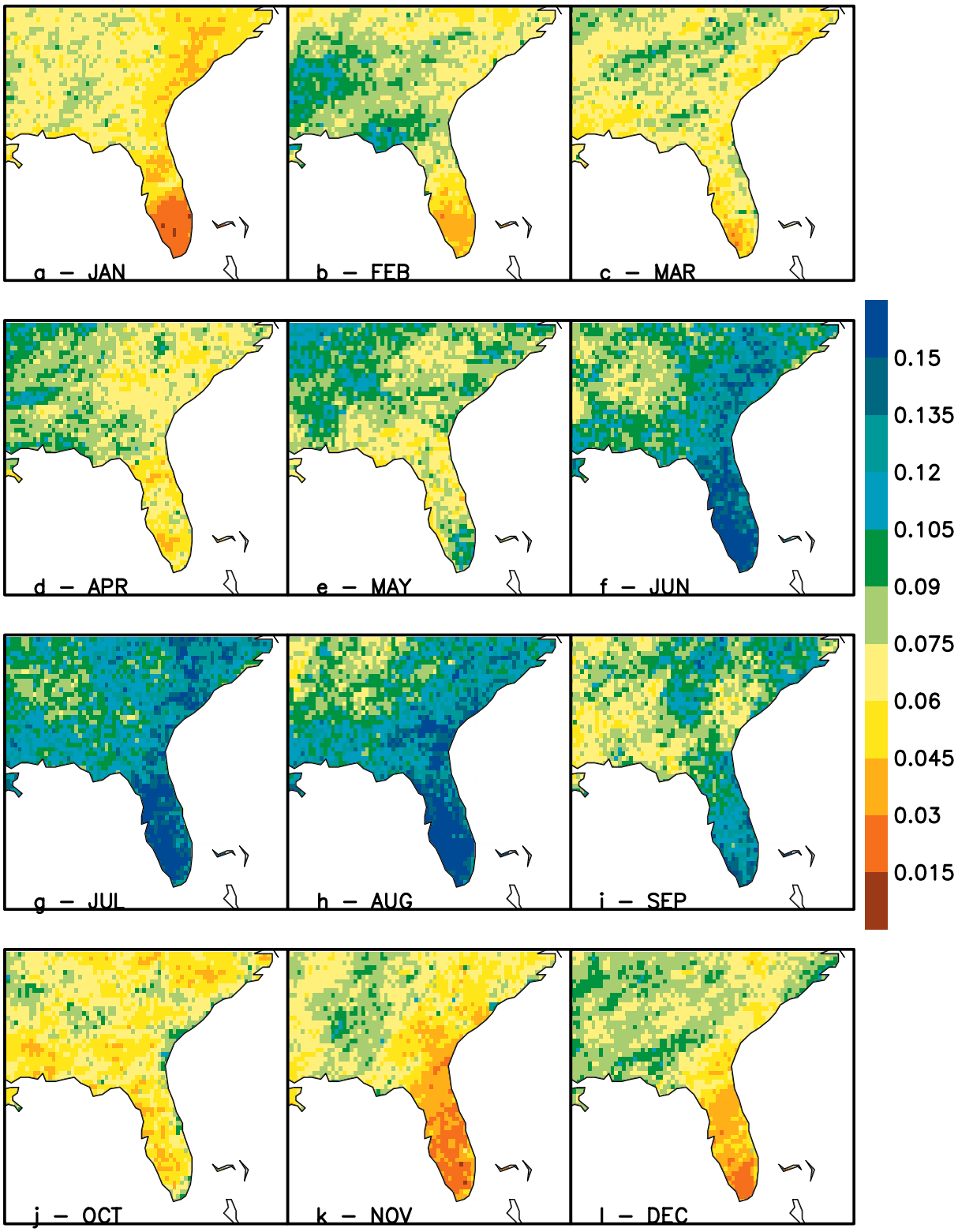

Fig. A2 - The fraction of annual total diurnal precipitation from STAGEIV observations. Unitless.

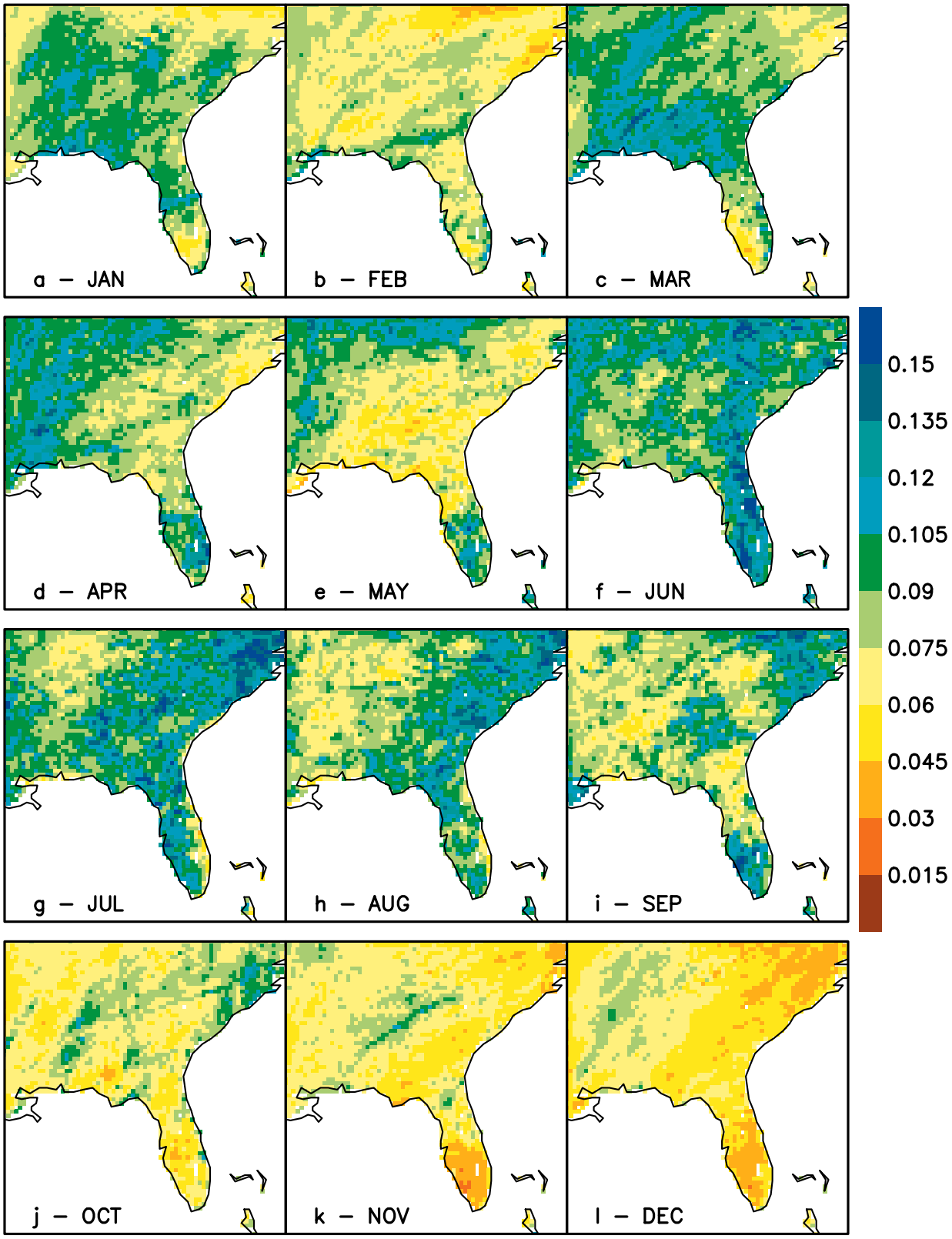

Fig. A3 - As in Fig. A2, but for NCEPR2-KF. Unitless.

REFERENCES

Baldocchi, D., and S. Ma, 2013: How Will Land Use Affect Air Temperature in the Surface Boundary Layer? Lessons Learned from a Comparative Study on the Energy Balance of an Oak Savanna and Annual Grassland in California, USA. Tellus B, 65, doi:10.3402/tellusb.v65i0.19994

Bastola, S. and V. Misra, 2013: Sensitivity of hydrological simulations of southeastern United States watersheds to temporal aggregation of rainfalls. J. Hydrometeor., 14, 1334-1344.

Biggs, W., and M. Graves, 1962: A Lake Breeze Index. J. Appl. Meteor. Climatol., 1, 474-480.

Bornstein R., 1968: Observations of the Urban Heat Island Effect in New York City. J. Appl. Met., 7, 575-582.

Braganza, K., D. Karoly, and J. M. Arblaster, 2004: Diurnal Temperature Range as an Index of Global climate Change During the Twentieth Century. Geophysical Research Letters, 31, doi:10.1029/2004GL019998.

Byers, H., and H. Rodebush, 1948: Causes of Thunderstorms of the Florida Peninsula. J. Meteor., 5, 275-280.

Carbone, R. E., and J. D. Tuttle, 2008: Rainfall Occurrence in the U.S. Warm Season: The Diurnal Cycle. J. Climate, 21, 4132-4146.

Chan, S., and V. Misra, 2010: A Diagnosis of the 1979-2005 Extreme Rainfall Events in the Southeastern United States with Isentropic Moisture Tracing. Mon. Wea. Rev., 138, 1172-1185.

Chow KC, Chan JCL (2009) Diurnal variations of circulation and precipitation in the vicinity of the Tibetan Plateau in early summer. Clim Dyn 32(1):55–73

Compo, G.P., J.S. Whitaker, P.D. Sardeshmukh, N. Matsui, R.J. Allan, X. Yin, B.E. Gleason, R.S. Vose, G. Rutledge, P. Bessemoulin, S. Brönnimann, M. Brunet, R.I. Crouthamel, A.N. Grant, P.Y. Groisman, P.D. Jones, M. Kruk, A.C. Kruger, G.J. Marshall, M. Maugeri, H.Y. Mok, Ø. Nordli, T.F. Ross, R.M. Trigo, X.L. Wang, S.D. Woodruff, and S.J. Worley, 2011: The Twentieth Century Reanalysis Project. Quarterly J. Roy. Meteorol. Soc., 137, 1-28. DOI: 10.1002/qj.776 Free and Open Access.

Cosgrove, B., and coauthors, 2003: Real-Time and Retrospective Forcing in the North American Land Data Assimilation System (NLDAS) Project. J. Geophys. Res., 108, doi:10.1029/2002JD003118.

Dai, A., 1999: Recent Changes in the Diurnal Cycle of Precipitation Over the United States. Geophysical Research Letters, 26, 341-344.

Dai, A., 2006: Precipitation Characteristics in Eighteen Coupled Climate Models. J. Climate, 19, 4605-4630.

Dai, A., and K. E. Trenberth, 2004: The Diurnal Cycle and its Depiction in the Community Climate System Model. J. Climate, 17, 931-951.

Dai, A., F. Girgi, and K. E. Trenberth, 1999: Observed and Model-Simulated diurnal cycles of Precipitation Over the Contiguous United States. J. Geophys. Res., 104, 6377-6402.

Das, S., A. K. Mitra, G. R. Iyengar, and J. Singh, 2002: Skill of Medium-Range Forecasts over the Indian Monsoon Region Using Different Parameterizations of Deep Convection. Weather and Forecasting, 17, 1194-1210.

Davis, C. A., K. W. Manning, R. E. Carbone, S. B. Trier, and J. D. Tuttle, 2003: Coherence of Warm-Season Continental Rainfall in Numerical Weather Prediction Models. Mon. Wea. Rev., 131, 2667-2679.

Defries, R., L. Bounoua, and G. Collatz, 2002: Human modification of the landscape and surface in the next fifty years. Global Change Biology, 8, 438-458.

Dinapoli, S., and V. Misra, 2012: Reconstructing the 20th century high-resolution climate of the southeastern United States, J. Geophys. Res., 117, doi:10.1029/2012JD018303

Dirmeyer, P.A., and coauthors, 2012: Simulating the diurnal cycle of rainfall in global climate models: resolution versus parameterization. Clim. Dyn, 39, 399-418.

Ek, M. B., K. E. Mitchell, Y. Lin, E. Rogers, P. Grunmann, V. Koren, G. Gayno, and J. D. Tarpley 2003: Implementation of Noah land surface model advances in the National Centers for Environmental Prediction operational mesoscale Eta model, J. Geophys. Res., 108, 8851.

Evans, J. P., and S. Westra, 2012: Investigating the Mechanisms of Diurnal Rainfall Variability Using a Regional Climate Model, J. Clim., 25, 7232-7247.

Gentry, R., and P. Moore, 1954: Relation of Local and General Wind Interaction Near the Seas Coast to Time and Location of Air-Mass Showers. Journal of Atmospheric Sciences, 11, 507-511.

Gibson, H., and T. Vonder Haar, 1990: Cloud and Convection Frequencies over the Southeast United States as Related to Small-Scale Geographic Features. Mon. Wea. Rev., 118, 2215-2227.

Harding, K., P. K. Snyder, and S. Liess, 2013: Use of Dynamical Downscaling to Improve the Simulation of Central U.S. Warm Season Precipitation in CMIP5 Models, J. Geophys. Res., 118, 12,522-12,536.

Huang, N., and Z. Wu, 2008: A Review on Hilbert-Huang Transform: Method and its Applications to Geophysical Studies. Rev. Geophys., 46, doi:10.1029/2007RG000228.

Hurrell, J. W., J. J. Hack, D. Shea, J. M. Caron, J. Rosinski, 2008: A New Sea Surface Temperature and Sea Ice Boundary Dataset for the Community Atmosphere Model. J. Climate, 21, 5145-5153.

Hutson, S., N. Barber, J. Kenny, K. Linsey, D. Lumia, and M. Maupin, 2000: Estimated use of water in the united states in 2000. USGS Circular 1268, revised February 2005.

Kain, J., and M. Fritsch, 1993: Convective Parameterization for Mesoscale Models: The Kain-Fritsch Scheme. Meteorological Monographs, 24, 165-170.

Kain, L., 2004: The Kain-Fritsch Convective Parameterization: An Update. Journal of Applied Meteorology,, 43, 170-181.

Kanamaru, H., and M. Kanamitsu, 2007: Scale selective bias correction in a downscaling of global analysis using a regional model, Mon. Weather Rev., 135, 334–350.

Kanamaru, H., and M. Kanamitsu, 2008: Model diagnosis of nighttime minimum temperature warming during summer due to irrigation in the California Central Valley. J. Hydromet., doi:10.1175/2008JHM967.1.

Kanamitsu, M., K. Yoshimura, Y. Yhang, and S. Hong, 2010: Errors of interannual variability and multi-decadal trend in dynamical regional climate downscaling and its corrections. J. Geophys. Res., 115, D17115.

Kanamitsu, M., W. Ebisuzaki, J. Woollen, S. K. Yang, J. J. Hnilo, M. Fiorino, and G. L. Potter, 2002: NCEP DOE AMIP II reanalysis (R2), Bull. Am. Meteorol. Soc., 83, 1631–1643.

Kang, H.-S., S.-Y. Hong, 2008: Sensitivity of the Simulated East Asian Summer Monsoon Climatology to Four Convection Parameterization Schemes. Journal of Geophysical Research, 113, doi:10.1029/2007JD00969

Kueppers, L., and M. Snyder, 2012: Influence of irrigated agriculture on diurnal surface energy and water fluxes, surface climate and atmospheric circulation in California. Clim. Dyn., 38, 1017-1029.

Lauritsen, R. G. and Jeffrey C. Rogers, 2012: U.S. Diurnal Temperature Range Variability and Regional Causal Mechanisms, 1901–2002. J. Climate, 25, 7216–7231.

Lee, M. I., et al, 2007: Sensitivity to Horizontal Resolution in the AGCM Simulations of Warm Season Diurnal Cycle of Precipitation Over the United States and Northern Mexico. J. Clim., 20, 1862-1881.

Lehmann, R., 1993: On the Choice of Relaxation Coefficients for Davies Lateral Boundary Scheme for Regional Weather Prediction Models. Meteor. Atmos. Phys., 52, 1-14.

LeMone, M. A, 1973: The Structure and Dynamics of Horizontal Roll Vortices in the Planetary Boundary Layer. J. Atmos. Sci., 30, 1077–1091.

Lewis, S., and D. J. Karoly, 2013: Evaluation of Historical Diurnal Temperature Range Trends in CMIP5 Models. J. Clim. 26, doi:10.1175/JCLI-D-13-00032.1

Li, L., W. Li, A. P. Barros, 2013: Atmospheric Moisture Budget and its Regulation of the Summer Precipitation Variability Over the Southeastern United States. Clim. Dyn., 41, 613-631.

Li, W., L. Li, R. Fu, L. Deng, and H. Wang, 2011: Changes to the North Atlantic Subtropical High and its Role in the Intensification of Summer Rainfall Variability in the Southeastern United States. J. Climate, 24, 1499-1506.

Li,, H. and V. Misra, 2014: Thirty two year ocean-atmosphere coupled downscaling of global reanalysis over the Intra-American Seas. Clim. Dyn., doi:1.007/s00382-014-2069-9.

Liang X.-Z., L. Li, A. Dai, and K. Kunkel, 2004: Regional Climate Model Simulation of Summer Precipitation Diurnal Cycle Over the United States. Geophys Res Lett, 31, doi:10.1029/2004GL021054.

Lin, Y. and K. E. Mitchell, 2005: The NCEP Stage II/IV hourly precipitation analyses: development and applications. Preprints, 19th Conf. on Hydrology, American Meteorological Society, San Diego, CA, 9-13 January 2005, Paper 1.2.

Liu, S., W. Graham, and J. Jacobs, 2005: Daily Potential Evapotranspiration and Diurnal Climate Forcings: Influence on the Numerical Modeling of Soil Water Dynamics and Evapotranspiration. Journal of Hydrology, 309, 39-52.

Lobell, D., C. Bonfils, and J.-M. Faurès, 2008: The Role of Irrigation Expansion in Past and Future Temperature Trends. Earth Interactions, 12, doi:10.1175/2007EI1241.1

Lobell, D., G. Bala, A. Mirin, T. Phillips, R. Maxwell, D. Rotman, 2009: Regional differences in the influence of irrigation on climate. J Climate, 22, 2248-2255.

Loveland, T. R., J. W. Merchant, B. C. Reed, J. F. Brown, D. O. Ohlen, P. Olson, and J. Hutchinson, 1995: Seasonal land cover regions of the United States, Ann. Assoc. Am. Geogr., 85, 339–355.

McNally, A., and coauthors, 2004: Assessing the Region Via Indicators: The Economy. Great Valley Center special report.

Meinke, I., J. Roads, and M. Kanamitsu, 2007: Evaluation of RSM-Simulated Precipitation during CEOP. Journal of the Meteorological Society of Japan, 85A, 145-166.

Misra, V., 2007: Addressing the issue of systematic errors in a regional climate model. J. Climate, 20, 801-818.

Misra, V., and P. A. Dirmeyer, 2009: Air, Sea, and Land Interactions of the Continental US Hydroclimate. J. Hydromet., 10, 353-373

Misra, V., L. Moeller, L. Stefanova, S. Chan, J. J. O'Brien, T. J. Smith III, and N. Plant, 2011: The Influence of Atlantic Warm Pool on Panhandle Florida Sea Breeze, J. Geophys. Res., 116, doi:10.1029/2010JD015367

Misra, V., P. Dirmeyer, B. Kirtman, 2003: Dynamical downscaling of seasonal simulations over South America. Journal of Climate, 16, 103-117.

Misra, V., S. DiNapoli, and S. Bastola, 2012: Dynamic downscaling of the twentieth-century reanalysis over the southeastern United States. Reg. Envrion. Change, 13, S15-23.

Mitchell, K., and coauthors, 2005: User's Guide -- Noah version 2.71. Available at http://www.ral.ucar.edu/research/land/technology/lsm/noah/Noah_LSM_USERGUIDE_2.7.1.pdf

Moorthi, S., and M. Suarez, 1992: Relaxed Arakawa-Schubert: A Parameterization of Moist Convection for General Circulation Models. Mon Wea Rev, 120, 978-1002.

MyMeteo, cited 2015: WRF Miscellanea. [Available online at http://mymeteo-notes.wikispaces.com/WRF+Miscellanea]

Oke, T., 1982: The energetic basis of the urban heat island. Quarterly Journal of the Royal Meteorological Society, 108, 1-24.

Ookouchi, Y., M. Segal, R. C. Kessler, and R. Pielke, 1984: Evaluation of soil moisture effects on the generation and modification of mesoscale circulations. Mon. Wea. Rev., 112, 2281-2292.

Parker, M.D. and D.A. Ahijevych, 2007: Convective episodes in the east-central United States. Mon. Wea. Rev., 135, 3707-3727.

Pielke, R. A., 1974: A Three-Dimensional Numerical Model of the Sea Breezes Over South Florida. Mon. Wea. Rev.,102,115–139.

Pielke, R.A., and coauthors, 2007: An overview of regional land-use and land-cover impacts on rainfall. Tellus, doi:10.1111/j.1600-0889.2007.00251.x.

Portmann, R. W., S. Solomon and G. C. Hegeri, 2008: Spatial and seasonal patterns in climate change, temperatures, and precipitation across the United States. Proc. Nat. Acad. Sci., 106, 7324-7329, doi:10.1073/pnas0808533106.

Puma, M., and B. Cook, 2012: Effects of irrigation on global climate during the 20th century. J Geophys Res, 115, D16120.

Qian, Y., M. Huang, B. Yang, and L. Berg, 2013: A modeling study of irrigation effects on surface fluxes and land-air-cloud interactions in the Southern Great Plains. J. Hydromet., 14, 700-721.

Rayner, N.A., D. E. Parker, E. B. Horton, C. K. Folland, L. V. Alexander, D. P. Rowell, E. C. Kent, and A. Kaplan, 2003: Global Analyses of Sea Surface Temperature, Sea Ice, and Night Marine Air Temperature Since the Late Nineteenth Century. J. Grophys. Res., 108, doi:10.1029/2002JD002670.

Reynolds, R. W., N. A. Rayner, T. M. Smith, D. C. Stokes, and W. Wang, 2002: An Improved In Situ and Satellite SST Analysis for Climate. J. Climate, 15, 1609-1625.

Risbey, J. S., and P. H. Stone, 1996: A case study of the adequacy of GCM simulations for input to regional climate change assessments. J. Climate, 9, 1441–1467.

Rogers E., D. Deaven, and G. DiMego, 1995: The Regional Analysis System for the Operational "Early" Eta Model: Original 80-km Configuration and Recent Changes. Wea. Forecasting, 10, 810-825.

Sacks, W., B. Cook, N. Buenning, S. Levis, J. Helkowski, 2009: Effects of global irrigation on the near-surface climate. Clim dyn, 33, 159-175.

Saeed, F., S. Hagemann, and D. Jacob, 2009: Impact of irrigation on the South Asian summer monsoon. Geophys. Res. Lett., 36, L20711.

Sapiano, M. R. P., and P. A. Arkin, 2009: An Intercomparison and Validation of High-Resolution Satellite Precipitation Estimates with 3-Hourly Gauge Data. J. Hydrometeor., 10, 149-166.

Schneider, A., M. Friedl, and D. Potere, 2009: A new map of global urban extent from MODIS satellite data. Env. Res. Lett., 4, 044003.

Schwartz, B. E., and L. F. Bosart, 1979: The Diurnal Variability of Florida Rainfall. Mon. Wea. Rev., 107, 1535-1545.

Selman, C., V. Misra, 2015a: Simulating diurnal variations over the Southeastern United States. J. Geophys. Res.: Atmos, 120, 180-198.

Selman, C., V. Misra 2015b: The impact of an extreme case of irrigation on the Southeastern United States Climate, in preparation.

Selman, C., V. Misra, 2015c: The sensitivity of Southeastern United States climate to varying irrigation vigor, in preparation.

Selman, C., V. Misra, L. Stefanova, S. DiNapoli, and T. J. Smith III, 2013: Twenty-first-century wet season projections over the Southeastern United States. Reg. Env. Change., S153-164. doi:10.1007/s10113-013-0477-8.

Siebert, S., P. Döll, J. Hoogeveen, J.-M. Faures, K. Frenken, and S. Feick, 2005: Development and validation of the global map of irrigation areas. Hydrology and Earth System Sciences, 9, 535-547.

Slingo, A., K. Hodges, G. Robinson, 2004: Simulation of the diurnal cycle in a climate model and its evaluation using data from Meteosat 7. Q J R Meteorol Soc 130(599):1449–1467

Sorooshian, S., J. Li, K.-L. Hsu and X. Gao, 2011: How significant is the impact of irrigation on the local hydroclimate in California's Central Valley? Comparison of model results with ground and remote-sensing data. J. Geophys. Res., 116, D06102.

Stefanova, L., V. Misra, S. Chan, J. J. O'Brien and T. J. Smith III, 2012: A proxy for high resolution regional reanalysis for the Southeast United States: Assessment of precipitation variability. Clim. Dyn., 38, doi:10.1007/s00382-011-1230-y

Sun, G., H. Riekerk, and L. Kornhak, 2000: Ground-water table rise after forest harvesting on cypress-pine flatwoods in Florida. WETLANDS, 20, 101-112.

Sun, G., S. G. McNulty, D. M. Amatya, R. W. Skaggs, L. W. Swift, J. P. Shepard, and H. Riekerk, 2002. A Comparison of the Hydrology of the Coastal Forested Wetlands/Pine Flatwoods and the Mountainous Uplands in the Southern US. J. Hydrology, 263, 92-104.

Tian, Y., C. D. Peters-Lidard, B. J. Choudhury, and M. Garcia, 2007: Multitemporal Analysis of TRMM-Based Satellite Precipitation Products for Land Data Assimilation Applications. J. Hydrometeor., 8, 1165-1183.

Uppala, S. M., KÅllberg, P. W., Simmons, A. J., Andrae, U., Bechtold, V. D. C., Fiorino, M., Gibson, J. K., Haseler, J., Hernandez, A., Kelly, G. A., Li, X., Onogi, K., Saarinen, S., Sokka, N., Allan, R. P., Andersson, E., Arpe, K., Balmaseda, M. A., Beljaars, A. C. M., Berg, L. V. D., Bidlot, J., Bormann, N., Caires, S., Chevallier, F., Dethof, A., Dragosavac, M., Fisher, M., Fuentes, M., Hagemann, S., Hólm, E., Hoskins, B. J., Isaksen, L., Janssen, P. A. E. M., Jenne, R., Mcnally, A. P., Mahfouf, J.-F., Morcrette, J.-J., Rayner, N. A., Saunders, R. W., Simon, P., Sterl, A., Trenberth, K. E., Untch, A., Vasiljevic, D., Viterbo, P. and Woollen, J. (2005), The ERA-40 re-analysis. Q.J.R. Meteorol. Soc., 131, 2961–3012. doi: 10.1256/qj.04.176

Wallace, J. M., 1975: Diurnal Variations in Precipitation and Thunderstorm Frequency over the Conterminous United States. Mon. Wea. Rev., 103, 406-419.

Wang Y., L. Zhou, and K. Hamilton, 2007: Effect of convective entrainment/detrainment on simulation of tropical precipitation diurnal cycle. Mon. Wea. Rev., 135, 567-585.

Wei, J., and P. Dirmeyer, 2012: Dissecting Soil Moisture-Precipitation Coupling. Geophys Res Lett, 39, doi:10.1029/2012GL053038.

Wei, J., P. Dirmeyer, D. Wisser, M. Bosilovich, and D. Mocko, 2013: Where does the irrigation water go? An estimate of the contribution of irrigation to precipitation using MERRA. J. Hydromet, doi:10.1175/JHM-D-12-079.1

Wootten, A., S. Raman, and A. Sims, 2010: Diurnal Variations of Precipitation Over the Carolina Sandhills Region. J. Earth Syst. Sci., 119, 579-596.

Wu Z., N. Huang, J. Wallace, B. Smoliak, and X. Chen, 2011: On the time-varying trend in global-mean surface temperature. Clim. Dyn., 37, 759-773.

Zhou, L., A. Dai, Y. Dai, R. S., C.-Z. Zou, Y. Tian, and H. Chen, 2008: Spatial Dependence of Diurnal Temperature Range Trends on Precipitation from 1950 to 2004. Clim. Dyn., 32, 429-440.

Zobler, L. 1986: A world soil file for global climate modeling. NASA Technical Memorandum 87802.

BIOGRAPHICAL SKETCH

Christopher Manuel Selman is the son of E. Bruce Selman III and Lourdes Delatorre Selman, and was born in Bradenton, FL. From a young age, he knew that he wanted to be a meteorologist and has followed that dream since. He completed his undergraduate and graduate degrees at Florida State University, majoring in the field of meteorology. He hopes to continue his pursuit of research by entering a postdoctoral research position, followed by entrance into either a teaching or research-oriented university.